공학박사학위논문

Synthesis of Pd-Cu catalyst with modified composition and structure via galvanic displacement and its electrochemical applications

갈바닉 치환 반응을 이용한 조성 및 구조가 개질된 팔라듐-구리 촉매의 합성 및 전기화학적 응용

2019년 8월

서울대학교 대학원
화학생물공학부
백 승 연

Abstract

Electronic structure and electrochemically active surface area of catalysts are the important factors to determine the catalytic activity of electrochemical reactions. The catalyst synthetic method using galvanic displacement reaction can provide highly active electro-catalysts by alloying and changing their geometric structure. For example, when immersing Cu substrate in a solution containing Pd^{2+} ions, Pd deposition occurs spontaneously by galvanic displacement reaction originated from the difference of standard reduction potentials between Pd and Cu. During Pd-Cu galvanic displacement reaction, Cu atoms in the substrate diffuse into Pd deposit forming Pd-Cu alloy by Kirkendall effect. The catalytic activity of Pd can be enhanced by alloying with Cu which can change the electronic structure of Pd by ligand effect. The structure of Pd-Cu catalyst can be controlled from planar to whisker shapes by manipulating the reaction kinetics of galvanic displacement. The addition of Cl^- ions in the reaction bath accelerates the galvanic displacement reaction and develops a steep concentration gradient of Pd^{2+} ions near the surface of Cu substrate. This induced the deposition of Pd-Cu in the vertical direction to form a whisker instead of horizontal extension. To verify the advantage of whisker-structured catalyst, the catalytic activity of Pd-Cu whisker toward electrochemical ethanol oxidation reaction was investigated**.** Pd-Cu whisker showed 21 times higher electrocatalytic performance than planar Pd due to the large surface area of whisker structure which could provide more reactive sites and the modified electronic structure of catalyst by alloying Pd with Cu**.**

The prepared Pd-Cu whisker catalyst was also applied for N_2O reduction. To enhance the N_2O approach to rough-surfaced catalyst and N_2O dissolution, electrochemical system combined with Couette-Taylor flow (CTF) mixer was adopted. When Ta number exceeds the critical Ta number by increasing rotating speed of inner cylinder of CTF mixer, Taylor vortices evolve in the solution, resulting in the rapid N_2O dissolution and enhancing N_2O solubility. The effectiveness of enhanced N_2O dissolution on the N_2O reduction was investigated by applying electrical potential on the CTF mixer. Pd-Cu whisker catalyst was loaded on outer cylinder of CTF mixer which played a role of cathode for N_2O reduction. N_2O conversion of 99.99% was obtained with introduction of Taylor vortices in the solution using a CTF mixer. Therefore, it can be suggested that the synthetic method to control geometric and electronic structure of catalysts using galvanic displacement reaction and the CTF mixer/electrolysis reactor hybrid system for efficient reactant dissolution can significantly enhance the electrochemical performance.

The electronic structure of Pd-Cu catalysts can be modulated by the addition of citric acid in the galvanic displacement bath. The atomic ratio of Pd to Cu in Pd-Cu catalysts, which determines the electronic structure, was controlled by varying citric acid concentration during the displacement. Citric acid was incorporated into the Pd-Cu deposit during galvanic displacement and restrained the diffusion of Cu from Cu substrate to deposit leading to decrease in Cu content in the Pd-Cu catalysts. The electrocatalytic activity for N_2O reduction was strongly dependent on Pd/Cu composition in Pd-Cu catalysts. The optimum composition of Pd-Cu catalysts with the highest N_2O reduction activity was $Pd_{66}Cu_{34}$. Moreover, the $Pd_{66}Cu_{34}$ catalyst showed remarkably enhanced mass activity for N_2O reduction compared with a commercial Pd/C. The density functional theory (DFT) calculations revealed that the highest N_2O reduction activity of $Pd_{66}Cu_{34}$ was attributed to the moderate bonding energy to reaction intermediates which resulted from interatomic charge transfer between Pd and Cu.

Keywords: Pd-Cu catalyst, galvanic displacement reaction, whisker catalyst, electrochemical ethanol oxidation, electrochemical N_2O reduction, Couette-Taylor flow mixer

Student number: 2014-21528

Content

List of Tables

List of Figures

CHAPTER I

Introduction

1.1. Bimetallic catalyst for electrochemical reaction

Pd or Pd-based metal, with high catalytic activity and low price, is one of the most important and widely used catalysts. In particular, Pd has been considered as a promising material for electrochemical reduction of N_2O. N_2O, which is one of the main components of the greenhouse gases, has 268 times higher global warming potential (GWP) than CO_2 [1-6], and it plays a significant role as an ozone depleting gas [7]. N_2O is produced in relatively small quantity compared with other greenhouse gases through microbial action, fossil combustion, and industrial process, however, the amount of N_2O in the atmosphere has been continuously increasing at a rate of about 0.2% per year in recent decades [8]. Moreover, the life time of N_2O in atmosphere is estimated to be 150 years [9]. Thus, the reduction of N_2O generation or the removal of N_2O is as important as the diminution in CO_2 generation. Various decomposition methods such as a thermal decomposition, a selective catalytic decomposition, and an electrochemical decomposition have been used for the N_2O removal as summarized on Table 1.1 [10-15]. The thermal decomposition is a method of decomposing N_2O by elevating temperature in the combustion zone above 800^oC [10]. The selective catalytic decomposition process is also carried out at high temperature above 250°C and decomposes N_2O by using metal oxide, zeolites or carbon-supported copper catalyst [11, 12]. However, these high temperature processes have many problems to be solved. It is difficult to maintain the activity of the catalytic reaction for a long time due to deteriorated catalysts by N_2O, which is a very powerful oxidant at an elevated temperature [13, 14]. In addition, some toxic pollutants such as NO and NO_2 are formed as by-products of N_2O decomposition at high temperature [7, 9]. Therefore, it is necessary to develop a N_2O decomposition process possible at mild temperature thus not deteriorating catalysts and not producing harmful by-products. It is not easy to decompose N_2O to N_2 and O with a conventional process at low temperatures even in the presence of catalysts. On the other hand, electrochemical reduction of N_2O to N_2, which is performed by applying electrical energy on the electrode, is thermodynamically feasible even at room temperature and does not produce environmentally toxic by-products as depicted below [15],

$$\text{Acidic condition: } N_2O + 2H^+ + 2e^- \rightarrow N_2 + H_2O,\ E^0_{298K} = 1.76\ V_{SHE} \qquad (1)$$

$$\text{Basic condition: } N_2O + H_2O + 2e^- \rightarrow N_2 + 2OH^-,\ E^0_{298K} = 0.94\ V_{SHE} \qquad (2)$$

In 1997, Kudo and Mine investigated catalytic activity of various metals toward electrochemical N_2O reduction as represented on Figure 1.1 [2, 4, 16]. Faradaic efficiencies largely beyond 100% were probably due to the corrosion of these metals by the reduction of N_2O [17]. They found that Pd is the most effective material for converting N_2O to N_2 with nearly 100% of Faradaic efficiency at the smallest overpotential among metals they investigated. The mechanism of N_2O reduction on Pd surface was proposed as described in Equation (3) and (4) [15].

$$N_2O \leftrightarrow N_2O_{ads} \tag{3}$$

$$N_2O_{ads} + H_2O + 2e^- \rightarrow N_2(g) + 2OH^- \tag{4}$$

It suggests that the adsorption and dissociation energies of N_2O play a key role for N_2O reduction. The simplest way to modify the adsorption and dissociation energies of reactant on Pd is alloying Pd with other metals which can change electronic structure of Pd by ligand effect as demonstrated in Figure 1.2 [18]. Ligand effect can be induced on Pd by adding hetero-metals with different work function which determines the degree of electron filling of the *d*-band of Pd. In the case of adding Cu on Pd, the partial electron transfer from Cu to Pd can take place due to the larger work function of Pd than Cu [19]. The electron transfer between Cu and Pd leads to broadening of the *d*-band of Pd and lowering the *d*-band center position. As the *d*-band of Pd is broaden, the filling of antibonding state, which is formed by interaction between Pd and reactants, increases. In the context of chemisorption of reactants to Pd surface, a higher *d*-band center of Pd results in stronger bonding. Density functional theory (DFT) studies suggested that several first-row transition metals such as Cu could induce significant charge transfer on neighboring Pd which could change adsorption energy of N_2O on Pd-Cu catalyst [20-

24]. Therefore, the catalytic activity of Pd toward electrochemical N_2O reduction can be enhanced by alloy formation with Cu. DFT calculation performed by W. Wei et al. showed that catalytic activity of Pd toward thermal N_2O decomposition could be enhanced by adding Au on Pd to lower chemisorption energy as compared to pure Pd [25]. In this way, lowering chemisorption energy of Pd by addition of appropriate amount of Cu can improve the electrochemical N_2O reduction activity.

Together with N_2O reduction, Pd catalyst is well known to exhibit high activity for the electrochemical oxidation of ethanol, which is a fuel in direct ethanol fuel cells (DEFCs), in alkaline media [26-28]. A mechanism for ethanol oxidation over Pd in alkaline media suggested by Z.X. Liang et al. is [29]:

$$OH^- \rightarrow OH_{ad} + e^- \tag{5}$$

$$(CH_3CH_2OH)_{ad} + 3OH^- \rightarrow (COCH_3)_{ad} + 3H_2O + 3e^- \tag{6}$$

$$(COCH_3)_{ad} + OH_{ad} \rightarrow CH_3CO_2H \tag{7}$$

The XPS results as shown in Figure 1.3 represent that Cu 2p data for Pd-Cu catalyst shifts negatively when compared to pure Cu while Pd 3d binding energy is upshifted when Cu is added to the Pd, which confirms charge transfer between Pd and Cu. The charge transfer induces an electronic effect on Pd surface and it affects the bonding energy of intermediate species. The addition of Cu to the Pd increases the rate of hydroxyl adsorption by electronic perturbation which plays an important role in enhancing the ethanol oxidation reaction. Therefore, Pd-Cu bimetallic catalyst can exhibit superior electrocatalytic activity and durability for ethanol oxidation in alkaline media due to the accelerated reaction by strongly adsorbed hydroxyl ions and the suppressed CO poisoning (Figure 1.4) [30, 31].

In addition to the control of electronic structure of catalyst by alloying, the increase in the geometrical surface area of catalysts can improve their electrochemical properties. The high surface area leads to an improvement in the apparent reaction rate due to the increased number of active sites for electrochemical reactions. Recently, number of attempts have been made to prepared Pd-Cu bimetallic catalysts with extended surface area for further enhanced electrocatalytic activities. It has been reported that small-sized PdCu alloy nanocapsules on 3D-graphene sheets (PdCu/3DGS) and a 3D-nanochain network of PdCu alloy (PdCu NNC) present the much enhanced electrocatalytic performance towards ethanol oxidation due to its hollow structure with high surface area and electronic interactions between Pd and Cu [32, 33].

Table 1.1. Various methods for N_2O decomposition [10-15]

Thermal decomposition	Selective catalytic decomposition	Electrochemical decomposition
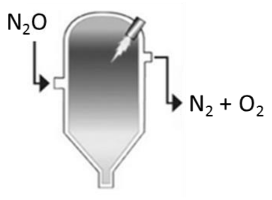	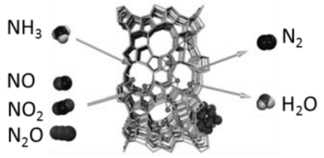	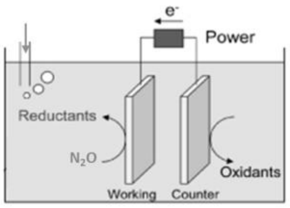
(decomposition temperature >800°C)	(>250°C)	(~25°C)

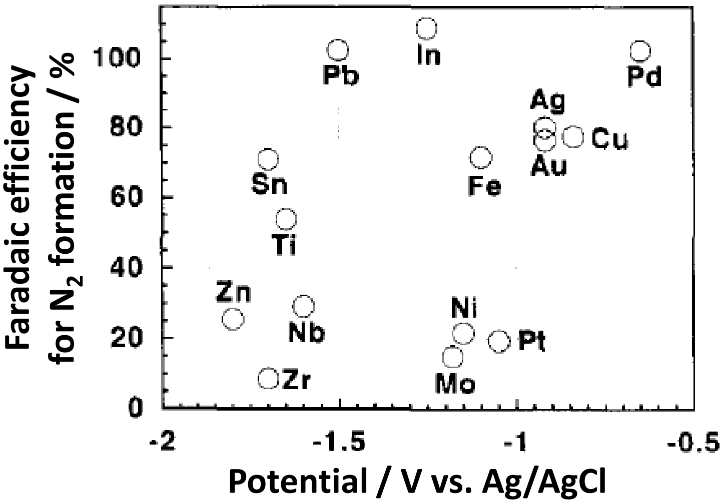

Figure 1.1. Electrochemical reduction of N_2O on various metal electrodes at 8 mA cm^{-2} [16].

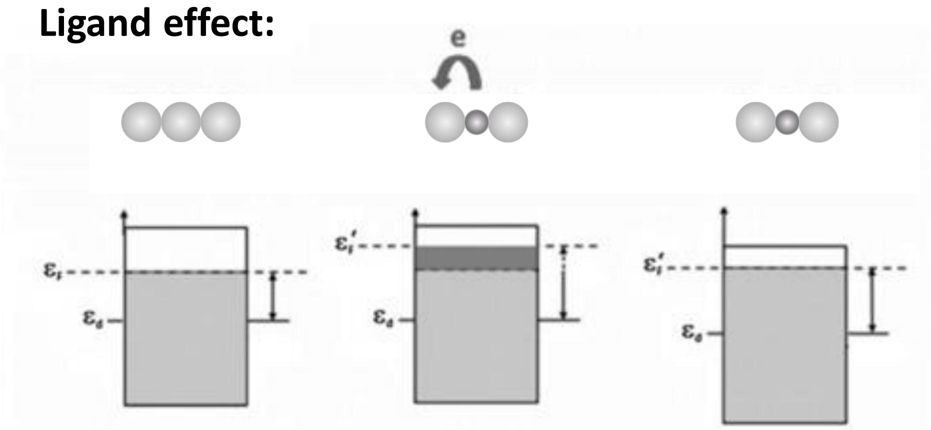

Figure 1.2. Schematic description of the ligand effect in bimetallic catalyst when an alloyed structure is formed [18].

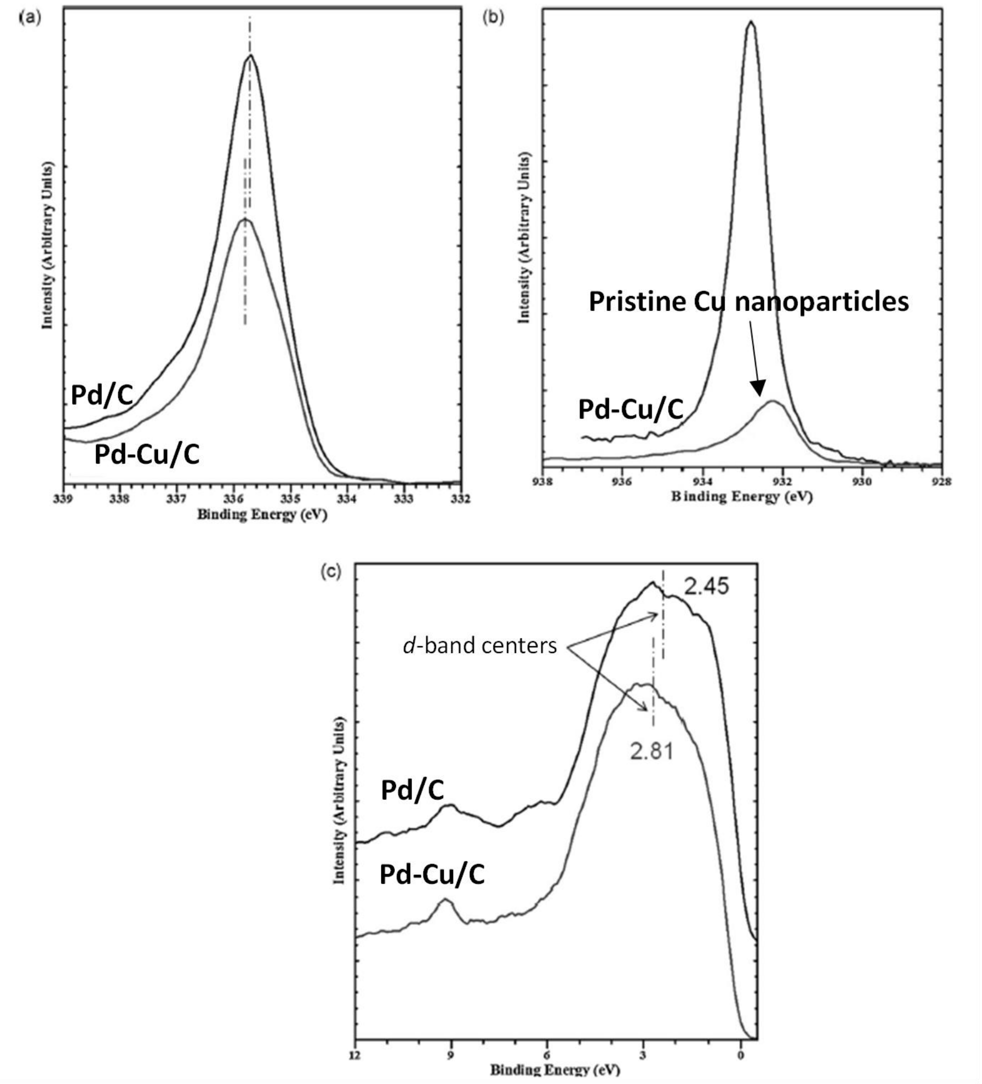

Figure 1.3. XPS results indicating a binding energy (a) upshift of 0.2 eV for Pd $3d_{5/2}$, (b) downshift of 0.5 eV for Cu $2p_{3/2}$ and (c) valence band spectra and calculated *d*-band center for Pd/C and Pd-Cu/C [31].

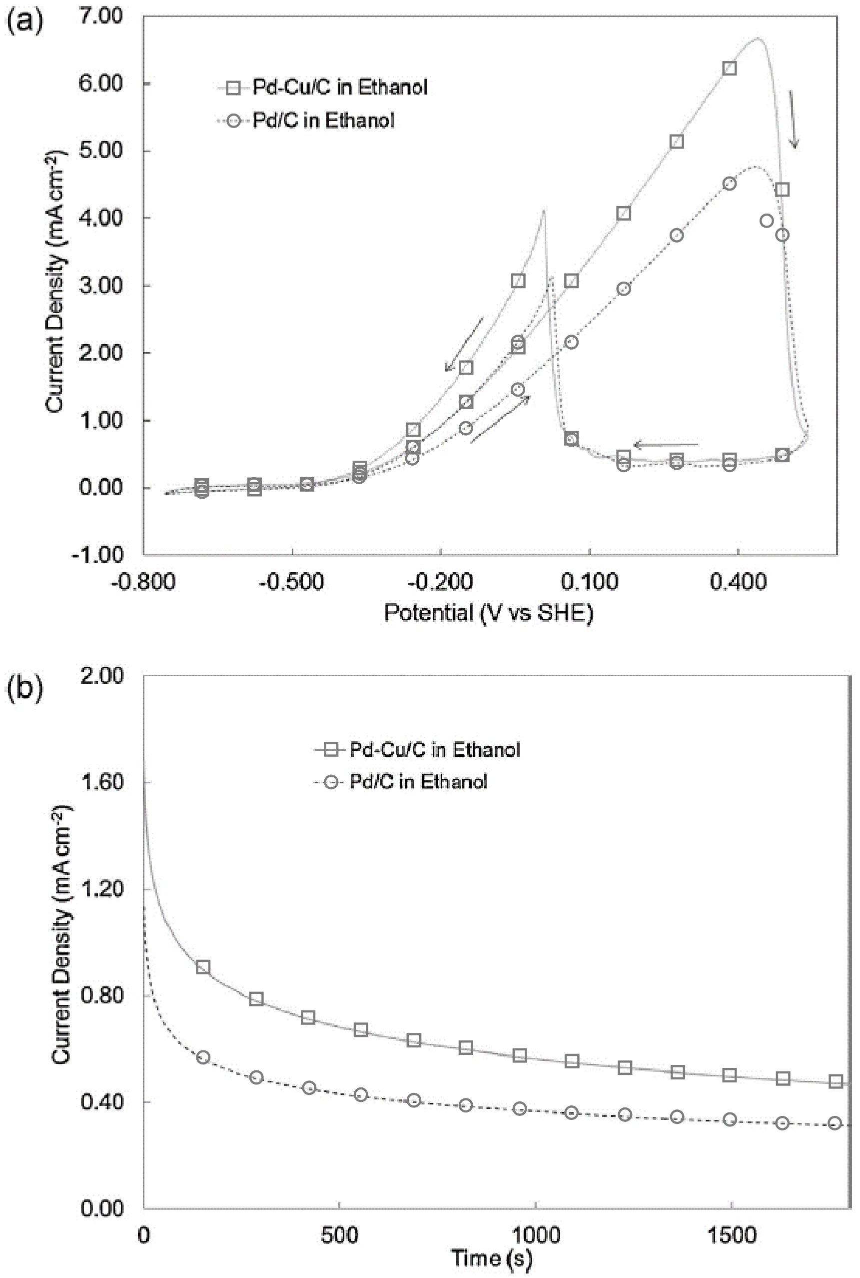

Figure 1.4. (a) Cyclic voltammogram of ethanol oxidation on Pd-Cu/C and Pd/C at 30 mV s^{-1} and (b) chronoamperometry for 30 minutes at -0.156 V vs SHE in 1 M ethanol + 1 M KOH [31].

1.2. Fabrication of bimetallic catalyst by galvanic displacement reaction

Catalyst preparation using galvanic displacement is a facile and economically sustainable method of spontaneous deposition that requires no additional energy supply; catalyst deposition occurs simply by immersing a substrate in the solution containing the ionic precursors of metal to be deposited [34, 35]. Galvanic displacement is mediated by the difference in standard reduction potentials; the metal substrate is spontaneously oxidized upon coming into contact with an ionized metal source with a more positive reduction potential. The electrons generated from the oxidation reaction, i.e. dissolution of the substrate, go towards the reduction reaction, i.e. metal deposition on the substrate. Through the galvanic displacement, bimetallic catalysts are formed via intermetallic diffusion between a substrate and a deposit, which is known as Kirkendall effect [36, 37]. Figure 1.5 shows the schematic illustration of Kirkendall effect in a diffusion couple A-B. During galvanic displacement reaction, atomic migration can occur at the interface where atoms diffuse from metal A to metal B and vice versa, leading to the formation of A-B alloy. As a consequence of the different diffusion rates of metal A and B, vacancies are injected in the zone of the faster diffusing metal. For example, the Pd^{2+} ions are reduced and Pd is deposited by immersing a sacrificial Cu substrate in Pd^{2+} solution due to the difference of the standard reduction potential between Pd and Cu. The half-cell reactions and standard reduction potentials (E^0) for this displacement reaction are shown below [38]:

$$\text{Anodic reaction: Cu} \rightarrow \text{Cu}^{2+} + 2e^{-},\ E^{0}_{298K} = 0.342\ V_{SHE} \qquad (8)$$

$$\text{Cathodic reaction: Pd}^{2+} + 2e^{-} \rightarrow \text{Pd},\ E^{0}_{298K} = 0.915\ V_{SHE} \qquad (9)$$

During galvanic displacement, Cu atoms diffuse from a Cu substrate to a Pd-Cu deposit due to smaller atomic size of Cu forming Pd-Cu alloy [39].

The metal deposition process via galvanic displacement reaction consists of nucleation and growth steps. Nucleated metal particles on the surface at the initial stage of the reaction grow until fully covering the substrate, which generally results in two-dimensional films as shown in Figure 1.6 [38, 40-42]. Therefore, uniform deposition of catalyst material using galvanic displacement has been performed on 3D-structured templates—such as nanocubes, nanotubes, nanowires and foam structure— to enlarge surface area of catalysts as represented in Figure 1.7 [39, 43-45]. However, it is hard to synthesize a high-surface-area catalyst by galvanic displacement method without going through a preliminary process for template modification to increase its surface area. If a one-pot galvanic displacement method for the synthesis of high-surface-area catalysts can be developed, it can simplify the preparation procedure for catalysts with enhanced catalytic performance.

The electrocatalytic activity of bimetallic catalysts is dependent on the degree of alloying. The atomic ratio of two metals in a catalyst could be tuned by changing the concentration of metal precursors dissolved in a chemical reaction bath for metal deposition methods such as electrodeposition and chemical reaction deposition using reducing agents (Figure 1.8) [46, 47]. In addition, it has been demonstrated that surface composition of bimetallic catalyst can be tailored by manipulating heat treatment condition such as temperature and gas atmosphere (Figure 1.9) [48]. F. Fouda-Onana et al. reported that Pd-Cu electrocatalysts of various compositions have different electrochemical properties for the oxygen reduction reaction (ORR) as shown in Figure 1.10 [49]. The plot between kinetic current for ORR and Cu composition has a volcano-shape and the plot for activation energy as well. Maximum exchange current density and lowest activation energy were found for Cu content between 35% and 55% in Pd-Cu catalyst. It resulted from that the Cu insertion allows an easier OOH_{ads} dissociative adsorption by the lowering of the Pd *d*-band center as Cu content increases due to changed electronic properties. However, as the Cu increases further, back donation bonding between *d*-occupied orbital of Pd-Cu and antibonding orbital of OOH_{ads} weakens, resulting in the slowing down of the ORR kinetic. Therefore, the appearance of maximum catalytic activity in Figure 1.10 is attributed to an optimal *d*-band property that makes easier the OOH_{ads} dissociative adsorption which is considered as chemical rate determining step (RDS) for the ORR.

Therefore, the precise control over surface composition of bimetallic catalysts is critical to obtain the most optimum surface electronic structure and catalytic activity toward electrochemical reaction. In this contribution, composition-tunable galvanic displacement method should be developed to synthesize bimetallic catalysts with the enhanced catalytic activity.

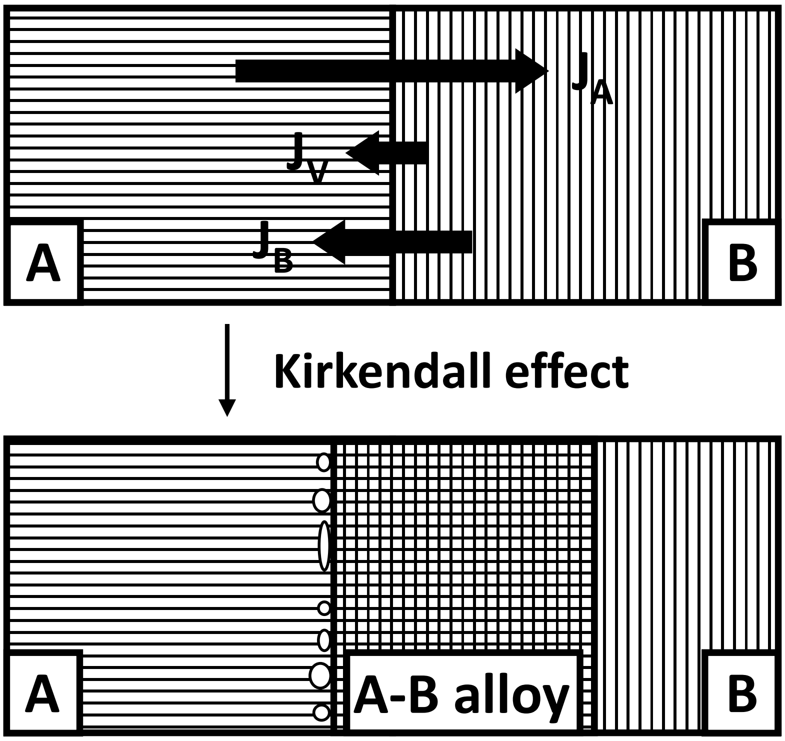

Figure 1.5. Schematic illustration describing a nonequilibrium lattice diffusion at the interface in bulk phase by Kirkendall effect (J_A, J_B, and J_V are diffusion fluxes of metal A, B, and void, respectively) [36].

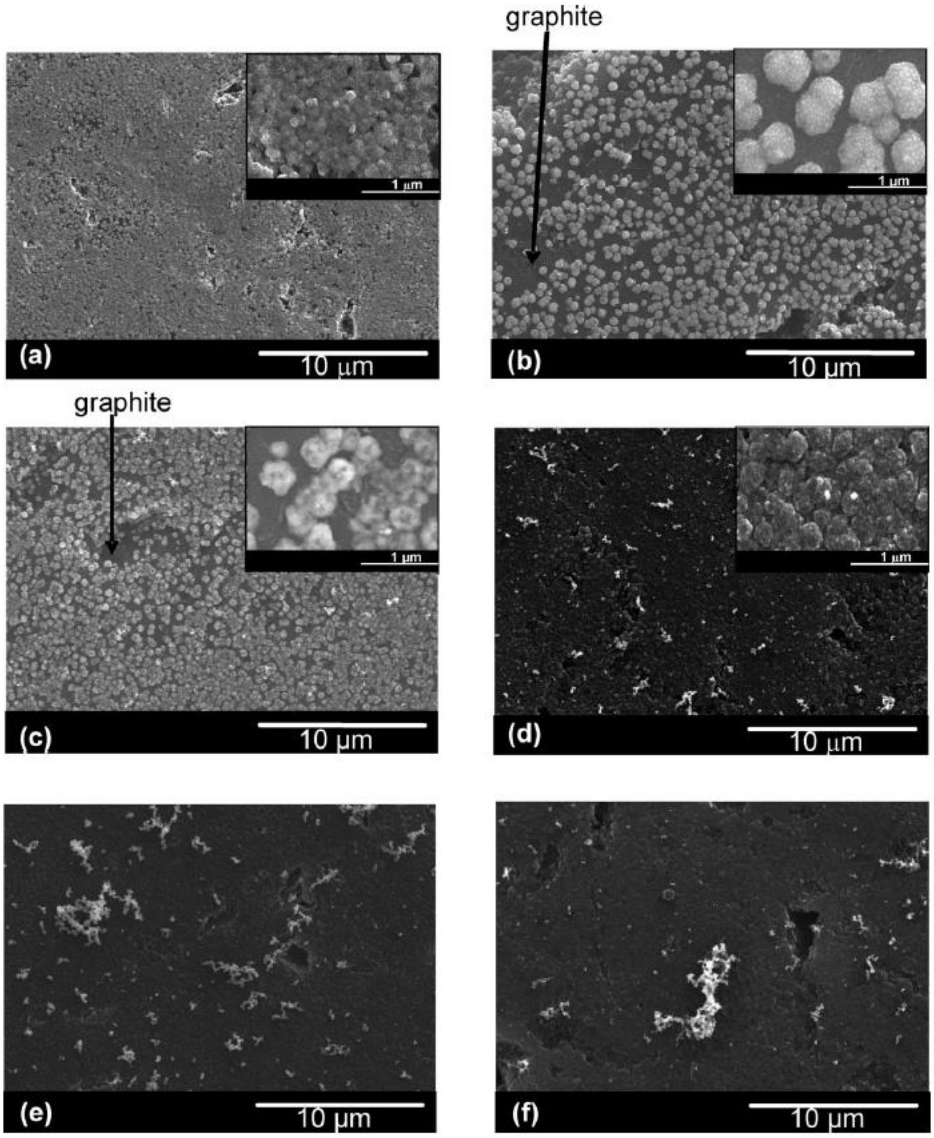

Figure 1.6. (a) SEM images of a Cu/graphite electrode. Cu was deposited in a 0.1 M $Cu(NO_3)_2$ + 1.8 M H_2SO_4 solution at –0.2 V for 20 s; SEM images of Cu-Pd/graphite electrodes, the exchange reaction was performed during 30 s in a $PdCl_2$ + 0.1 M $HClO_4$. The $PdCl_2$ concentration was (b) 1, (c) 3, (d) 5, (e) 7, and (f) 10 mM [38].

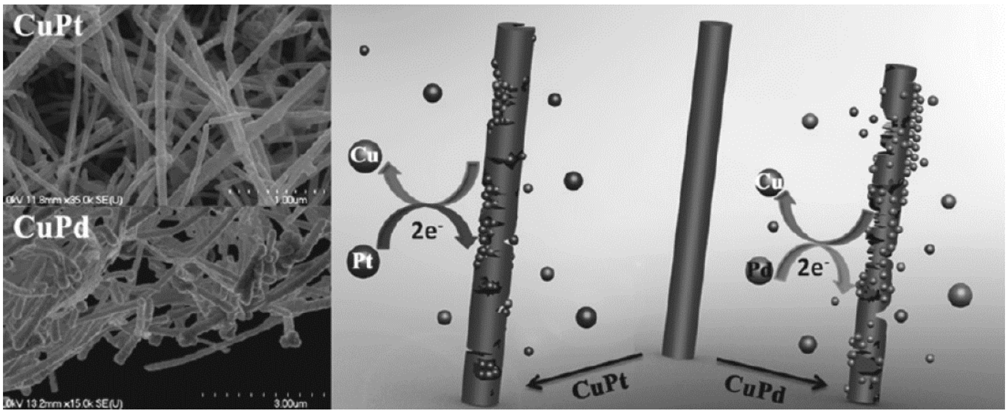

Figure 1.7. Schematic image illustrating the possible formation mechanism of CuPt bimetallic nanostructures and CuPd bimetallic nanotubes from Cu nanowires [39].

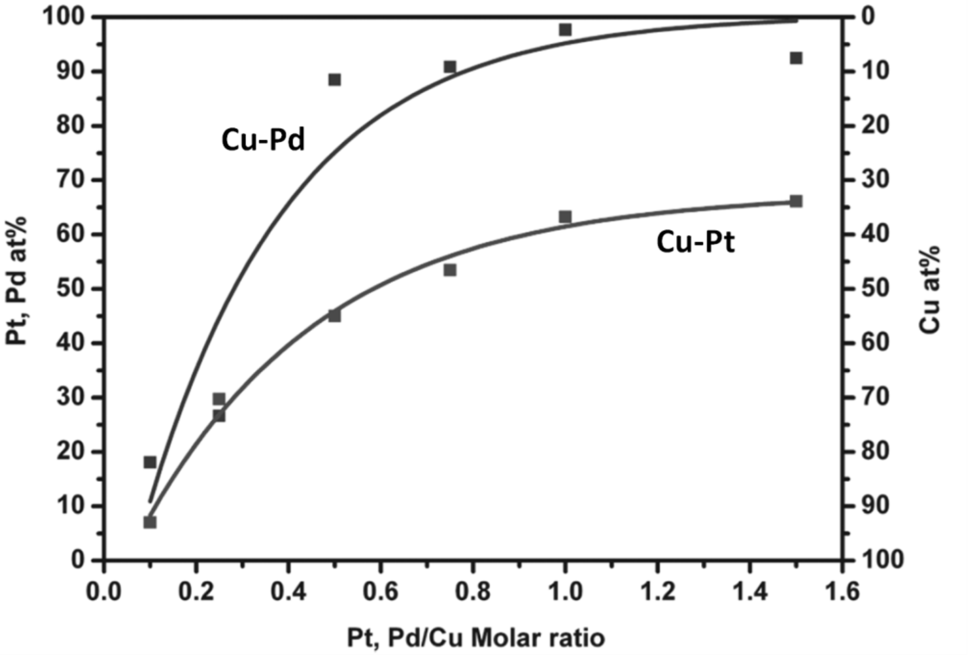

Figure 1.8. Atomic percentage of Cu and Pd, Pt in the product as a function of the molar ratio (K_2PtCl_4, K_2PdCl_4 to Cu) of the reactants [39].

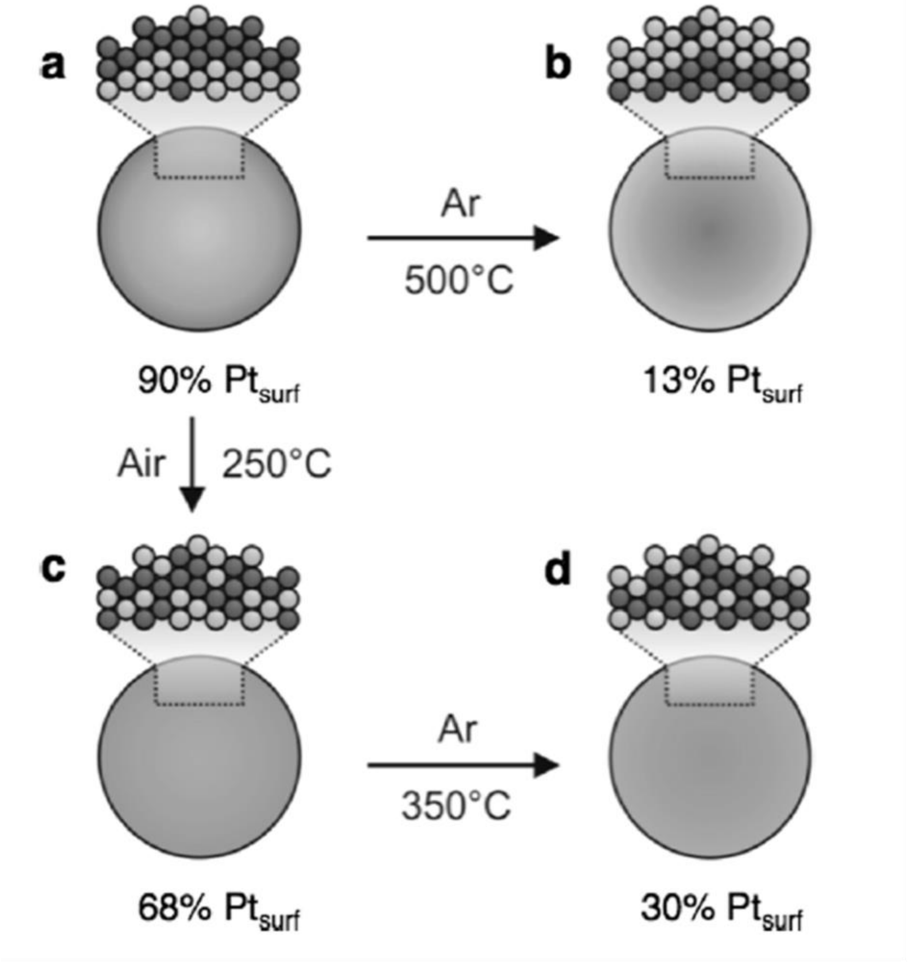

Figure 1.9. Schematic models of $Au_{0.5}Pt_{0.5}$ nanoparticles undergoing surface-energy-driven restructuring upon different thermal treatments. Differential surface energies of Au and Pt in different environments enable adsorbate-driven segregation, which leads to different surface compositions despite all having the same bulk composition [48].

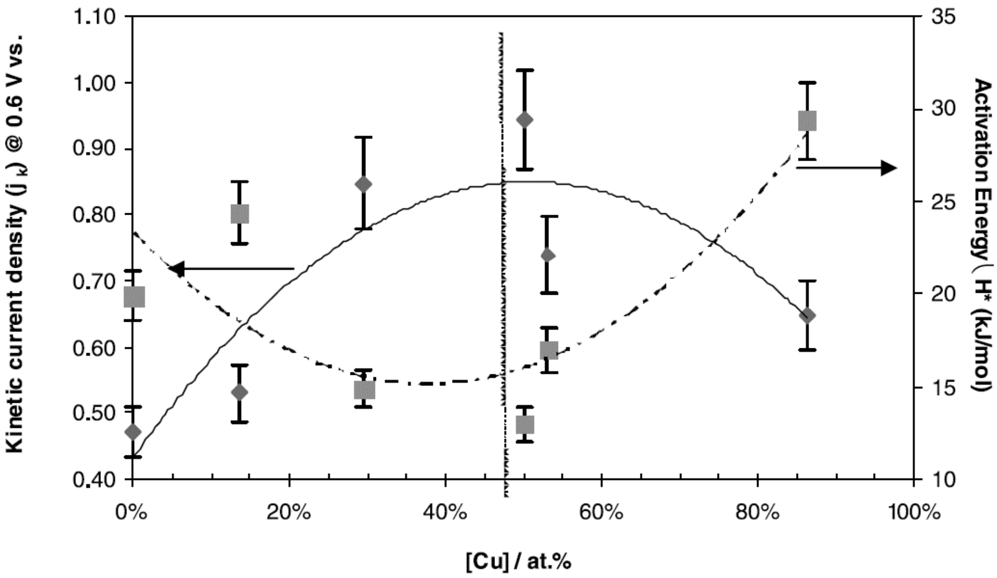

Figure 1.10. Kinetically-controlled current (j_k) and activation energy (ΔH^*) as a function of the bulk composition of the Pd-Cu alloy electrodes [49].

1.3. Couette-Taylor flow mixer in a two-phase gas-liquid system

For electrochemical reactions using gaseous reactants, the solubility of a gaseous substance in an electrolyte solution and its dissolution rate play an important role for efficient reactions, in addition to the activity of catalyst. The solubility of gases in liquids depends upon thermodynamic properties such as pressure and temperature [50-52]. The high pressure of the gas and low temperature of the solution can enhance the gas solubility. The dissolution rate of gas is affected by mass transfer between the gas and the liquid. The gas-to-liquid mass transfer rate, in other words, the gas dissolution rate, can be controlled by mass-transfer coefficient of gas, interfacial area between gas and liquid, and a concentration gradient of dissolved gas. For these reasons, in this study, the system aiming for the enhanced mass transfer at the interface between the bubble and the electrolyte and for the increased gas pressure inside the bubble was developed by employing a Couette-Taylor flow (CTF) mixer. Helicoidal flow in an annular gap of the CTF mixer was generated by the superposition of the axial Poiseuille flow and the rotational Couette flows (Figure 1.11) [53]. In this type of flow, hydrodynamic instability, due to Taylor vortices, emerges when Taylor number (Ta) exceeds the critical value of 41.19 [54-57]. The Ta is defined as the following equations:

$$\mathrm{Ta} = \Omega r_m^{0.5}(r_o - r_i)^{1.5}/\nu \qquad (10)$$

$$r_m = (r_o+r_i)/2 \qquad (11)$$

, where Ω is angular velocity of the inner cylinder, r_m is arithmetic mean radius of the outer (r_o) and inner (r_i) cylinders, and ν is kinematic viscosity of the solution.

The change in Ta number by controlling rotational speed affects the gas-liquid flow pattern as represented in Figure 1.12 [53]. In these regime, either regular rings of bubbles, referred to as ring flow, or irregular rinds is observed, which results from the horizontal orientation of a CTF mixer. As increasing rotational speed, the ring pattern becomes more regular distinctively. However, the distinct ring pattern is disturbed when rotational speed exceeds critical point. With a CTF mixer which was used in this study, same trend was observed as shown in Figure 1.13. With increasing the rotational speed up to 1000 rpm, distinct and regular ring pattern of bubbles appeared, which is characteristic of horizontal CTF mixer for liquid-gas two phase [53]. However, the distinct ring pattern is disturbed when rotational speed exceeds critical point, which is 1500 rpm. In the CTF mixer, the bubbles tend to gather at the outflow boundaries of the Taylor vortices (Figure 1.14). The difference of flow patterns with varying operating condition of CTF mixer is attributed to the different form of streamlines in the Taylor vortices.

S. Wronski et al. investigated the effect of operational parameters of a CTF mixer, such as rotational speed of impeller and liquid axial flow rate, on the gas-liquid flow as shown in Figure 1.15 and 1.16 [58, 59]. The interfacial area between the gas and the liquid which is inversely proportional to bubble size and the volumetric mass transfer coefficient of the gas increased as increasing rotational speed of impeller and liquid axial flow rate. The interfacial area and volumetric mass transfer coefficient first increased due to intense mixing by Taylor vortex until a transition flow pattern was attained on which vortices collapsed and an irregular turbulent flow structure was formed. They also found that interfacial area depended mainly on the rotational speed of impeller while mass transfer coefficient both depended on the rotational speed of rotor as well as on the axial liquid flow rate. Therefore, it can be expected that the control of operational condition for a CTF mixer can enhance N_2O dissolution which can lead to efficient electrochemical reaction of N_2O.

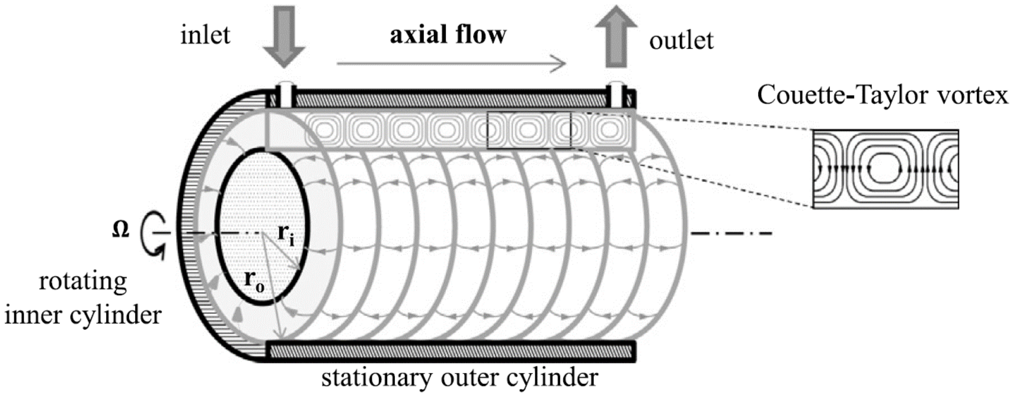

Figure 1.11. The schematic diagram of the Couette-Taylor vortex reactor (CTVR). r_i, r_o, and Ω are the radius of the inner and outer cylinders, and angular velocity of the inner cylinder, respectively [60].

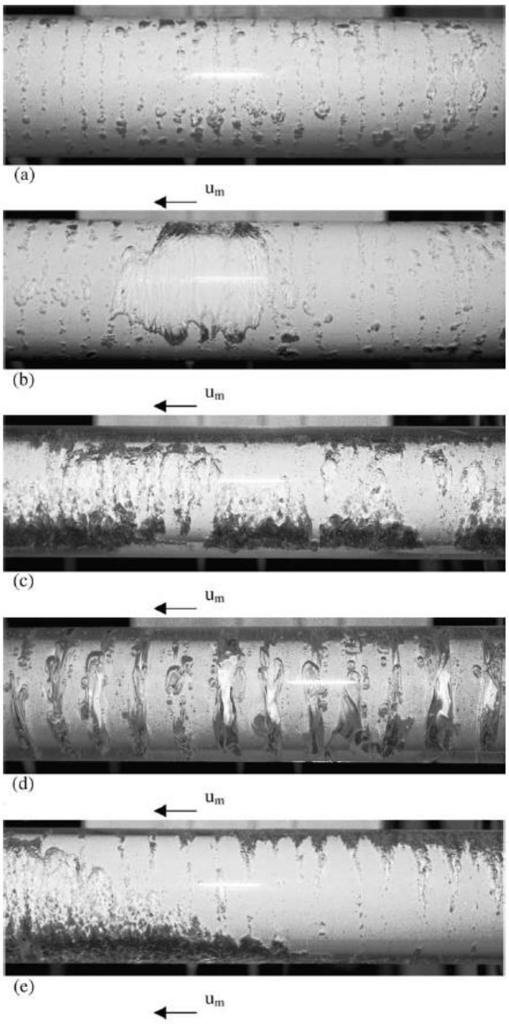

Figure 1.12. Examples of flow patterns in the high rotational speed regime: (a) the ring structure for $\Omega = 110$ s^{-1}, $u_L = 0.0098$ m s^{-1}, $\beta = 1/8$, $\eta = 0.92$, $\mu = 1$ cP; (b) disturbance of the rings for $\Omega = 110$ s^{-1}, $u_L = 0.0098$ m s^{-1}, $\beta = 1/8$, $\eta = 0.92$, $\mu = 1$ cP; (c) $\Omega = 190$ s^{-1}, $u_L = 0.0018$ m s^{-1}, $\beta = 1/8$, $\eta = 0.67$, $\mu = 29$ cP; (d) $\Omega = 136$ s^{-1}, $u_L = 0.0025$ m s^{-1}, $\beta = 1/8$, $\eta = 0.67$, $\mu = 29$ cP; (e) $\Omega = 188$ s^{-1}, $u_L = 0.024$ m s^{-1}, $\beta = 1/4$, η=0.8, $\mu = 1$ cP. u_L is liquid flow rate, β is volumetric flow ratio of gas and liquid, η is ratio of the rotor and outer cylinder diameters, and μ is liquid viscosity [53].

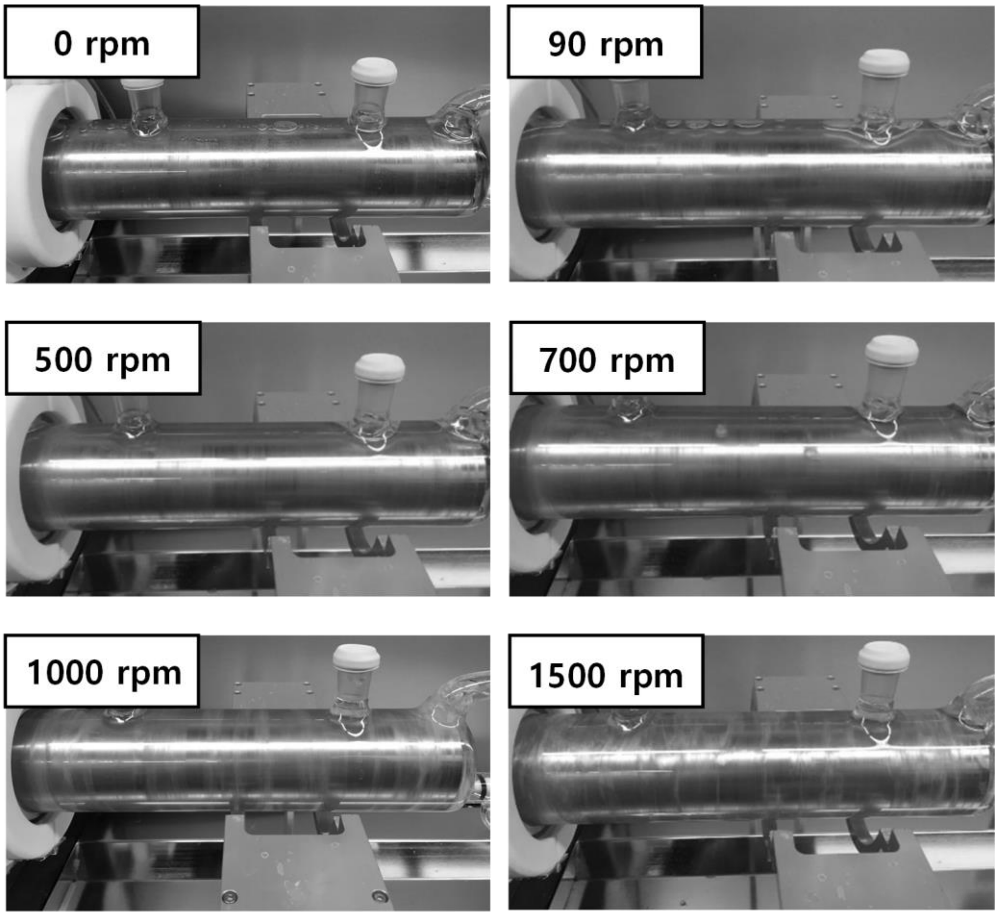

Figure 1.13. Images of flow patterns with various rotational speeds of inner cylinder in a CTF mixer from 0 to 1500 rpm. The flow rates of N_2O and solution were 200 ccm and 150 ccm, respectively. Aqueous solution including 0.3 M K_2SO_4 and 0.2 M KOH was used for N_2O dissolution.

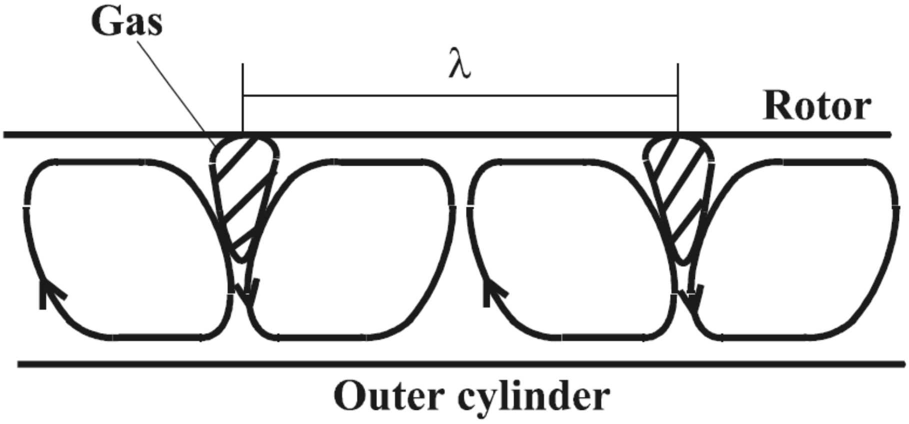

Figure 1.14. Hypothetical Taylor vortex structure in ideal ring flow [53].

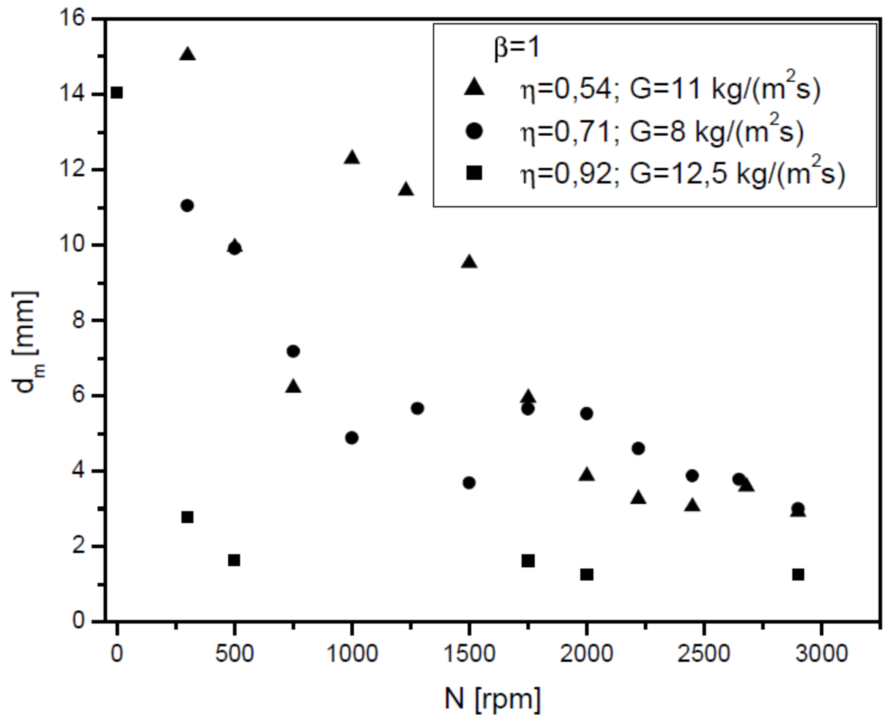

Figure 1.15. Dependence of mean bubble size (d_m) on rotational speed of impeller (N) at different values of η and for β = 1. β is volumetric flow ratio of gas and liquid, η is ratio of the rotor and outer cylinder diameters, and G is liquid axial flow rate [58].

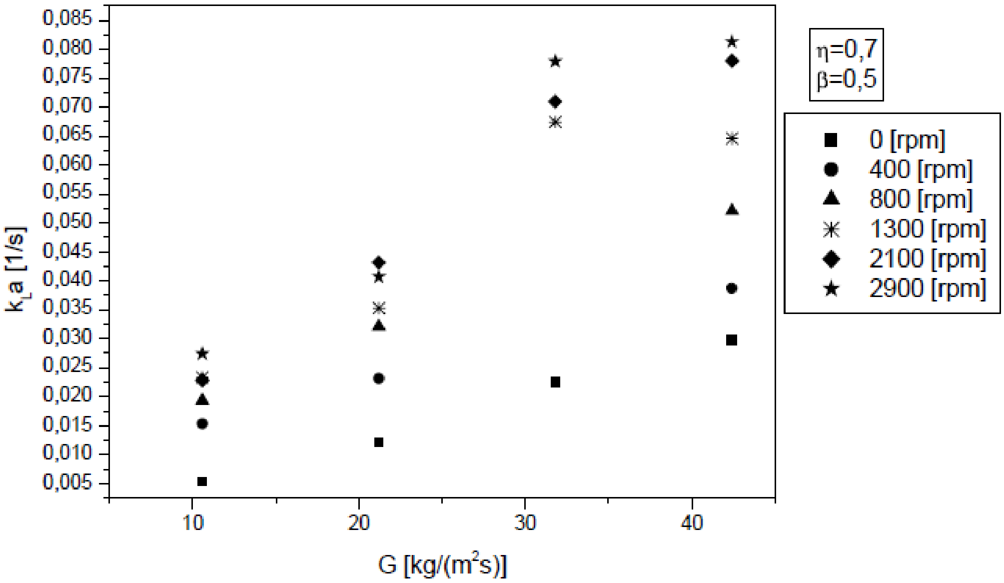

Figure 1.16. Dependence of the volumetric mass transfer coefficient (k_La) on the liquid axial flow rate (G) for η = 0.7 and β = 0.5 [58].

1.4. Combination of electrochemical reactor and Couette-Taylor flow mixer

When an electrolyte solution remained between the inner and outer cylinders of CTF mixer, Taylor vortices are formed in the electrolyte by rotating inner cylinder above critical rotating speed. N_2O dissolution in the electrolyte can be enhanced by Taylor vortices when both electrolyte and N_2O gas are injected into the gap between cylinders.

In this regard, combining electrochemical system and CTF mixer can increase the efficiency of electrochemical N_2O reduction due to high solubility and fast dissolution of N_2O. Therefore, the efficient reduction of N_2O can be performed using the electrochemical reactor-combined CTF mixer due to the intensive mixing by Taylor vortices.

1.5. Purpose of this study

In this study, Pd-Cu catalysts can simply be synthesized via one-step galvanic displacement method. The morphology and chemical composition of Pd-Cu catalysts were modified to enhance their catalytic activity toward electrochemical reactions such as ethanol oxidation and N_2O reduction.

Whisker Pd-Cu catalyst with large surface area was prepared by addition of Cl^- ions in galvanic displacement bath. The mechanism of whisker formation was clarified by confirming the effects of Cl^- ions on the reaction rate and mass transfer of Pd^{2+} ions. A universal method of controlling morphology to whisker or smooth film was applied to the preparation of several noble metal (Pd, Pt, and Au)-based catalysts. Furthermore, electrocatalytic activity of Pd-Cu whisker was tested for ethanol oxidation and the effectiveness of enlarged surface area on enhanced catalytic activity was investigated.

In addition to the control of catalyst morphology, the composition of Pd-Cu catalyst can be tunable using citric acid-assisted galvanic displacement. The Pd/Cu ratio on catalyst surface was controlled by changing the concentration of citric acid, which is incorporated into the deposit and prevents Cu diffusion from the substrate to alloy. The obtained Pd-Cu catalysts such as $Pd_{49}Cu_{51}$, $Pd_{61}Cu_{39}$, $Pd_{66}Cu_{34}$, $Pd_{74}Cu_{26}$, and $Pd_{84}Cu_{16}$ were characterized and evaluated in terms of their electrochemical N_2O reduction performance. The dependence of catalytic activity toward N_2O reduction on chemical composition of Pd-Cu alloy was studied through the DFT calculation.

In addition to enhance catalytic activity, the efficiency of electrochemical reaction was further increased by improving mass transfer property of reactants using a CTF mixer. Taylor vortices which were formed in the electrolyte solution by rotating inner cylinder of a CTF mixer above critical rotating speed could enhance gas dissolution. Therefore, CTF mixer was adopted for efficient N_2O dissolution and the characteristics of N_2O dissolution with the CTF mixer were investigated by changing the operating conditions, including cylinder rotation speed and flow rates of the gas and the liquid. Furthermore, the effectiveness of enhanced N_2O dissolution for electrochemical reduction of N_2O was evaluated by comparing N_2O conversions obtained with applying electrical potential on Pd-Cu catalyst loaded on a CTF mixer with and without rotating inner cylinder, respectively.

CHAPTER II

Experimental

2.1. Fabrication of Pd-Cu catalysts

2.1.1. Synthesis of Pd-Cu whisker catalyst with enlarged surface area

Pd-Cu whisker catalyst was synthesized simply by immersing a Cu substrate in an aqueous solution containing 0.1 M $HClO_4$ (70%, Junsei) and 3 mM $PdCl_2$ (99%, KOJIMA) or 3 mM $PdSO_4$ (99%, Alfa Aesar). A Cu coupon wafer, whose structure was Cu (PVD, 1 μm)/TaN (PVD, 30 nm)/Ta (PVD, 30 nm)/TaN (PVD, 30 nm)/SiO2/Si, was used as the sacrificial substrate. Before galvanic displacement reaction, the Cu substrate was immersed in an aqueous solution of 20.4 mM citric acid (99.5%, Sigma Aldrich) and 35.6 mM KOH (95%, SAMCHUN) for 2 min to eliminate the native Cu oxide. The pretreated wafer was rinsed in deionized water, followed by immersion in the displacement bath. Galvanic displacement was conducted with stationary or 300 rpm-rotating Cu substrate at 25°C. K_2PtCl_4 (99.99%, Sigma Aldrich) or $AuCl_3$ (99.999 %, Sigma Aldrich) (each 3 mM) was also used as a precursor for the Pt and Au displacement, respectively.

2.1.2. Synthesis of Pd-Cu film catalyst with controllable composition

Pd-Cu catalysts with different compositions were formed on Cu foil (99.98%, Sigma-Aldrich) by simply dipping the Cu foil in an aqueous solution containing 3 mM $PdSO_4$ (99.99%, Alfa Aesar) and 0.1 M $HClO_4$ (70%, Junsei). Citric acid (≥99.5%, Sigma-Aldrich) was added in the galvanic displacement bath as an alloy composition controller with adjusting the concentration between 0.1 and 100 mM. In prior to galvanic displacement reaction, the Cu foil was immersed in an aqueous solution of 10 vol% H_2SO_4 and 3 vol% H_2O_2 to remove native Cu oxide. The galvanic displacement reaction was carried out at 25°C for 5 min. Cu foil was rinsed with deionized water to remove residues after pretreatment and displacement reaction.

2.2. Characterization of catalysts

The surface morphology of prepared catalysts was analyzed using field emission-scanning electron microscopy (FE-SEM; Hitachi, S-4800) and atomic force microscopy (AFM; Agilent Technologies, 5100 AFM). The composition of catalysts was analyzed by transmission electron microscopy (TEM; JEM-2100F, JEOL) and energy-dispersive X-ray spectroscopy (EDS; INCA Energy, Oxford Instruments Analytical Ltd.). Crystal information was obtained using an X-ray diffractometry (XRD; Brucker, D8-Advance). X-ray photoelectron spectroscopy (XPS; K-Alpha, Thermo Electron) was utilized to study surface electronic state and chemical composition of Pd-Cu catalysts. The amount of Pd deposited by galvanic displacement was measured by inductively coupled plasma-mass spectrometer (ICP-MS; Varian 820-MS, Varian).

2.3. Electrochemical analysis

All electrochemical experiment was conducted in a three-electrode system containing Pt mesh as a counter electrode and saturated calomel electrode (SCE) as a reference electrode as shown in Figure 2.1 and 2.2. Diffusion coefficient of Pd^{2+} ions was measured using linear sweep voltammetry (LSV) analysis based on previously introduced method [61]. Glassy carbon electrode was used as a working electrode. LSV was performed using glassy carbon electrode as a working electrode in (i) 3 mM $PdCl_2$, 0.1 M $HClO_4$ and (ii) 3 mM $PdSO_4$, 0.1 M $HClO_4$ solution. The scan rate for LSV was between 10 and 100 mV s^{-1}.

In addition, the electrochemically active surface area of Pd disk and whisker electrodes was analyzed by cyclic voltammetry (CV) in 0.5 M KOH aqueous solution. The electrochemical surface area of the Pd-based electrodes was calculated by integrating the charge associated with the reduction of surface Pd oxide as same as the previous method suggested by F. Fouda-Onana et al. [49]. Pd disk electrode was polished carefully with 0.3 and 0.05 μm alumina powders, and it was rinsed by deionized water with ultrasonication after each mechanical polishing step.

Electrochemical detection of N_2O was performed in 0.3 M K_2SO_4 solution which pH was adjusted using KOH (aq). Since the solubility of N_2O in an aqueous solution depends on the temperature and pressure, all experiments were carried out at a constant temperature of 298 K and an ambient pressure of 10^5 Pa. After achieving a steady-state flow with a CTF mixer, the electrolyte solution was purged with N_2O. The concentration of N_2O, dissolved in the solution was determined by CV technique with a scan rate of 50 mV s^{-1}. The CV analysis was performed in the solution extracted from a CTF mixer after N_2O dissolution. The concentration of N_2O was estimated from peak current of N_2O reduction on the steady-state voltammogram.

Figure 2.1. Image of the three-electrode system for electrochemical analysis of the prepared catalysts.

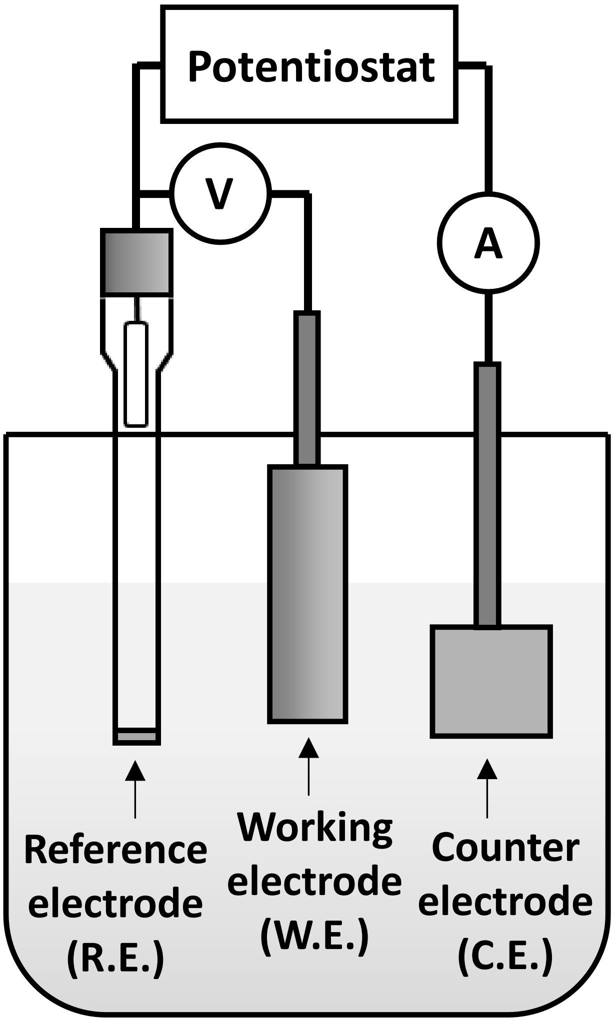

Figure 2.2. Schematic diagram of the three-electrode system for electrochemical analysis of the prepared catalysts.

2.4. Catalytic performance test

2.4.1. Electrochemical ethanol oxidation

The electrocatalytic activity of whisker and Pd disk for the ethanol oxidation reaction was measured by CV in the solution containing 1 M KOH and 1 M ethanol (EtOH; 94.5%, DAEJUNG). The scan rate of CV was 20 mV s^{-1}. Before each measurement, the electrodes were electrochemically pretreated by repeating the CV to obtain the reproducible electrochemical measurements. The long-term stability of electrodes for ethanol oxidation reaction was investigated by a chronoamperometry performed at -0.245 V for 3600 s. The aforementioned electrochemical analyses for ethanol oxidation were conducted with 1600 rpm-rotating working electrodes at 25°C and using a potentiostat (VersaStatII, EG&G).

2.4.2. Electrochemical N_2O reduction

Electrochemical N_2O reduction was performed in the designed H-type cell as shown in Figure 2.3 and 2.4. The N_2O reduction activities of different-composition Pd-Cu catalysts, Pd and Cu foils, and Pd/C catalyst were analyzed through polarization curves obtained in the solution containing 0.3 M K_2SO_4 and 0.2 M KOH after 30 min of N_2O (purity; 99.9%) purging. The scan rate of polarization curve was 5 mV s^{-1}. Since the solubility of N_2O in an aqueous solution depends on the temperature and pressure, all experiments were carried out at a constant temperature of 298 K and an ambient pressure of 10^5 Pa.

Figure 2.3. Image of the H-type cell for electrochemical reduction of N_2O.

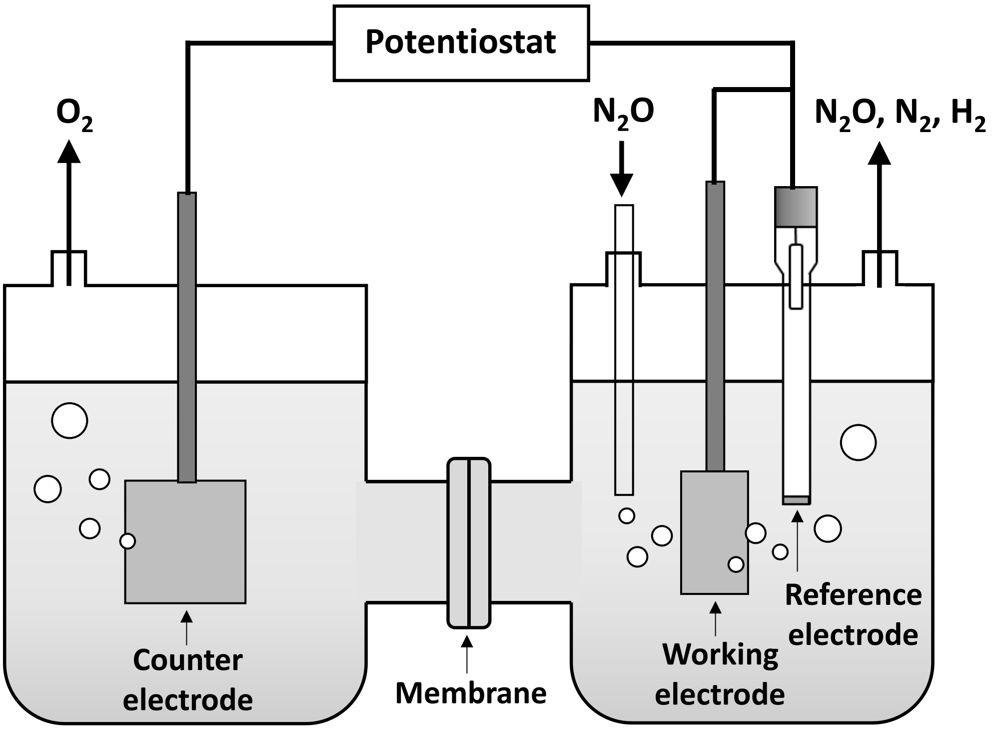

Figure 2.4. Schematic diagram of the H-type cell for electrochemical reduction of N_2O.

2.5. DFT calculation

The DFT calculations using the Vienna *ab initio* Simulation Package (VASP) were tried [62, 63]. Exchange-correlation effects were treated by Perdew-Burke-Ernzerhof (PBE) functional based on generalized gradient approximation (GGA). A plane-wave has been expanded with a cutoff of 400 eV. 4 × 4 × 1 Monkhorst-Pack *k*-point mesh [64] was employed with a (4 × 4) surface unit cell. The conjugate gradient method was used for ionic relaxation. Methfessel–Paxton smearing method was used to treat partial occupancies with a width of 0.2 eV. All structures were relaxed until the force on each atom is less than 0.03 eV/Å with the correction of van der Waals interactions using DFT-D3 [65]. The calculations for gas-phase molecules were conducted in 20 × 20 × 20 Å supercell with 12 × 12 × 12 Monkhorst-Pack *k*-point mesh. The lattice constant of bulk FCC structures of Pd and Cu were optimized to 3.89 and 3.57 Å, which are in good agreement with the experimental values of 3.89 and 3.61 Å, respectively.

For the PdCu surface alloys, the lattice constant and crystal structure of Pd was used. Pd atoms on Pd(111) surface were substituted with Cu atoms with the surface coverages of 0, 1/16, and 1/4 ML. For the pure Cu catalyst, we used Cu(111) with the lattice constant and crystal structure of pure Cu. Since the (111) surface is thermodynamically the most stable, it has been widely used for investigating the activity for N_2O reduction reaction on transition metal surfaces [25, 66]. A three layer slab model with fixed one bottom layer was used to describe the metal surface. The vacuum thickness of 15 Å was used to exclude the self-interaction between the periodic slabs. The adsorption energy (E_{ads}) for each adsorbate was calculated as below;

$$E_{ads} = E_A - E_{surf} - E_{A(g)} \tag{12}$$

where E_A is the total energy of adsorbate-substrate system, E_{surf} is the total energy of bare surface, and $E_{A(g)}$ is the isolated gas-phase molecule, respectively.

2.6. Couette-Taylor flow mixer/electrolysis reactor hybrid system

The N_2O dissolution system, including the CTF mixer (LCTR-Lab II, Laminar) for enhancing gas dissolution, is shown in Figure 2.5 to 2.7. CTF mixer (4) is 25.0 cm long and equipped with a rotor (inner cylinder) with a diameter of 5.25 cm. It has a concentric annular gap of 0.70 cm between the inner and outer cylinders. Two types of outer cylinder were used in experiments as shown in Figure 2.6; glass cylinder was used for observing flow pattern during N_2O dissolution and SUS cylinder was used as a negative electrode to supply electrical energy for N_2O reduction. The inner cylinder was rotated at various rotation speeds between 0 and 1500 rpm. The N_2O and electrolyte were supplied through nozzles with a diameter of 1 cm at the perimeter of the outer cylinder. The feed rates of N_2O were 0.05, 0.10, 0.15, and 0.20 L min^{-1}, which was controlled by mass flow controller (Bronkhorst, F-201CB-500-AAD-00-V). The electrolyte was circulated in a CTF mixer system at flow rates of 0.05, 0.10, 0.15, and 0.20 L min^{-1} which are controlled by a peristaltic pump (Plus Master, PP-150D). For the comparison of N_2O dissolving performance of a CTF mixer, N_2O dissolution was also conducted by bubbling N_2O while stirring with an overhead stirrer in a batch system. Since the solubility of N_2O in an aqueous solution depends on the temperature and pressure, all experiments were carried out at a constant temperature of 298 K and an ambient pressure of 10^5 Pa.

The CTF mixer was combined with electrochemical system to simultaneously reduce

N_2O during dissolution with a CTF mixer as illustrated in Figure 2.7. The dissolved N_2O was electrochemically reduced by applying potential at 3.5 V with a DC power supply (XG 33-25, Sorensen) to inner and outer cylinders. Pd-Cu whisker catalyst was loaded on Cu foil by immersing the foil in the solution containing 3 mM $PdCl_2$ and 0.1 M $HClO_4$ for 30 min. The catalyst-loaded Cu foil was attached to the outer cylinder of a CTF mixer for N_2O reduction. The gases exiting the CTF mixer were transferred directly into a gas chromatography (GC, HP5890, Hewlett-Packard) system, using He carrier gas, to measure the concentrations of product gases. The N_2O conversion was evaluated based on the following Equation (13):

$$N_2O\ \text{conversion} = (Q_iX_i - Q_oX_o) \times 100 / Q_iX_i \qquad (13)$$

, where Q_i and Q_o are inlet and outlet flow rates and X_i and X_o are inlet and outlet N_2O concentrations measured by GC.

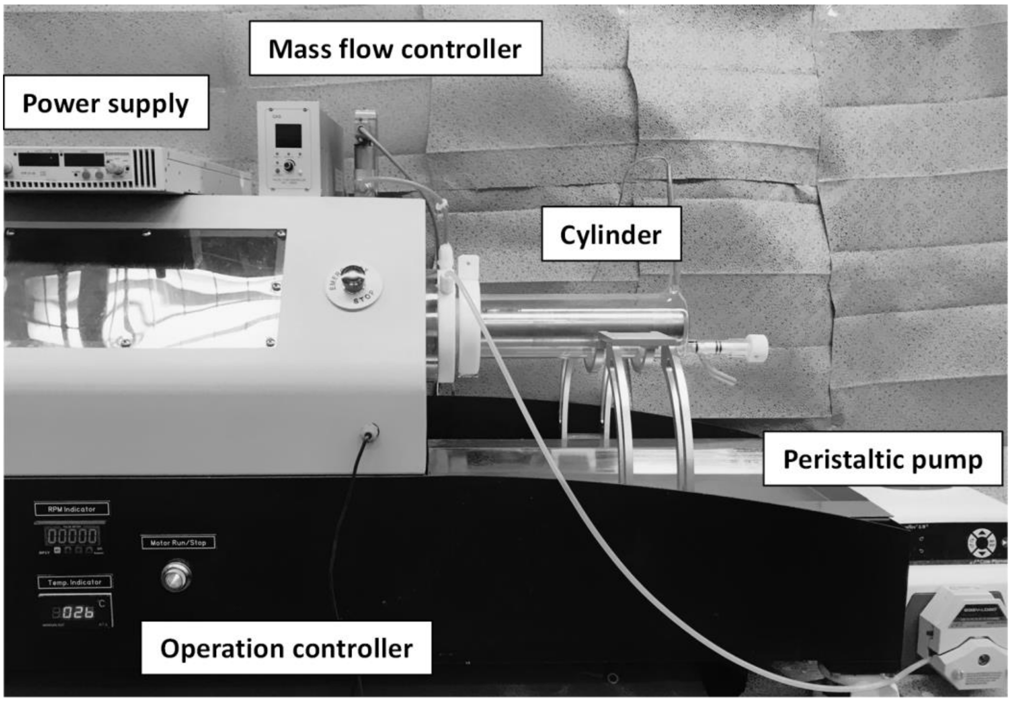

Figure 2.5. Image of CTF mixer/electrolysis reactor hybrid system for dissolving and reducing N_2O.

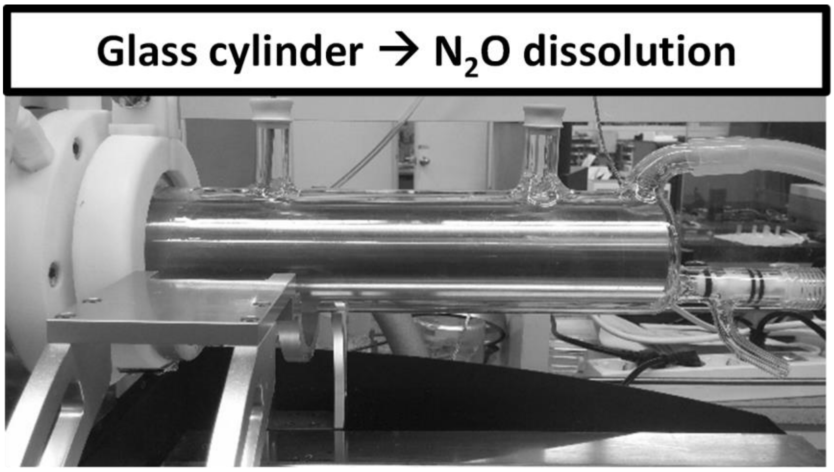

Glass cylinder → N_2O dissolution

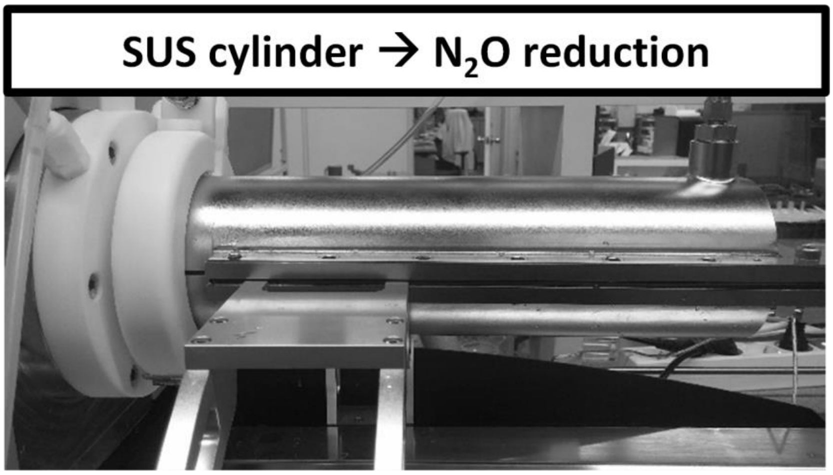

SUS cylinder → N_2O reduction

Figure 2.6. Image of CTF mixer with two types of outer cylinders.

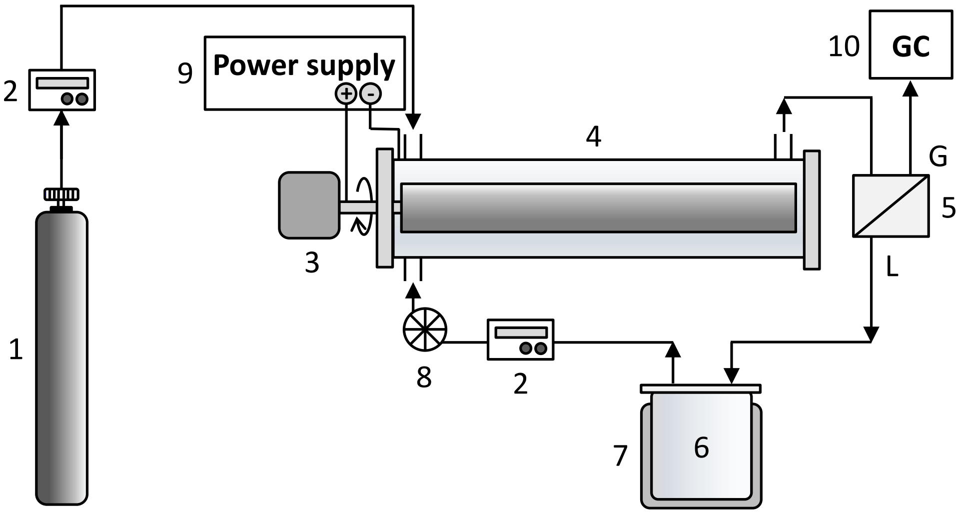

Figure 2.7. Schematic diagram of CTF mixer/electrolysis reactor hybrid system for dissolving and reducing N_2O: (1) gas cylinder, (2) mass flow controller, (3) motor, (4) CTF mixer, (5) gas-liquid separator, (6) bath with outlet solution, (7) cooling jacket, (8) peristaltic pump, (9) power supply, and (10) gas chromatography.

CHAPTER III

Results and Discussion

3.1. Morphology-controlled synthesis of Pd-Cu catalyst via galvanic displacement deposition

3.1.1. Synthesis of Pd-Cu whisker catalyst with enlarged surface area

The dendritic growth of metal deposit using electrodeposition has been achieved by depleting the metal ions near the electrode surface with high deposition rate, i.e. under the mass transfer-limited condition. The metal ions transporting from the bulk electrolyte to the electrode surface are in turn reduced at the end of dendrites [67]. That is, the mass transport of metal ions and their concentration gradient during deposition can change the morphology of the metal deposit. In galvanic displacement, two electrochemical reactions take place: dissolution of the sacrificial substrate (oxidation reaction) and deposition of the noble metal (reduction reaction), and the rates of both reactions should be identical. Therefore, it is possible to control the morphology of metal deposit by modifying the rates of electrochemical reaction and mass transfer of noble metal ions, similar to the case of electrodeposition. The addition of Cl^- ions is one of the ways to change the rate of the electrochemical reaction because the dissolution of Cu can be accelerated by Cl^- ions, leading to an increase in the reduction rate of Pd. K. Zhuo et al. reported that dendritic nanoporous nickel oxides were prepared by galvanic displacement reaction with Cl^- ion as an accelerator [68]. In addition, the mass transfer of metal ions can be modified: (i) by changing the diffusion rate of Pd^{2+} ions with modification of the complex form between Pd^{2+} ions and counter anions and (ii) by simply rotating the substrate during the reaction. Therefore, the effects of aforementioned variables on the morphology of Pd deposit were firstly investigated.

The deposit morphologies according to Pd precursors and substrate rotation during the reaction are shown in Figure 3.1. The rotation of Cu substrate was for promoting the mass transport of Pd^{2+} ions, resulting in less development of a concentration gradient of Pd^{2+} ions during the displacement reaction. Although the Cu substrates used in this study were smooth and free from defects (Figure 3.1(a)), cavities were formed in Cu substrate by galvanic displacement, regardless of solution composition and substrate rotation. These cavities originated from oxidation reaction of Cu during galvanic displacement. Cavities in Cu substrate were formed by diffusion of Cu atoms into the deposit to be oxidized and dissolved out, which is known as Kirkendall effect. Therefore, the depth of cavity can be used as an indicator of reaction degree. In contrast, the structure of deposited metal depended on the solution composition and substrate rotation. As shown in Figure 3.1(b), whisker-type deposits were formed in $PdCl_2$ solution without rotation. However, when the substrate rotated during the displacement reaction, a flat and smooth deposit with no whiskers was observed (Figure 3.1(c)). Also, displacement in $PdSO_4$

solution instead of $PdCl_2$ solution resulted in the formation of planar deposit even without substrate rotation (Figure 3.1(d)). This suggested that Cl^- ions and the rotation of substrate (i.e. mass transport of Pd^{2+} ions during the reaction) play a critical role to determine the final morphology of metal deposited by galvanic displacement.

To investigate changes in morphology over reaction time, the reaction time was increased from 30 s to 30 min. Figure 3.2 shows the changes in the morphology of metal deposit according to the reaction time. The height of whiskers and the depth of cavities measured from these images are presented in Figure 3.3. At the initial stage of displacement reaction (30 s), the aggregated particles were formed with small cavities in Cu substrate. As the reaction proceeded, whiskers started to grow from the aggregated particles, and their height continuously increased with increasing cavity depth. The morphological change of Pd deposits from $PdSO_4$ solution over reaction time is shown in Figure 3.4, and the change in the cavity depth is presented in Figure 3.5. Planar film was observed with gradual increases in both the thickness of film-type deposit and the cavity in Cu substrate. Interestingly, the growth rate of cavity in $PdSO_4$ solution was much lower than that in $PdCl_2$ solution. Since the formation of cavities originates from the anodic reaction of Cu, the reduction rate of Pd, which is identical to the rate of coupled-oxidation reaction, can be surmised from the size of cavities. It revealed that the reduction rate of Pd in the presence of Cl^- ion was found to be much faster than that in the presence of SO_4^{2-} ion. Therefore, it can be suggested that Cl^- ions could accelerate the galvanic displacement reaction and form vertically-grown deposit (whisker) due to deficient Pd^{2+} ion supply. In contrast, the substrate rotation could suppress the formation of steep concentration gradient of Pd^{2+} ion by promoting Pd^{2+} ion diffusion and lead to the formation of film-type deposit.

The characteristics of whisker catalyst were investigated. The EDS line-scanning and mapping results of Pd and Cu components are shown in Figure 3.6(a-c) and they indicate that the whisker contained a markedly higher Pd content than the surrounding planar region. It suggests that most Pd^{2+} ions, moving from the bulk solution to the surface of substrate, contributed to whisker formation. On the XRD pattern of the whisker in Figure 3.6(d), two diffraction peaks were observed between 40^{o} and 43^{o} of two-theta, corresponding to pure Pd (111) and PdCu (111). In addition, HR-TEM image of whisker, as shown in Figure 3.7, revealed that the d-spacing of adjacent lattice fringes of the whisker is 0.218 nm which is between the lattice distances of pure Pd (0.224 nm) and pure Cu (0.208 nm), meaning that PdCu alloy was formed during galvanic displacement [69, 70]. The formation of PdCu alloy during galvanic displacement was further confirmed by STEM-EDS analysis (Figure 3.8). The EDS line-scan of a whisker in the vertical direction reveals that the whisker consisted of PdCu alloy and the Pd concentration increased from the bottom to the top of the whisker. The compositional and structural information of the whisker in Figure 3.6-3.8 indicates that Pd^{2+} ions reaching the surface contributed to whisker growth in the absence of agitation. In addition, the concentration gradient of Pd^{2+} ions near the substrate, which is formed during galvanic displacement, could result in the gradually-increasing Pd content in the vertical direction of a whisker.

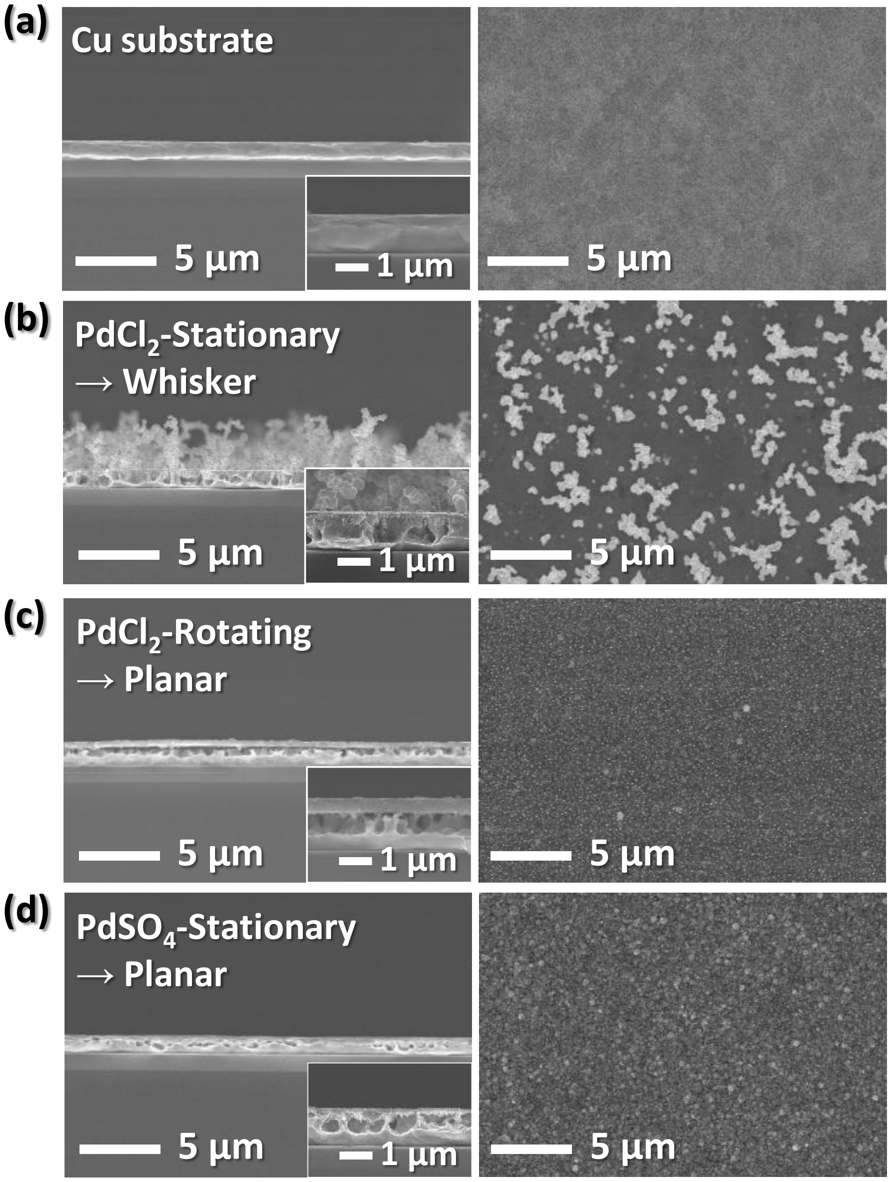

Figure 3.1. Surface and cross-sectional FE-SEM images of (a) Cu substrate and Pd-Cu deposits prepared by galvanic displacement reaction (b, c) in the $PdCl_2$ solution and (d) in the $PdSO_4$ solution. The substrate remained (b, d) stationary for 30 min or (c) rotating at 300 rpm for 2 min during the reaction.

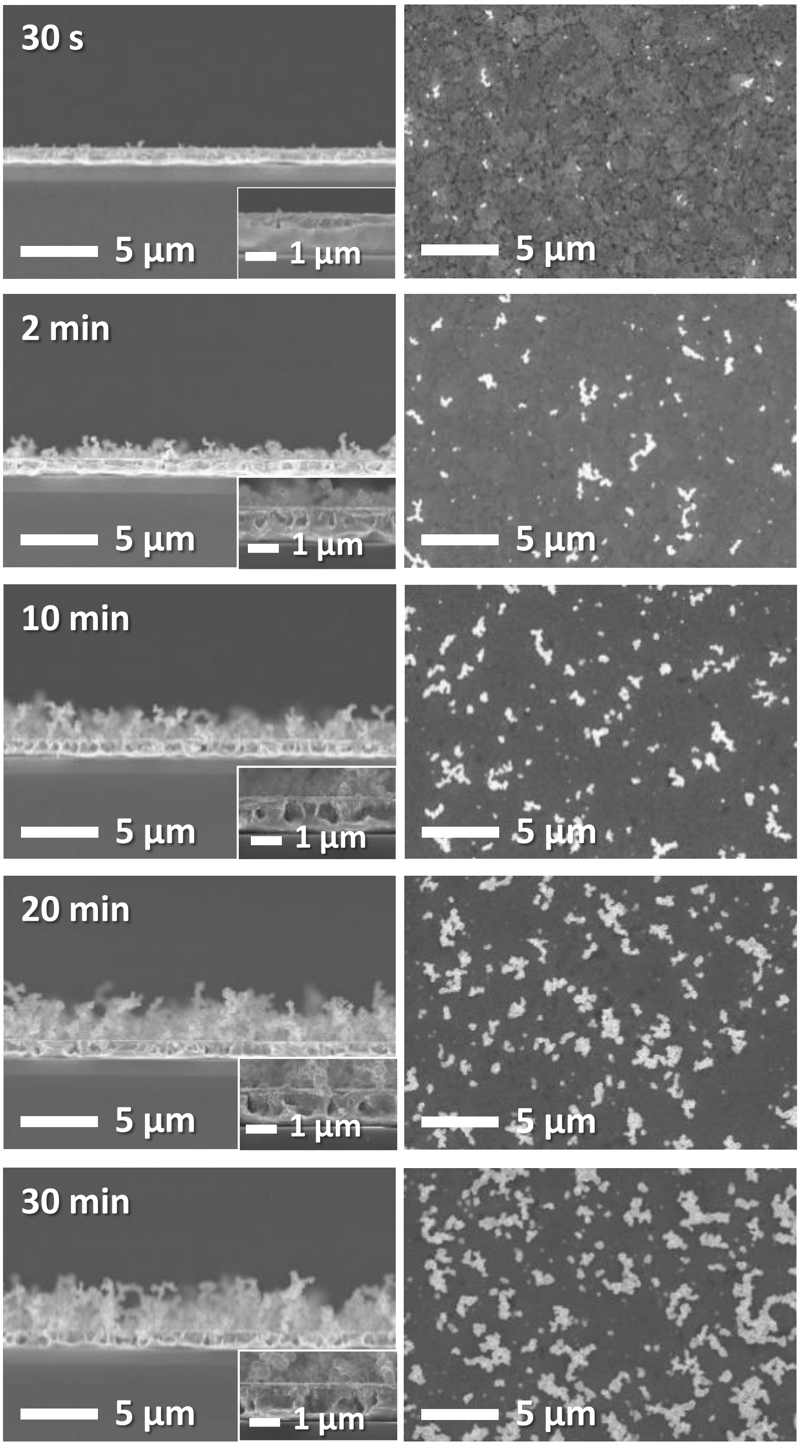

Figure 3.2. Surface and cross-sectional FE-SEM images of Pd-Cu deposits after galvanic displacement in $PdCl_2$ solution without forced convection according to reaction time.

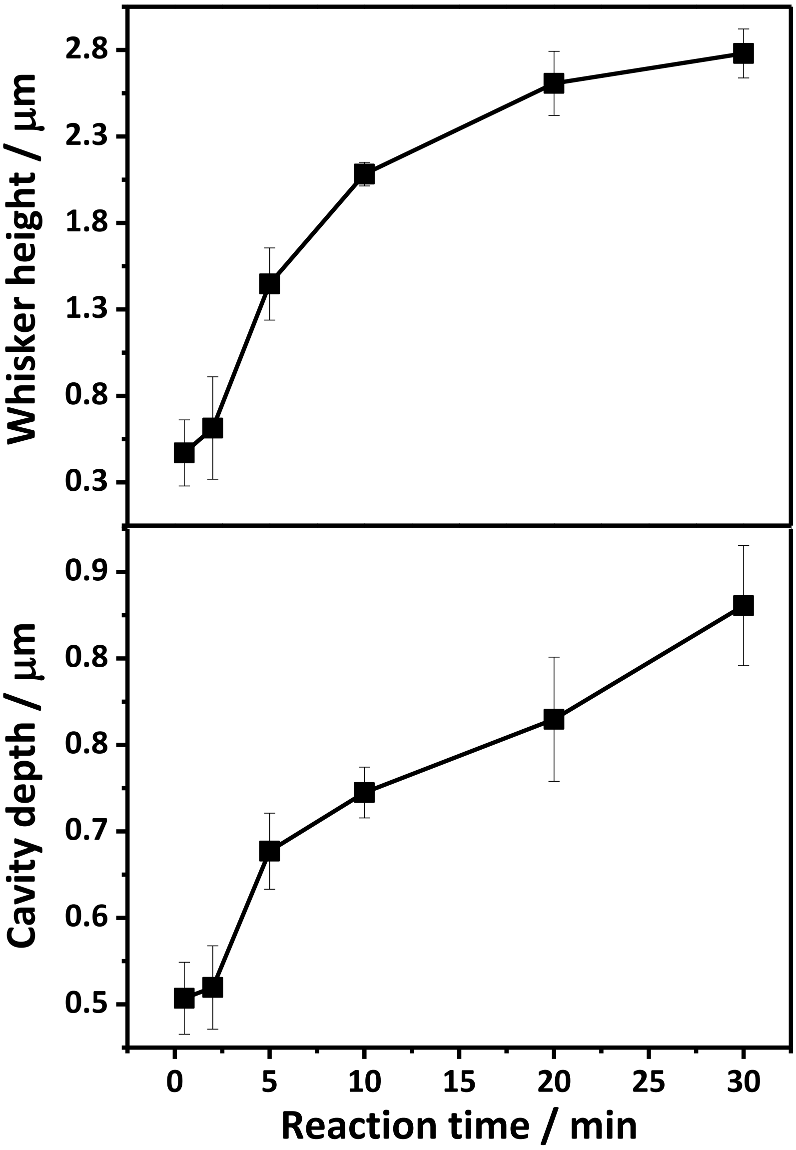

Figure 3.3. The changes in the whisker height and cavity depth with reaction time. The whisker height and cavity depth were measured from Figure 3.2.

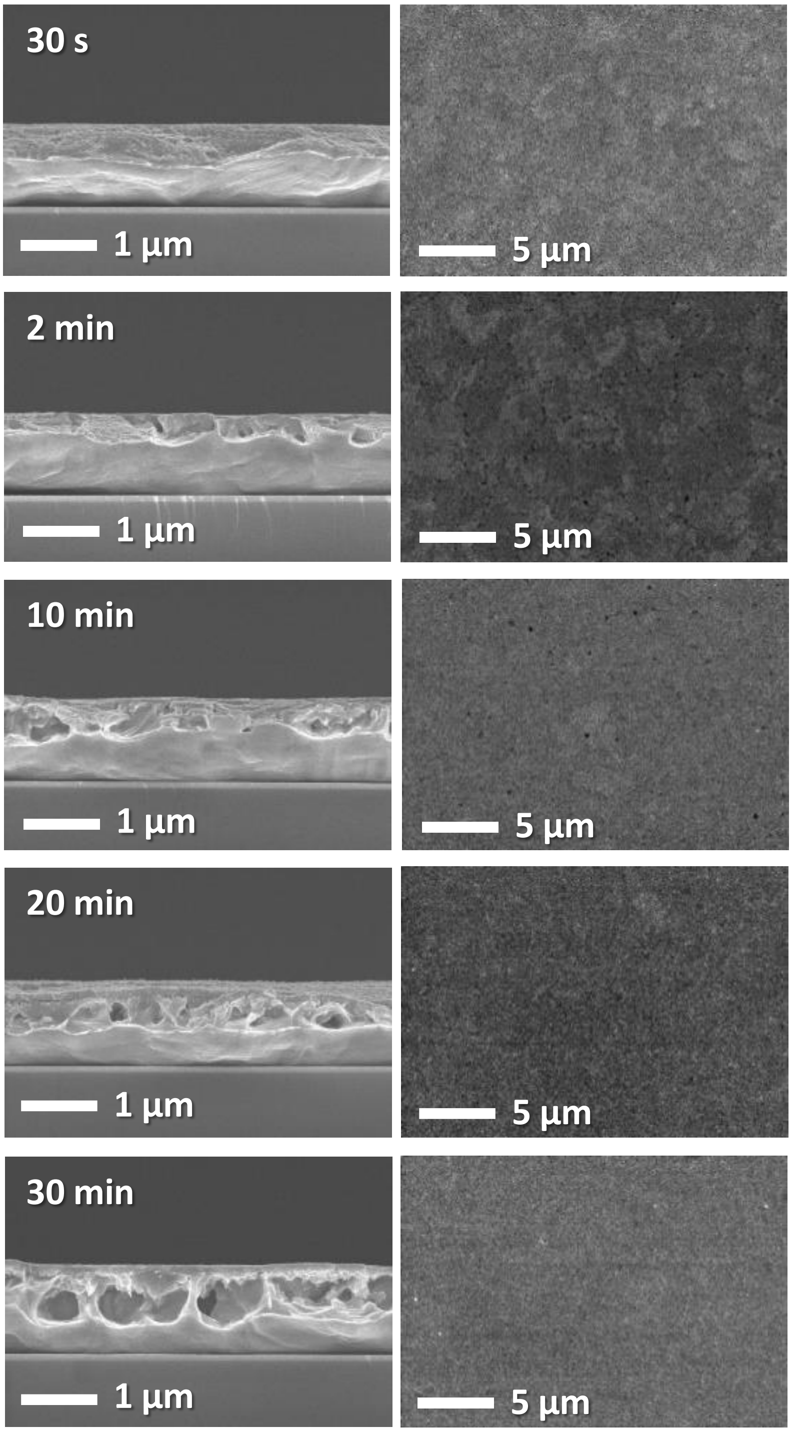

Figure 3.4. Surface and cross-sectional FE-SEM images of Pd-Cu deposits after galvanic displacement in $PdSO_4$ solution without forced convection according to reaction time.

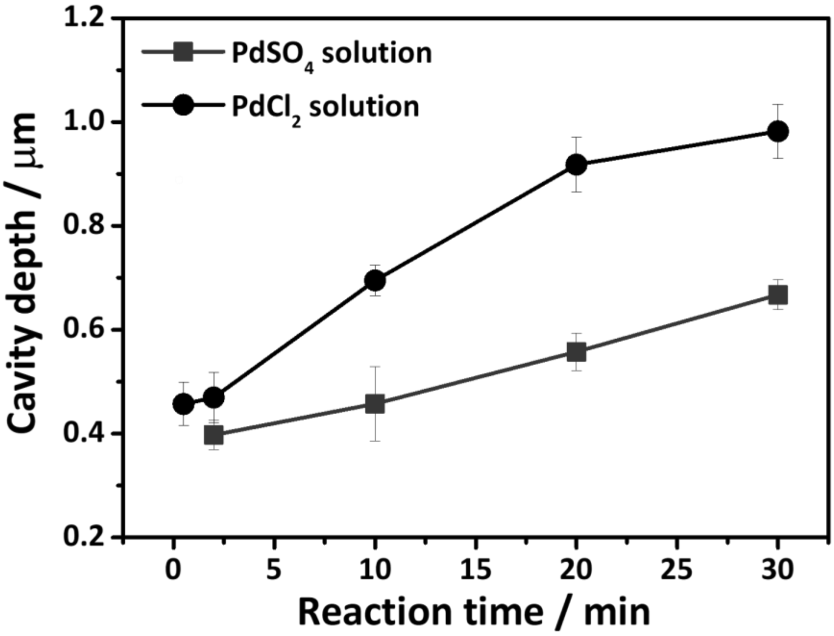

Figure 3.5. The changes in the cavity depth according to reaction time in 3 mM $PdCl_2$ (circle) and 3 mM $PdSO_4$ (square) solutions. The depth of cavity formed with $PdSO_4$ or $PdCl_2$ solution was measured from Figure 3.2 and 3.4, respectively.

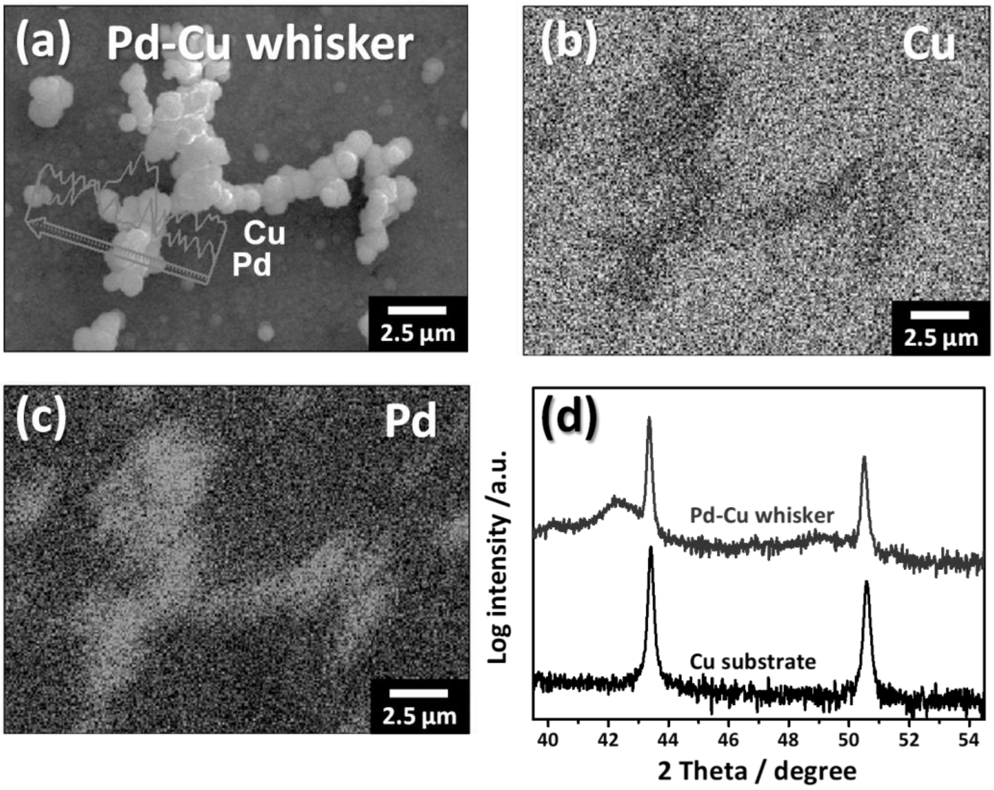

Figure 3.6. (a) FE-SEM image with EDS line-scan, corresponding EDS mapping images of Pd-Cu whisker for (b) Pd and (c) Cu elements, and (d) XRD patterns of pristine Cu substrate and Pd-Cu whisker.

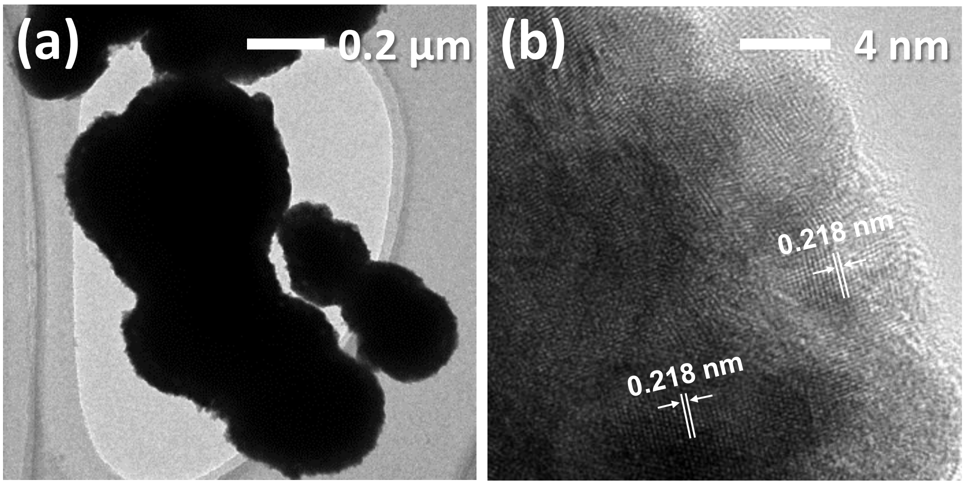

Figure 3.7. Representative TEM images of Pd-Cu whisker.

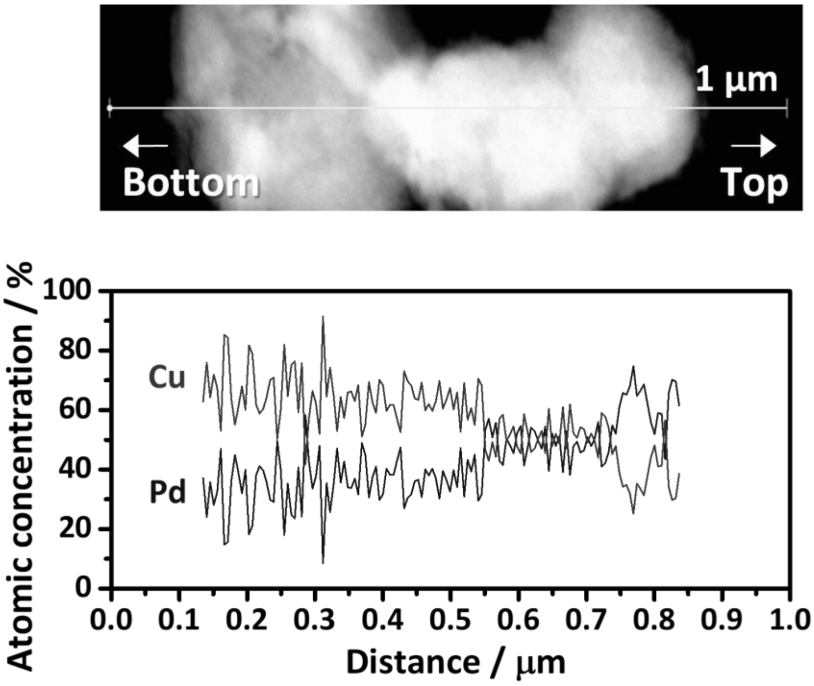

Figure 3.8. TEM image of a whisker with corresponding line profiles of elemental composition analyzed by STEM-EDS.

3.1.2. Mechanism of whisker formation

The effects of the presence of Cl^- ion and the rate of Pd^{2+} ion diffusion on the controllable deposit morphology were investigated in the aspect of kinetics of galvanic displacement reaction. As depicted in Figure 3.5, the size of cavities formed with the solution containing SO_4^{2-} ions were smaller than that formed with Cl^- ions-containing solution. It suggested that Cl^- ions increased the reaction rate of galvanic displacement. The effect of Cl^- ion on the dissolution of Cu was examined by adding various concentration of NaCl to the galvanic displacement bath (Figure 3.9). The whisker height and cavity depth measured from the FE-SEM images were summarized in Figure 3.10. The increasing whisker height and cavity depth indicates that Cu dissolution; i.e., the oxidation reaction during galvanic displacement, was accelerated by Cl^- ion, and resulted in huge cavities within the Cu substrate. Cu oxidation accelerated by Cl^- ion can proceed according to the following equations [71, 72]:

$$Cu + Cl^- \leftrightarrow CuCl_{ads} + e^- \qquad (14)$$

$$CuCl_{ads} + Cl^- \leftrightarrow CuCl_2^- \qquad (15)$$

This acceleration of oxidation reaction can promote the deposition of Pd which is a coupled reduction reaction in galvanic displacement. The accelerated consumption of Pd^{2+} ion led to development of rapid concentration gradient of Pd^{2+} ions, which enhanced vertical growth of Pd because Pd is more readily deposited at the end of whiskers than at the side or on substrate. This was supported by the height of whisker increased with higher concentration of Cl^- ion at the same reaction time.

The diffusion rate of Pd^{2+} ions can be affected by a type of counter anion in Pd precursor due to different complex forms of Pd^{2+} ions. The complex form of Pd^{2+} ions could determine the mass transfer rate of Pd^{2+} ion from the bulk solution to the substrate surface, and this might have an additional effect on whisker formation. If the Pd^{2+} ion in coordination with Cl^- ions has lower diffusivity, the effect of fast corrosion on the development of steep concentration gradient of Pd^{2+} ion becomes more significant than the case with SO_4^{2-} ions. That is, the planar deposit can be obtained with more rapid diffusion of Pd^{2+} ions by maintaining higher concentration of Pd at the substrate surface. Therefore, CV was performed to determine the diffusion coefficients of Pd^{2+} ions forming different complexes with Cl^- and SO_4^{2-} ions at various scan rates between 10 and 100 mV s^{-1} (Figure 3.11). The cathodic peak around 0.1 V (vs. SCE) corresponding to the reduction of Pd^{2+} ions was increased and negatively shifted with increasing scan rate, indicating that the reduction of Pd^{2+} ions on glassy carbon electrode is irreversible [73]. αn_α can be determined from the shift in peak potential (ΔE_p) for 10-fold increase in scan rate, 10 and 100 mV s^{-1}, by using the following Equation (16):

$$\Delta E_p = 1.15RT/\alpha n_\alpha F \qquad (16)$$

, where α is the charge transfer coefficient and n_α is the number of electrons in the rate-determining step. A linear relationship between cathodic peak current (I_P) and the square root of the scan rate ($\nu^{1/2}$) is shown in the inset to Figure 3.11(a-c), which indicated that the Pd reduction reaction was controlled by diffusion for the conditions examined in this study. Therefore, the diffusion coefficient can be estimated from the Equation (17), used for the irreversible process:

$$I_p = 0.4598nFC_o^{*}AD^{1/2}(\alpha n_\alpha F\nu/RT)^{1/2} \tag{17}$$

, where n is the number of exchanged electrons, C_o^{*} is the Pd^{2+} ion concentration, A is the electrode area and D is the diffusion coefficient. Diffusion coefficients of the Pd^{2+} ions in the $PdCl_2$ and $PdSO_4$ solutions, calculated from Figure 3.11(a) and (b), were found to be 1.36×10^{-8} cm^2 s^{-1} and 4.59×10^{-8} cm^2 s^{-1}. The diffusion coefficient of Pd^{2+} ions, calculated from Figure 3.11(c), decreased to be 1.03×10^{-8} cm^2 s^{-1} when 6 mM of NaCl was added in $PdSO_4$ solution. UV-Vis spectra on Figure 3.11(d) showed that the decreased diffusion coefficient in Cl^- ions-containing solution was due to the complex formation between Pd^{2+} ions and Cl^- ions [74]. The higher diffusion coefficient in $PdSO_4$ solution resulted from the hydrated Pd^{2+} ions with weak coordination with the counter anion, SO_4^{2-} [75], which did not severely diminish the diffusion of Pd^{2+} ions. On the contrary, the slow diffusion of Pd-Cl complex led to the relatively easy depletion of Pd^{2+} ions near the surface (i.e. the formation of a large concentration gradient of Pd^{2+} ions during displacement).

The mechanism for whisker formation during galvanic displacement is summarized in Figure 3.12. Cl^- ion accelerates the oxidation reaction of Cu which promotes the reduction reaction of noble metal ions. Furthermore, the diffusion of the complex between metal ion and Cl^- ion is slower than metal-SO_4 complex. Therefore, the steep concentration gradient is developed with the presence of Cl^- ion during the galvanic displacement reaction, and the reduction reaction of noble metal ions becomes mass transfer-limited. As a result, the whiskers could grow from the aggregated particles on the surface and the large concentration gradient of metal ions could induce the metal ions to easily be reduced at the edge of the whiskers where the metal ions are well supplied from the bulk solution. On the contrary, when the development of steep concentration gradient is suppressed by rotating the substrate or using a SO_4^{2-}-containing Pd precursor, the planar catalyst is formed on the substrate instead of whisker-shaped catalyst as shown in Figure 3.1(c) and (d).

The validity of the suggested synthetic method for whisker formation using one-step galvanic displacement was confirmed with Pt- and Au-whisker formation (Figure 3.13). Whisker formation by galvanic displacement was attributed to development of a concentration gradient. Therefore, Pt and Au displacement was conducted using a metal precursor containing Cl^- counter anion with or without rotating the substrate. As expected, in the absence of rotation, whisker-type Pt-Cu and Au-Cu catalysts were obtained with large cavities within the Cu substrate. In contrast, flat and smooth Pt-Cu and Au-Cu were deposited with substrate rotation. These results suggest that this galvanic displacement method of controlling the surface morphology is not limited by the kind of metal to be deposited.

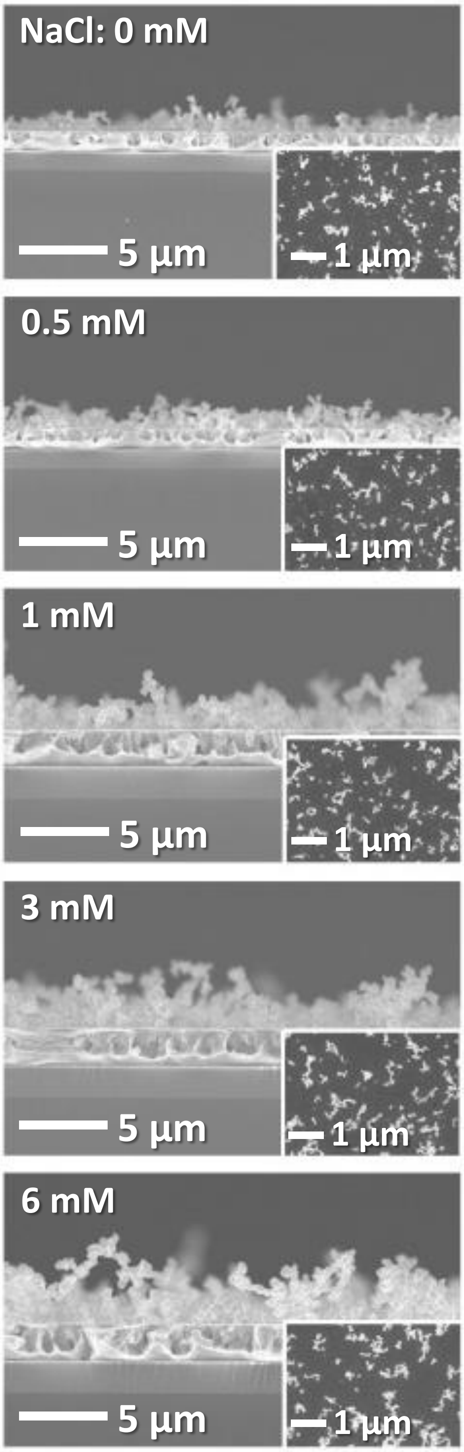

Figure 3.9. Surface and cross-sectional FE-SEM images of Pd-Cu deposits after galvanic displacement in $PdCl_2$ solution with varying the concentration of NaCl. The reaction was performed without substrate rotation for 5 min.

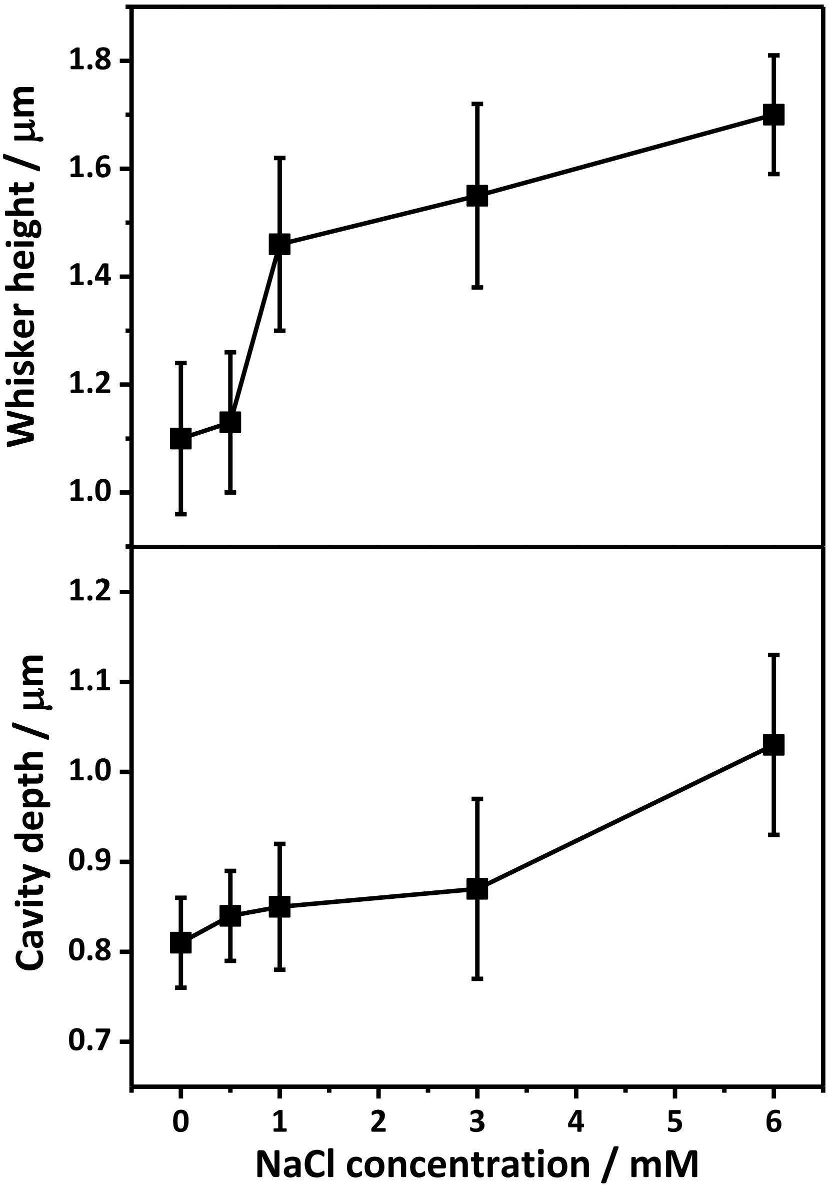

Figure 3.10. The changes in the whisker height and cavity depth with the concentration of NaCl in the $PdCl_2$ solution. The whisker height and cavity depth were measured from Figure 3.9.

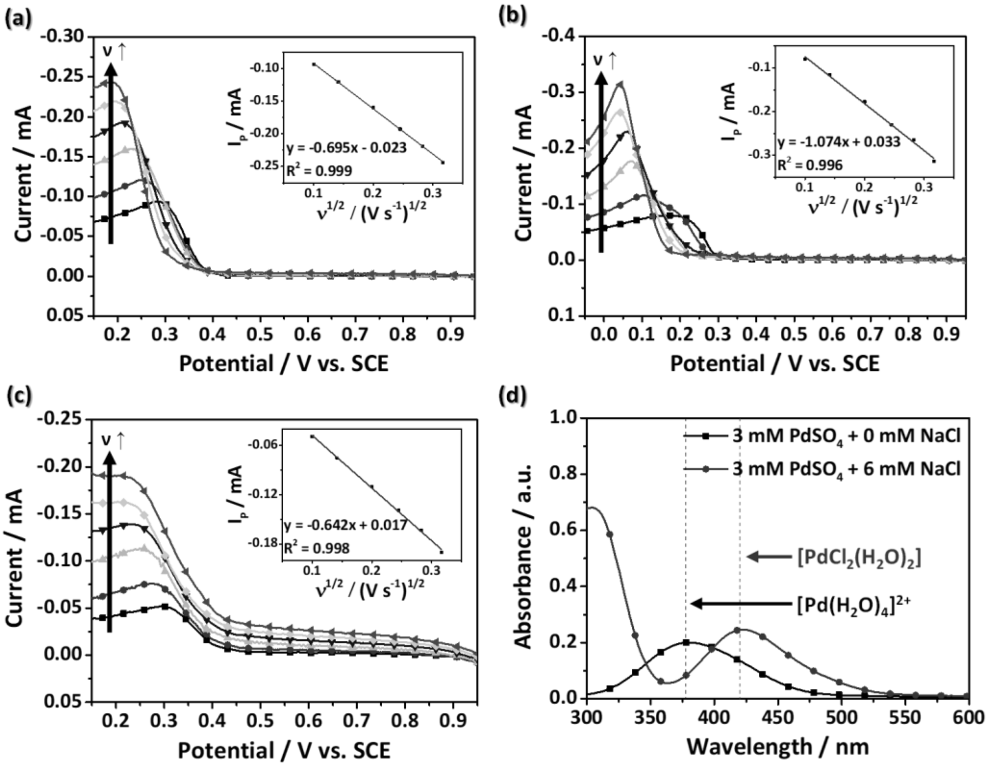

Figure 3.11. Linear sweep voltammograms of glassy carbon electrode in 0.1 M $HClO_4$ aqueous solutions with (a) 3 mM $PdCl_2$, (b) 3 mM $PdSO_4$, and (c) 3 mM $PdSO_4$ + 6 mM NaCl at the scan rates (ν) between 10 and 100 mV s^{-1}. Insets on Figure 3.11(a-c) show linear relationship between peak current (I_P) and square root of scan rate ($\nu^{1/2}$). (d) UV-Vis spectra of 3 mM $PdSO_4$ solution with 0 or 6 mM NaCl.

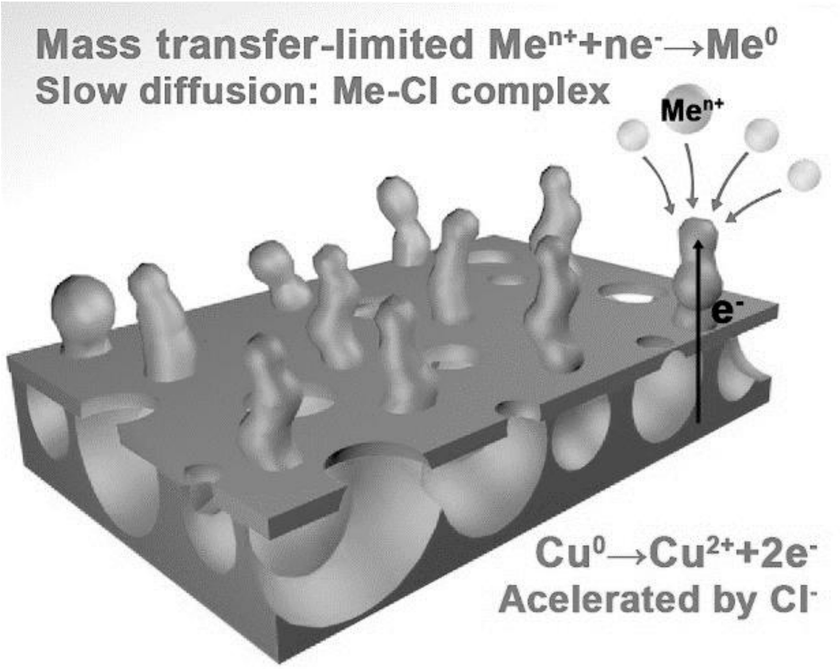

Figure 3.12. Schematic diagram for the mechanism of whisker formation during galvanic displacement.

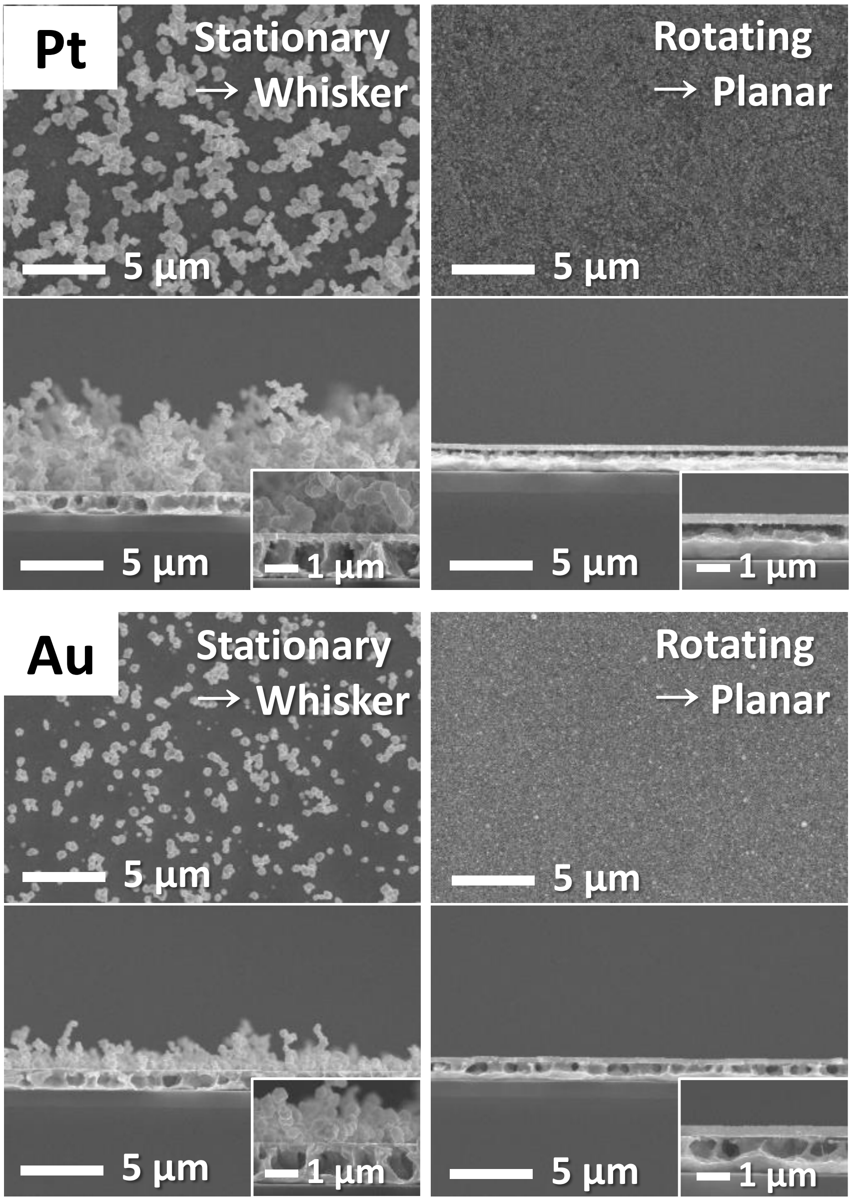

Figure 3.13. Surface and cross-sectional FE-SEM images of (a) Pt-Cu and (b) Au-Cu deposits prepared by galvanic displacement in K_2PtCl_4 and $AuCl_3$ solutions, respectively. The substrates remained stationary for 30 min or rotating at 300 rpm for 2 min during the reaction.

3.1.3. Catalytic performance toward electrochemical ethanol oxidation

The electrochemically active surface area and the electrochemical performance for ethanol oxidation of the Pd-Cu whisker were investigated. Figure 3.14(a) shows the cyclic voltammograms at several switching potentials (E_λ) for Pd disk electrode in 0.5 M KOH. The oxide reduction peak increased with increasing E_λ because more Pd was oxidized during the anodic sweep. The charges for the Pd oxide reduction calculated by integration of the peak located between -0.1 and -0.4 V are plotted against the E_λ on Figure 3.14(b). The E_λ at 0.05 V where the straight line changes its slope corresponds to the formation of a complete PdO monolayer. For the potential more anodic than 0.05 V, the formation of complex Pd oxides and oxygen evolution reaction start and can cause the incorrect calculation of a charge for the reduction of PdO monolayer [49, 76]. Therefore, the CVs were performed between -1.0 V and 0.05 V to measure precisely the reduction charge for Pd oxide monolayer. From cyclic voltammograms obtained at this E_λ (Figure 3.15), the electrochemically active surface area (S_{el}) of catalysts can be estimated from Equation (18) when Q_M is the calculated charge for reduction of PdO:

$$S_{el}\,(\mathrm{cm}^2) = Q_M(\mathrm{C}) \times 10^6/405 \qquad (18)$$

, with 405 μC cm^{-2} considered as the charge to reduce a monolayer of PdO [77]. In this way, active surface area on the Pd-Cu whisker and Pd disk electrode was evaluated by calculating the charge for Pd oxide reduction. Cyclic voltammogram of the Pd-Cu whisker on Figure 3.15 shows the accumulated reduction peak of Cu oxide and Pd oxide in the potential region for the integration. Therefore, the charge of Pd oxide reduction on Pd-Cu whisker electrode was calculated solely after subtraction of Cu oxide reduction peak by peak deconvolution. The roughness factors (S_{el}/S_{geom}) of the Pd disk and Pd-Cu whisker electrodes were 1.23 and 21.1, respectively, indicating that the whisker catalyst exhibited a 17-fold greater surface area for the electrochemical reaction than the planar catalyst. Figure 3.16(a) shows the cyclic voltammograms of the Pd-Cu whisker and Pd disk electrodes for ethanol oxidation reaction which has been used for direct ethanol fuel cells (DEFCs) [32, 33]. Two oxidation peaks appeared in forward and backward scans. In the forward scan, the oxidation peak located at -0.3 V for Pd and at -0.1 V for Pd-Cu whisker is assigned to the oxidation of freshly chemisorbed ethanol. The positive shift of ethanol oxidation peak was attributed to the alloy nature of Pd-Cu whisker [33]. Whereas, the oxidation peak in the reverse scan located at -0.4 V is associated with the removal of carbonaceous species not oxidized in the forward scan [33]. The anodic peak current density for ethanol oxidation, observed in the forward scan, on Pd-Cu whisker (146.5 mA cm^{-2}) was 21-fold higher compared to that on Pd disk (7.0 mA cm^{-2}). Even after normalization with their roughness factors, the peak current density on Pd-Cu whisker (7.2 mA cm^{-2}) was higher than that on Pd disk (5.1 mA cm^{-2}). The onset potential for the ethanol oxidation on the Pd-Cu whisker was -0.66 V, which was more negative than the potential of -0.54 V on Pd disk, representing lower activation energy on Pd-Cu whisker. Regardless of the large surface area of Pd-Cu whisker, Pd-Cu whisker electrode showed higher roughness factor-normalized peak current density and more negative onset potential for ethanol oxidation, implying the improvement in the intrinsic catalytic activity over Pd disk electrode due to alloying effect of Pd and Cu [31-33]. In addition, the ratio of the forward anodic peak current (I_f) to the backward anodic peak current (I_b), usually reflecting the tolerance to carbonaceous species accumulation on catalysts, on Pd-Cu whisker (1.6) was higher than that on Pd disk (0.5). Therefore, both the large surface area of whiskers and the modified electronic structure by alloying Pd and Cu resulted in the enhanced electrocatalytic activity. The stabilities of disk and whiskered electrodes were finally investigated by chronoamperometry at the potential of -0.245 V at which ethanol oxidation reaction occurred for 3600 s (Figure 3.16(b)), and it was obvious that Pd-Cu whisker has better electrocatalytic performance towards ethanol oxidation than Pd disk even in long-term.

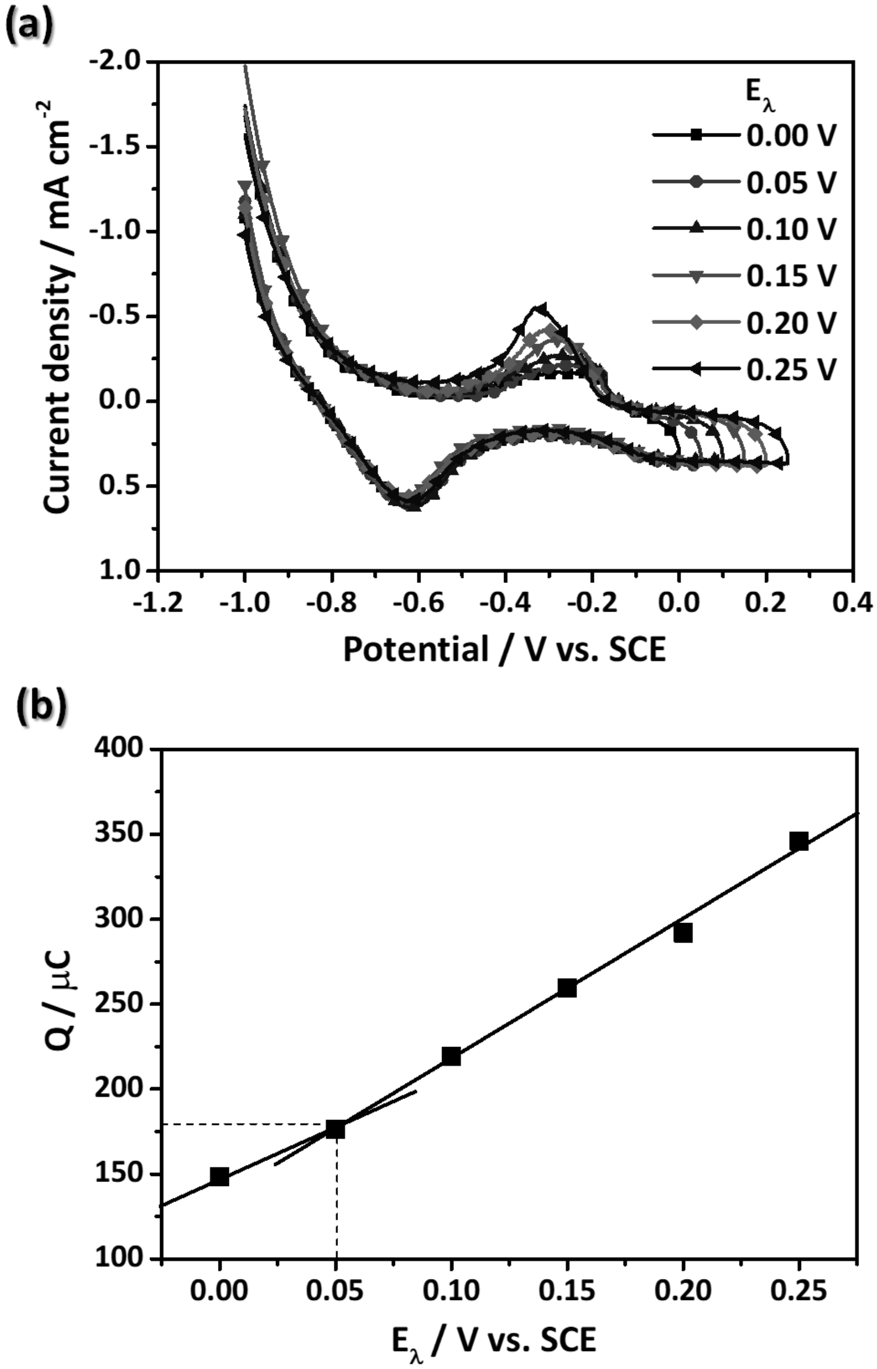

Figure 3.14. (a) Cyclic voltammograms with varying the switching potential (E$_\lambda$) for Pd disk electrode in 0.5 M KOH aqueous solution. The scan rate was 50 mV s^{-1}. (b) The calculated charge for Pd oxide reduction from Figure 3.14(a) as a function of E$_\lambda$.

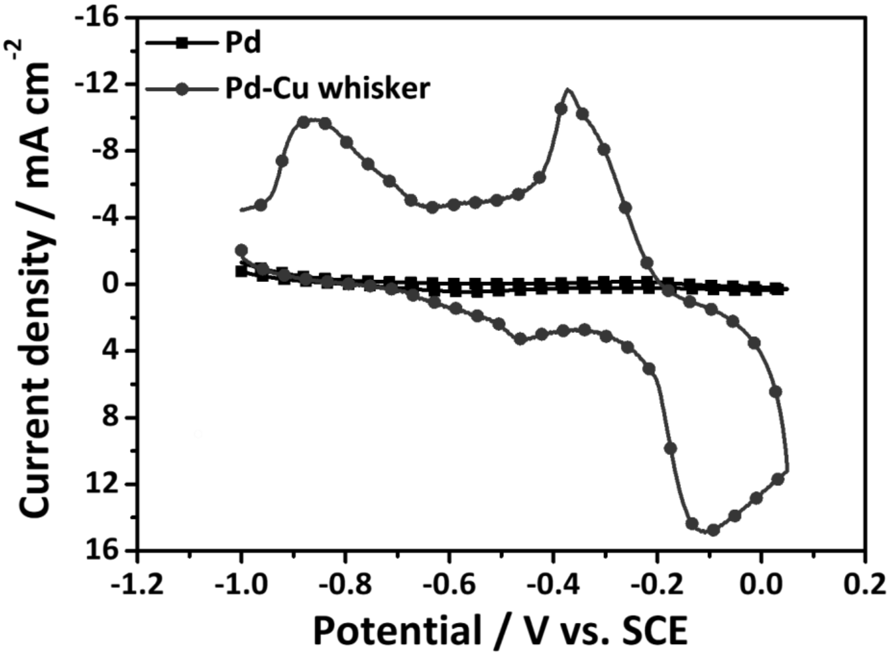

Figure 3.15. Cyclic voltammograms of Pd-Cu whisker and Pd disk electrodes with 0.05 V of E_λ in 0.5 M KOH solution with a scan rate of 50 mV s^{-1}.

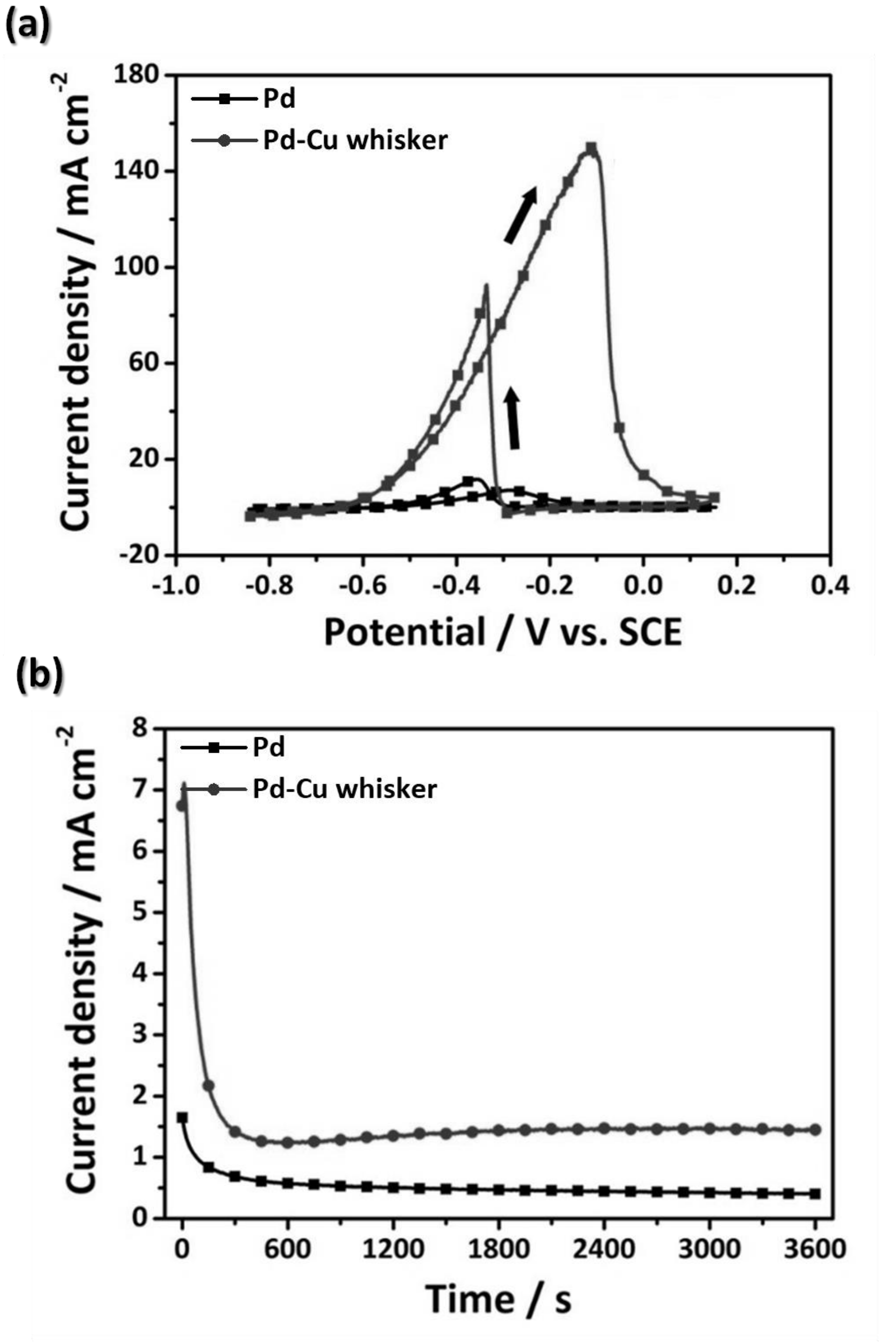

Figure 3.16. (a) Cyclic voltammograms of Pd-Cu whisker and Pd disk electrodes in 1 M KOH and 1 M ethanol solution with a scan rate of 20 mV s^{-1}. (b) i-t curves of Pd-Cu whisker and Pd disk electrodes in 1 M KOH and 1 M ethanol solution at -0.245 V for 3600 s.

3.1.4. Application of Pd-Cu whisker catalyst in Couette-Taylor flow mixer/electrolysis reactor hybrid system

The performance of electrochemical reaction of gaseous reactants strongly depends on solubility and mass transfer of gaseous substances as well as catalytic activity. Therefore, a CTF mixer can enhance the N_2O reduction performance by increasing the solubility and mass transfer rate of N_2O in the electrolyte solution.

The concentration of N_2O in the solution dissolved using a CTF mixer with different operating condition was measured by the electrochemical method based on the fact that the current for an electrochemical reaction is proportional to the concentration of reactants [11]. CV was performed using Pd RDE by varying the pH of K_2SO_4. As shown in Figure 3.17(a), the reduction peak of N_2O was clearly observed at -0.5 V regardless of pH, which is in accordance with a prior publication [78]. The peak current density for N_2O reduction was higher in the higher pH solution, thus, the measurement of N_2O concentration by peak current density of N_2O reduction was performed in the pH 12 solution to improve the accuracy of electrochemical measurement. The voltammogram obtained with N_2-purged electrolyte solution shows the onset potential for hydrogen evolution of -0.7 V which is more negative than the potential for N_2O reduction. The appearance of a small reduction peak at -0.4 V in the absence of N_2O was for the reduction of Pd oxide formed during an anodic sweep between 0 and 1.0 V [3, 6]. The current for Pd oxide reduction was independent of N_2O concentration in the electrolyte solution, not interfering the electrochemical measurement of N_2O concentration. The current related to the electrolytes was not observed both in the absence and the presence of N_2O in Figure 3.17(a). These results suggest that it is possible to estimate the N_2O concentration by measuring peak current density for N_2O reduction on the cyclic voltammogram.

To find out the optimum concentration of K_2SO_4 which was added as a supporting electrolyte to reduce electrolyte resistance, a peak current density was measured by varying K_2SO_4 concentration. It has been reported that the addition of salt could reduce the gas solubility due to a salting-out effect [79]. At the same time, however, the electrochemical reaction could not be performed effectively without adding salts because of high electrolyte resistance. Thus, figuring out the optimum salt concentration is important for electrochemical reaction. Figure 3.17(b) shows that N_2O reduction current increased significantly in the N_2O-saturated solution when K_2SO_4 was added to reduce solution resistance. The peak current for N_2O reduction was not observed at 0 mM K_2SO_4. However, it appeared by K_2SO_4 addition and the peak current density increased gradually as the concentration of K_2SO_4 was increased up to 300 mM. Then, the peak current density turned to decrease over 300 mM K_2SO_4 due to the conflicting effects of K_2SO_4 between an increase in solution conductance and a decrease in N_2O solubility by salting-out effect. From the results, it can be concluded that the 300 mM is the optimum concentration of K_2SO_4 for an efficient electrochemical reduction of N_2O under the experimental condition we investigated.

Figure 3.18(a) shows the cyclic voltammograms, recorded by varying the N_2O concentration in the electrolyte solution. Electrolytes with different N_2O concentration were prepared by diluting N_2O-saturated electrolyte: First, deaerated and N_2O-saturated electrolytes were prepared by N_2 and N_2O purging for 30 min in an open vessel. The pressure and temperature were maintained at 101 kPa (abs) and at 298 K, where the saturated concentration of N_2O is 24.3 mM [3, 80]. Then, the N_2O-saturated electrolyte was diluted by mixing in the different ratios with N_2-purged electrolyte. The peak current density for N_2O reduction around -0.5 V increased as the concentration of N_2O arose. Figure 3.18(b) shows the relationship between the peak current density observed on Figure 3.18(a) and the N_2O concentration in an electrolyte solution. It represents a strong linearity for the concentration region from 0 to 24.3 mM with R^2=0.9977. Thus an unknown N_2O concentration can be estimated by measuring the peak current density using this calibration curve. In this way, the concentration of N_2O dissolved by a CTF mixer was measured by conducting the CV analysis in the N_2O-dissolved solution.

The effectiveness of Taylor vortex in dissolving N_2O was investigated by controlling the Ta number. As defined in Equation (10), the Ta number was controlled by varying the rotation speed of the inner cylinder. When the rotation speed of the inner cylinder increases above 13 rpm, the Ta number exceeds a critical number of 41.19 and Taylor vortices evolve in the electrolyte [81]. The concentration of saturated N_2O in the electrolyte with or without Taylor vortices was electrochemically measured (Figure 3.19). The highest N_2O saturation concentration of 31.1 mM was obtained at the Ta number of

3229. On the other hand, when N_2O was dissolved without rotating the inner cylinder, the saturation concentration was 24.1 mM, and it was very similar value to the reported N_2O solubility, 24.3 mM, at 101 kPa (abs) and at 298 K [3]. It indicates that Taylor vortices notably increased the N_2O solubility as 29.0%. Figure 3.19 illustrates that the saturation time decreases, and the saturated concentration of N_2O increases as the Ta number increases up to 3229. The saturation time just took 2 min to saturate the electrolyte with N_2O at Ta=3229 (1000 rpm) while 20 min was required for saturating electrolyte at Ta=10 (3 rpm) as shown in Figure 3.19(a). It is known that the CTF mixer increases the gas-liquid interfacial area by forming small bubbles and the mass-transfer coefficient by dissipating energy from the rotating inner cylinder [58, 59, 82, 83]. Thus, the enhanced N_2O dissolution could result from the enhancement of mass transfer originating from the increased interfacial area and the mass transfer coefficient. The saturation time became longer and the saturated N_2O concentration turned to decrease slightly when Ta exceeded 3229. From the result, it can be concluded that the optimum Ta number for efficient dissolution was 3229 with the CTF mixer. It is thought that the flow transition to the unsteady and wavy vortex at greater Ta number might be a reason for the decrease in N_2O dissolution performance [16, 84].

The maximum N_2O saturation concentration of 31.1 mM was obtained at Ta number of 3229 as shown in Figure 3.19(b). The concentration increased until Ta number became 3229, then it slightly dropped. The increase in the saturated N_2O concentration with increasing rotation speed was probably due to the decreased bubble size [58]. In the CTF mixer, small bubbles with higher gas pressure are formed as a result of sucking action of Taylor vortices. The bubble size decreased with increasing rotation speed of inner cylinder due to the more intensive mixing by Taylor vortices. Therefore, the saturated concentration increased with increasing rotational speed up to 1000 rpm.

In addition to the Ta number, the liquid (electrolyte) and gas flow rates could affect N_2O dissolution because they could affect a flow pattern and a residence time of gas-liquid two-phase flow in the CTF mixer. Thus, the changes in the saturated concentration of N_2O with the liquid and gas flow rates were investigated. Figure 3.20(a) shows the saturated N_2O concentration measured at the fixed gas flow rate of 0.15 L min^{-1}. There was no clear dependence of the saturated N_2O concentration on the liquid flow rate. Similar N_2O saturation concentration with small deviation was obtained for each liquid flow rate. It can be assumed that liquid flow rate is not the main factor affecting N_2O dissolution. On the other hand, the saturated N_2O concentration increased with gas flow rate as shown in Figure 3.20(b). It corresponds to the paper by S. Wronski et al. suggesting that bubble size, which determines the inner pressure of N_2O and its solubility, decreased with increasing volumetric flow ratio of gas and liquid, while the liquid flow rate is less important [58]. In the experimental scope of this study, the liquid flow rate of 0.2 L min^{-1} and the gas flow rate of 0.15 L min^{-1} are the optimum values when the Ta number was 3229.

The usefulness of a CTF mixer as an N_2O-dissolving method for electrochemical N_2O reduction was assessed by comparing the saturation time and the saturated concentration of N_2O dissolved by the CTF mixer with those by the batch system (Figure 3.21). N_2O dissolution in the batch system was accomplished by bubbling N_2O in a beaker with or without stirring by an overhead stirrer rotating at 300 rpm. N_2O was supplied with the flow rate of 0.15 L min^{-1} at 298 K for both systems. During the N_2O purging in the CTF mixer, the inner cylinder remained rotating at 1000 rpm, and the electrolyte was circulated at 0.2 L min^{-1}. Two main differences between CTF mixer and batch system were observed on Figure 3.31. First, the CTF mixer is more efficient than the batch system for fast supply of N_2O. The solution was saturated within 2 min by a CTF mixer, while it took 30 min for saturation in a batch system. It is because gas-liquid interface area and mass transfer coefficient in the CTF mixer are larger than those in the batch system [85]. Second, more N_2O was dissolved with a CTF mixer than with a batch system. The CTF mixer (31.1±0.4 mM) dissolved 26.9% more N_2O than the batch system (24.5±0.6 mM) did. It can be predicted that N_2O is more soluble using the CTF mixer because the gas pressure of N_2O is higher due to the small bubble formation and the strong impact between N_2O and electrolyte where Taylor vortices occur. Therefore, it can be concluded that the dissolution of N_2O was accelerated by the improved mass transfer between N_2O and electrolyte and the solubility of N_2O was increased by greater bubble pressure induced by small bubble size comparing with a conventional bubbling. Therefore, the CTF mixer is advantageous over the batch system, in that the enormous amount of N_2O can be electrochemically reduced when the electrochemical system is connected to the CTF mixer. Electrochemical N_2O reduction was performed in the electrochemical reactor-combined CTF mixer where outer and inner cylinders worked as negative and positive electrodes, respectively. Pd-Cu whisker catalyst obtained by galvanic displacement deposition on Cu foil in $PdCl_2$ solution was attached to outer cylinder as a N_2O-reducing catalyst. While N_2O reduction potential of 3.5 V was or was not applied to the electrochemical-CTF mixer system, gases existed from the system were analyzed with GC (Figure 3.22). The N_2O peak on the chromatogram indicated the exited N_2O gas which was not dissolved and not reacted in the system. The N_2 and H_2 peaks were originated from the electrochemical reduction reactions of N_2O and H_2O on negative electrode, respectively. The O_2 was product gas of electrochemical H_2O oxidation reaction on positive electrode, which occurred simultaneously with the reduction reactions on negative electrode. N_2O peak disappeared on the chromatogram when the potential of 3.5 V for N_2O reduction was applied to the system with rotating inner cylinder, as shown in Figure 3.22(a). However, the peak intensity of N_2O was not reduced when N_2O reduction was performed where inner cylinder remained stationary as shown in Figure 3.22(b). N_2O conversions were calculated by measuring peak area of N_2O from the chromatograms before and after N_2O reduction. N_2O conversions of 99.99% and 5.39% were obtained at the inner cylinder rotation conditions of 1000 rpm and 0 rpm, respectively (Table 3.1). The increased N_2O conversion by rotating inner cylinder indicates that fast N_2O supply to the N_2O-reducing catalyst and high N_2O concentration in the solution induced by Taylor vortex enhanced N_2O reduction performance of electrochemical-CTF mixer system. Therefore, effective N_2O electrolysis is possible by using CTF mixer system-combined electrolysis reactor.

Table 3.1. N_2O conversions at different rotational speed of inner cylinder of a CTF mixer

Rotational speed	1000 rpm	0 rpm
N_2O conversion	99.99%	5.39%

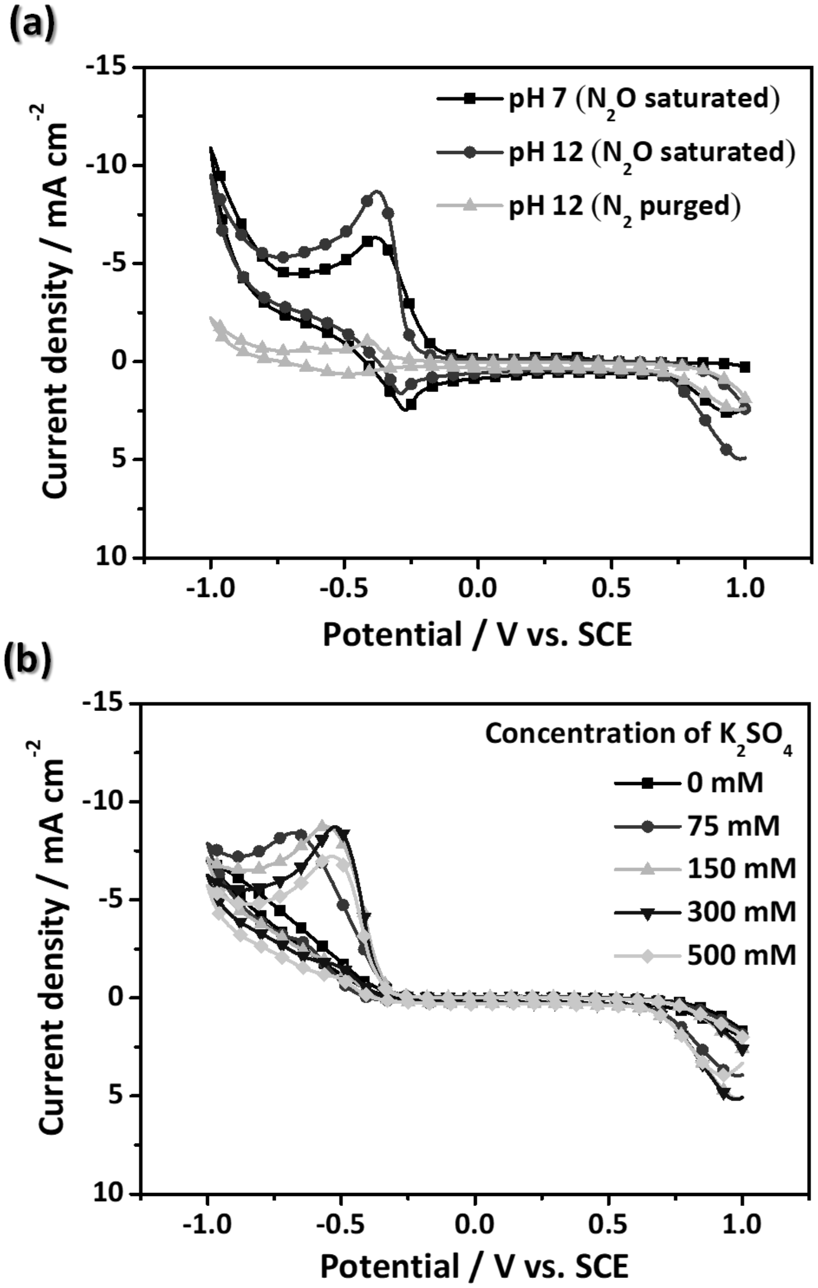

Figure 3.17. (a) CV curves obtained in the electrolyte solution at pH 7 or pH 12 with N_2 purging or N_2O saturation, and (b) CV curves obtained by varying K_2SO_4 concentration from 0 to 500 mM at pH 12.

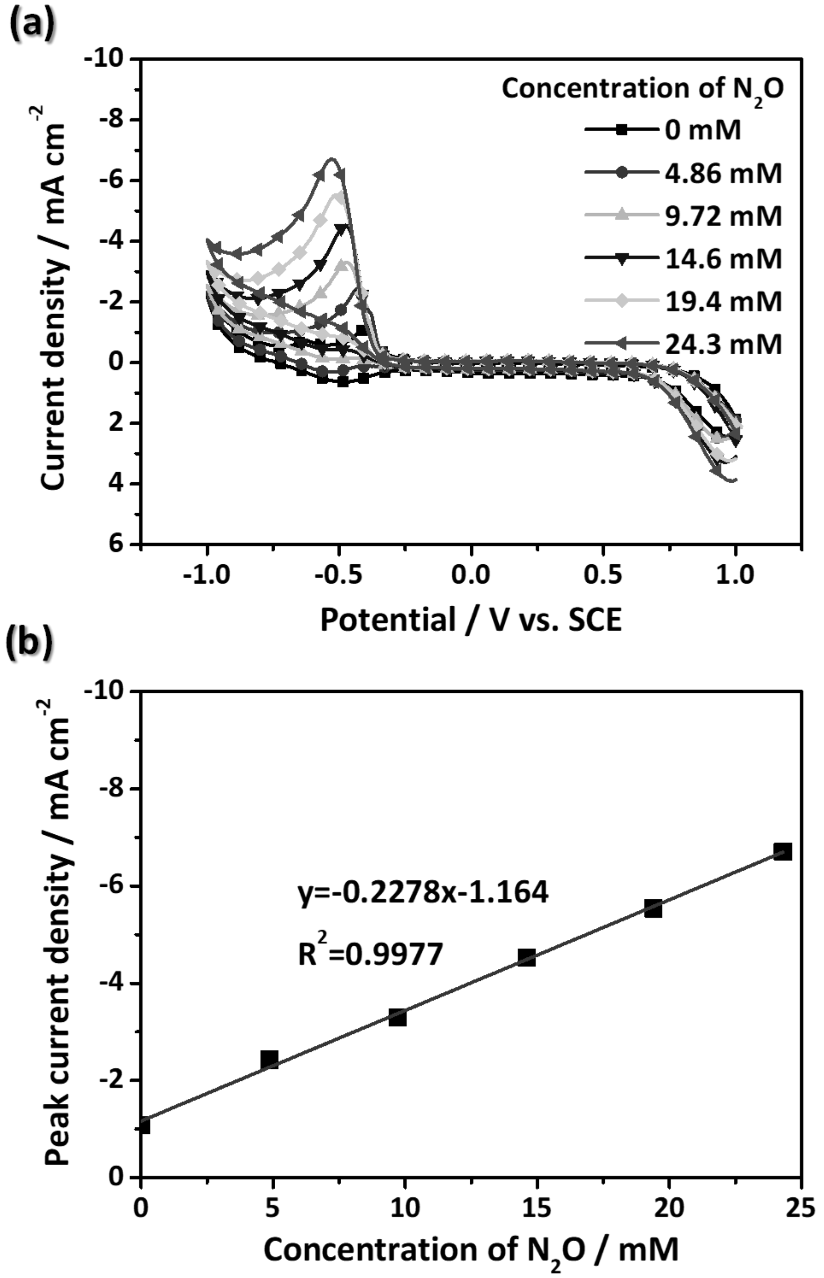

Figure 3.18. (a) CV curves obtained by varying the concentration of N_2O dissolved in the electrolyte solution, and (b) empirical fitting curve showing the linear correlation between peak current density for N_2O reduction and dissolved N_2O concentration.

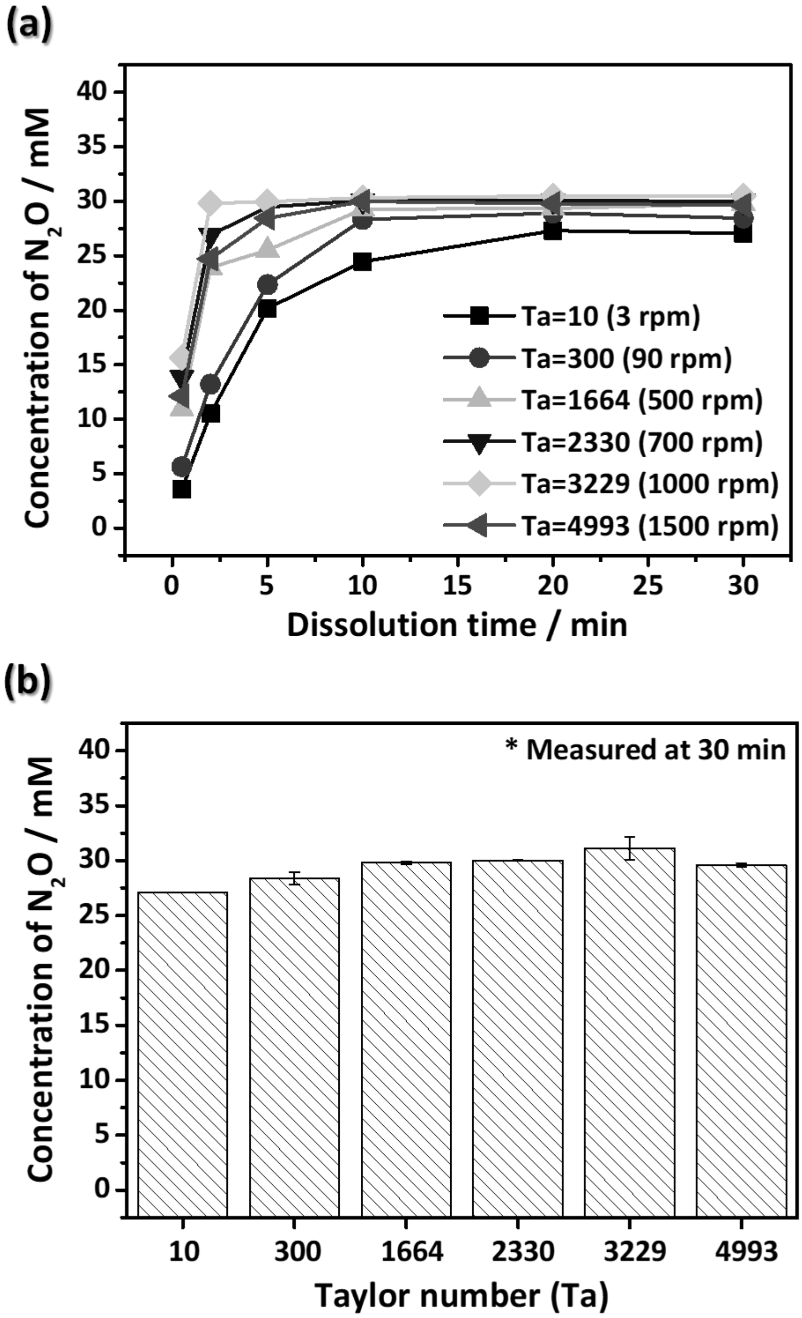

Figure 3.19. (a) Change in the N_2O concentration with N_2O dissolution time at various Ta number controlled by rotation speed of inner cylinder in the CTF mixer, and (b) saturated N_2O concentration, measured at N_2O dissolution time of 30 min, as a function of Ta number.

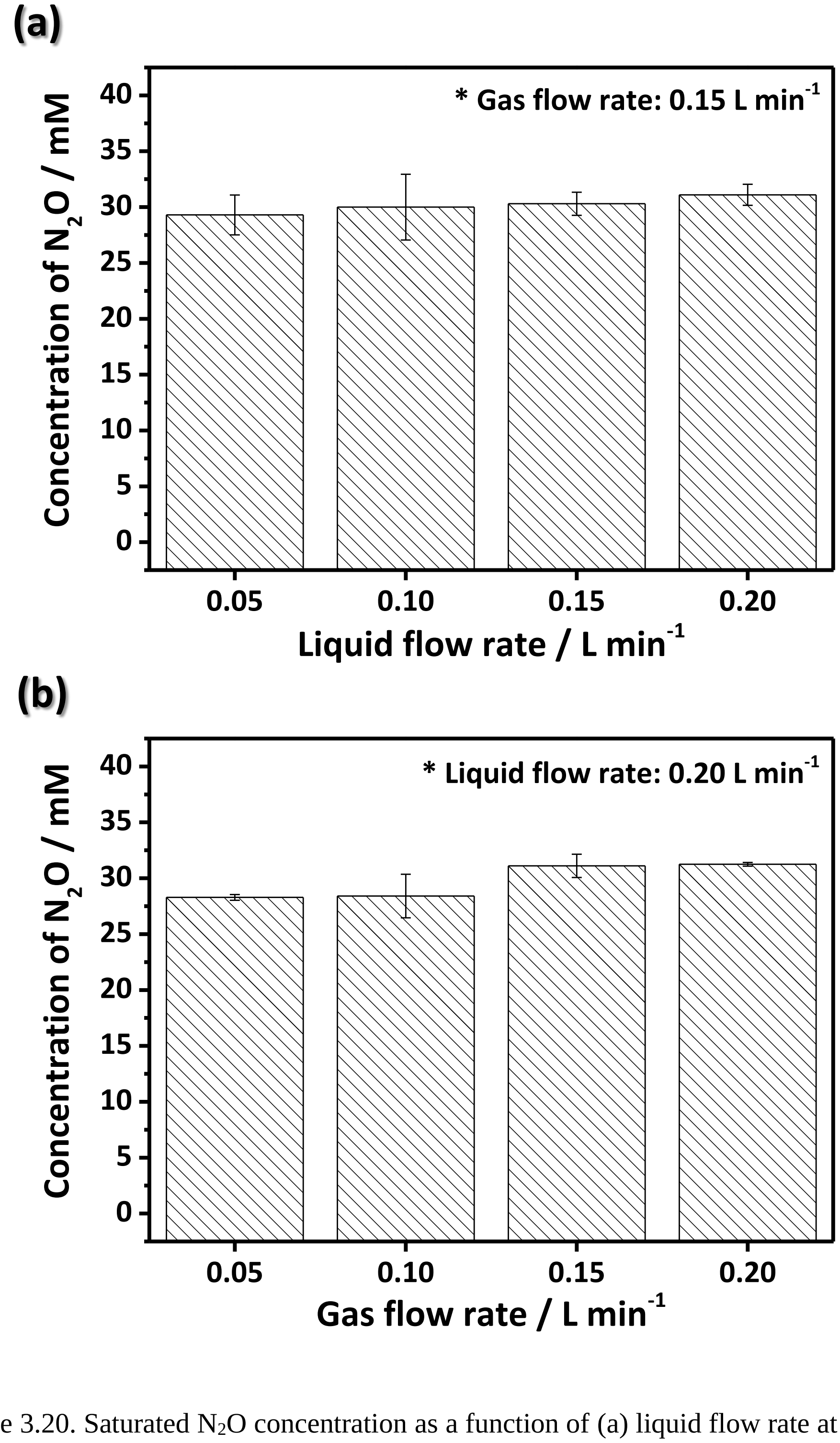

Figure 3.20. Saturated N_2O concentration as a function of (a) liquid flow rate at the gas flow rate of 0.15 L min^{-1} and (b) gas flow rate at the liquid flow rate of 0.20 L min^{-1}.

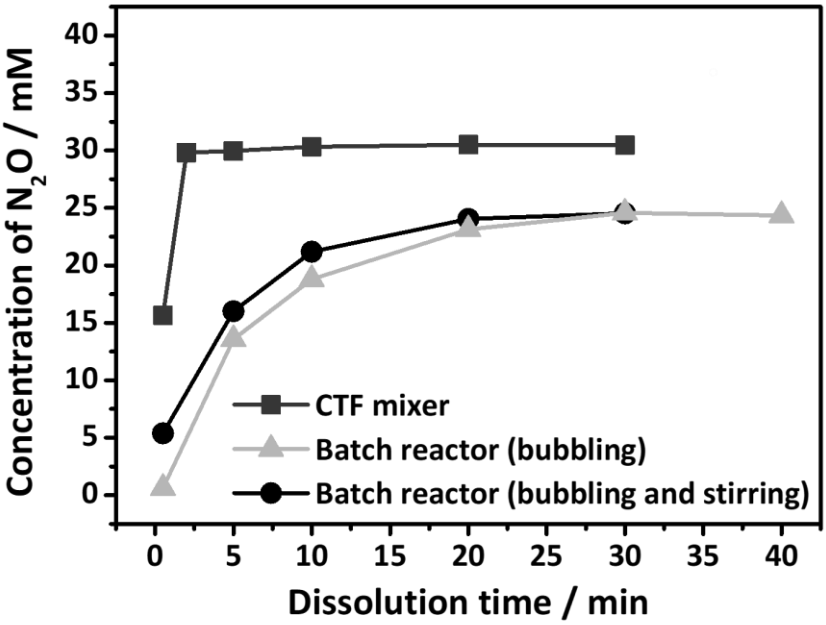

Figure 3.21. Change in the N_2O concentration with N_2O dissolution time at various pre-mixing methods: CTF mixer, bubbling in batch system, and bubbling and stirring in batch system.

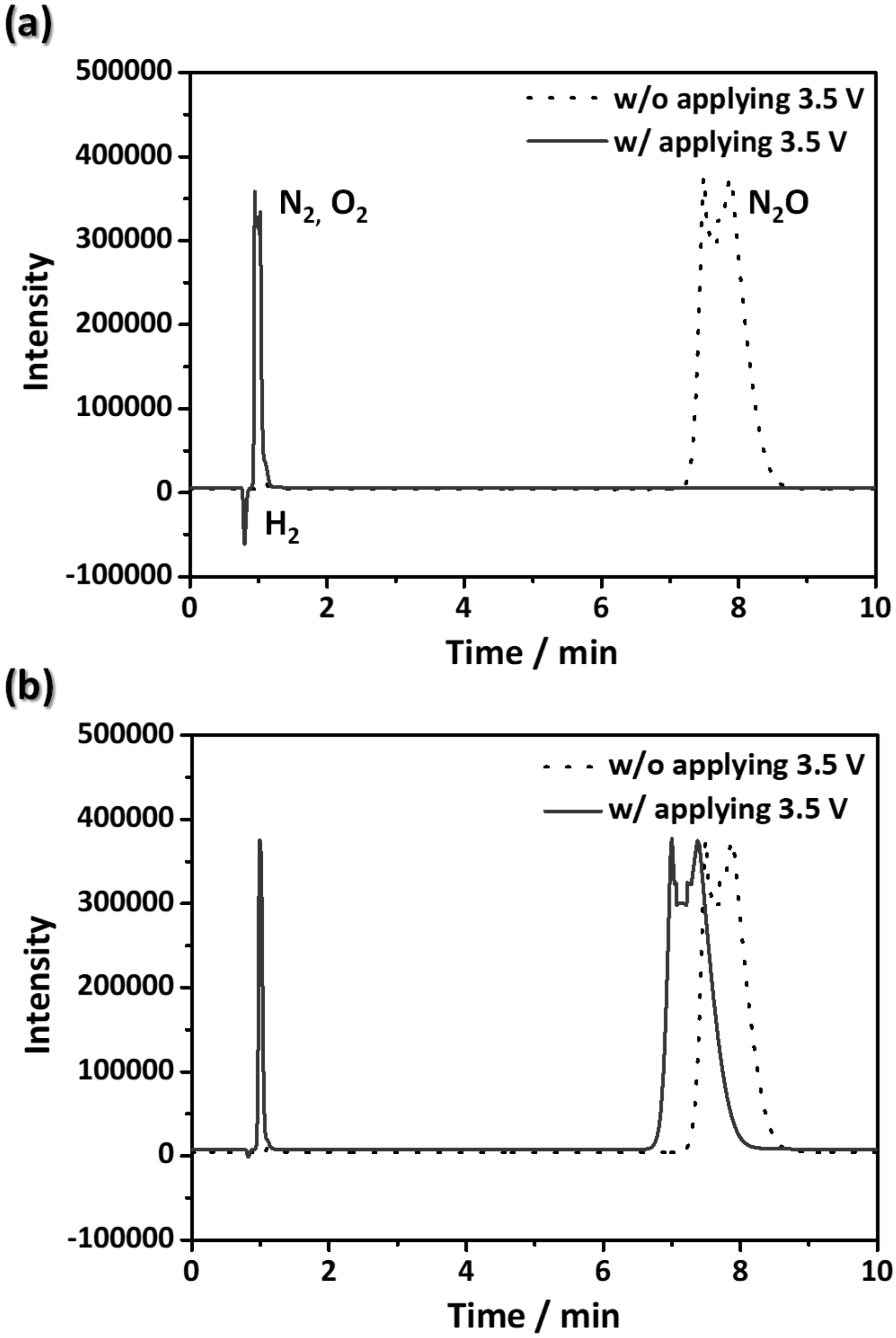

Figure 3.22. GC chromatograms of gases exited from the electrochemical-CTF mixer system when the N_2O reduction potential of 3.5 V was or was not applied to the system (a) with (1000 rpm) or (b) without (0 rpm) inner cylinder rotation, respectively.

3.2. Composition-controlled synthesis of Pd-Cu catalyst via galvanic displacement deposition

3.2.1. Citric acid-assisted synthesis of Pd-Cu catalyst with controllable surface composition

The addition of additives to the galvanic displacement bath which chemically interact with Pd and Cu can affect the Pd-Cu galvanic displacement reaction, leading to a change in the morphology and the chemical composition of deposit. The morphology of Pd-Cu deposit obtained by varying concentration of citric acid in galvanic displacement bath was firstly investigated. The morphological characteristics of the Pd-Cu deposit were examined using FE-SEM (Figure 3.23) and AFM (Figure 3.24). Figure 3.23 shows that deposits have smooth surface similar with pristine Cu foil. The root-mean-square (RMS) roughness of deposits was represented on Figure 3.25. The surface of deposit obtained by galvanic displacement reaction became smoother as the concentration of citric acid increased. It has been reported that metal deposition takes place in horizontal direction than in perpendicular direction when complexes are formed between deposited metal and complexing agents and they are not dissociated after the deposition [86]. Therefore, as increasing citric acid concentration, the citric acid-adsorbed surface might increase, contributing to the deposit formed by galvanic displacement with smoother surface morphology. The energy-dispersive spectroscopy (EDS) elemental maps as shown in

Figure 3.26 suggests the uniform distribution of Cu and Pd in the deposit.

X-ray photoelectron spectroscopy (XPS) analysis was conducted to elucidate the chemical composition of Pd-Cu catalysts prepared by galvanic displacement in $PdSO_4$ solution (Figure 3.27). The atomic ratios of Pd to Cu on Pd-Cu catalysts measured by XPS are represented in Figure 3.28(a). The results indicate that the concentration of Pd in Pd-Cu catalysts increased while Cu concentration decreased as increasing the citric acid concentration. The surface composition of Pd-Cu catalysts was measured by angle-resolved XPS and AES analysis (Table 3.2). The Pd:Cu atomic ratio on the surface was almost the same as the composition measured by normal XPS with a deviation less than 1.24%. Therefore, each catalysts were named as $Pd_{49}Cu_{51}$, $Pd_{61}Cu_{39}$, $Pd_{66}Cu_{34}$, $Pd_{74}Cu_{26}$, and $Pd_{84}Cu_{16}$ representing their Pd/Cu atomic ratios based on the results from quantitative XPS analysis on Figure 3.28(a). Figure 3.28(b) shows X-ray diffraction (XRD) patterns of the catalysts prepared with different concentration of citric acid. The sharp peaks at 43, 51, 74, and 90^o on the XRD patterns indicate (111), (200), (220), and (311) of (fcc) Cu crystal (JCPDS 04-0836), respectively, which were from underlying Cu foil substrate. The appearance of a peak at 41^o is related (111) reflection of face centered cubic (fcc) PdCu crystal (JCPDS 48-1551), which implies that bimetallic Pd-Cu alloy structures are formed. The PdCu peak was clearly shifted to lower two-theta value as increasing concentration of citric acid added in the reaction bath. The gradual shift in the PdCu peak position reflects the increase in the lattice distance caused by decreased content of Cu which has smaller atomic size than Pd. This corresponds to the quantitative analysis performed with XPS. In addition, the full width at half maximum (FWHM) of these PdCu (111) peaks increased with increasing the citric acid concentration as shown in Figure 3.28(c), which could result from the larger number of defects and the smaller grain size [32, 87, 88]. It suggests that citric acid could be incorporated into Pd-Cu deposit during galvanic displacement and affect the crystallinity of the deposit. It was confirmed by EDS chemical composition analysis for carbon content as an indicator of the incorporated citric acid (Figure 3.28(d)). As increasing citric acid concentration added in the $PdSO_4$ solution, the amount of citric acid incorporated in Pd-Cu catalysts increased. Angle-resolved XPS analysis was also conducted to confirm the citric acid incorporation. As depicted in Figure 3.29, the C 1s XPS spectra exhibited three peaks at 284.5 eV, 285.4 eV, and 287.9 eV, which are ascribed C-C, C-O, and C=O, respectively [89]. The carbon content and C=O content in Pd-Cu catalysts prepared in $PdSO_4$ solution with 0 and 1 mM citric acid are summarized in Table 3.3. When adding citric acid in Pd displacement bath, carbon and C=O contents in the Pd-Cu catalyst increased, revealing the citric acid incorporation. It has been reported that citric acid can strongly adsorb on Cu and Pd surfaces [90, 91]. Therefore, it is expected that the adsorption and incorporation of citric acid could retard inter-diffusion of Cu from Cu foil into the deposit, resulting in the increase in Pd content in Pd-Cu catalysts. In this regard, citric acid played a role of composition controller for Pd-Cu catalyst in galvanic displacement.

Table 3.2. The atomic ratio of Pd:Cu on Pd-Cu catalysts prepared with 0 or 1 mM of citric acid in $PdSO_4$ solution

	Pd-Cu catalyst obtained with 0 mM citric acid	Pd-Cu catalyst obtained with 1 mM citric acid
Pd:Cu atomic ratio on the surface of catalyst	49.1:50.9(a)	66.7:33.3(b)
Pd:Cu atomic ratio measured by XPS	48.5:51.5	66.2:33.8

The surface Pd:Cu atomic ratios were measured by AES-depth profile(a) and angle-resolved XPS(b).

Table 3.3. Carbon content and C=O content in Pd-Cu catalyst prepared in $PdSO_4$ solution with (a) 0 mM and (b) 1 mM citric acid, measured at 0, 10, 20, and 30 degree of XPS take-off angle

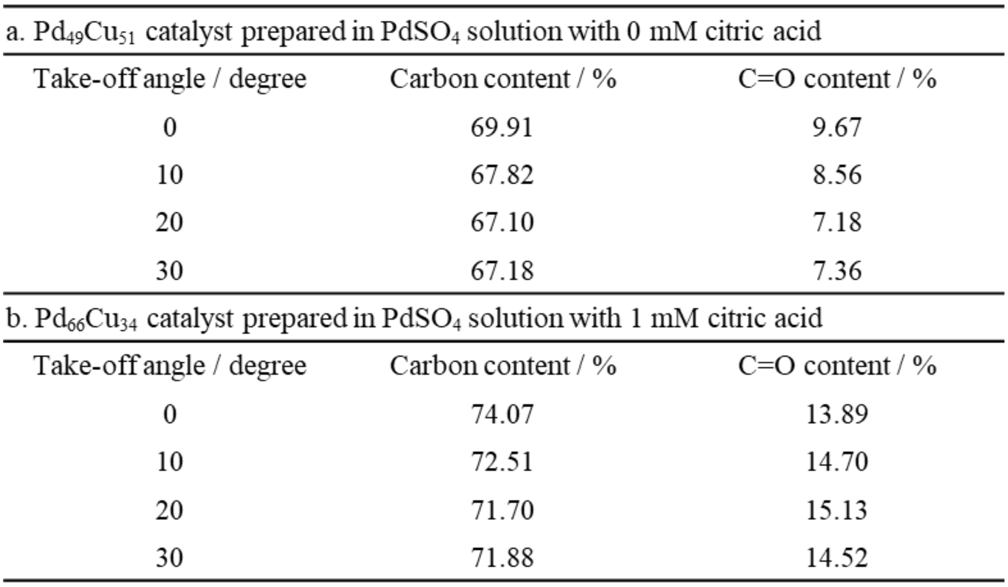

a. $Pd_{49}Cu_{51}$ catalyst prepared in $PdSO_4$ solution with 0 mM citric acid

Take-off angle / degree	Carbon content / %	C=O content / %
0	69.91	9.67
10	67.82	8.56
20	67.10	7.18
30	67.18	7.36

b. $Pd_{66}Cu_{34}$ catalyst prepared in $PdSO_4$ solution with 1 mM citric acid

Take-off angle / degree	Carbon content / %	C=O content / %
0	74.07	13.89
10	72.51	14.70
20	71.70	15.13
30	71.88	14.52

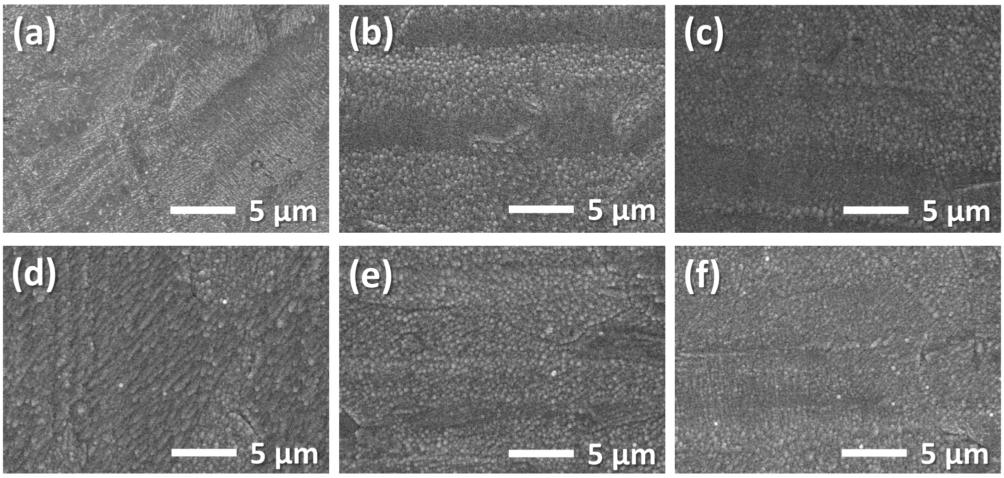

Figure 3.23. FE-SEM images of (a) bare Cu foil substrate and Pd-Cu deposits formed on the Cu foil by galvanic displacement in $PdSO_4$ solution with citric acid concentration of (b) 0 mM, (c) 0.1 mM, (d) 1 mM, (e) 10 mM, and (f) 100 mM.

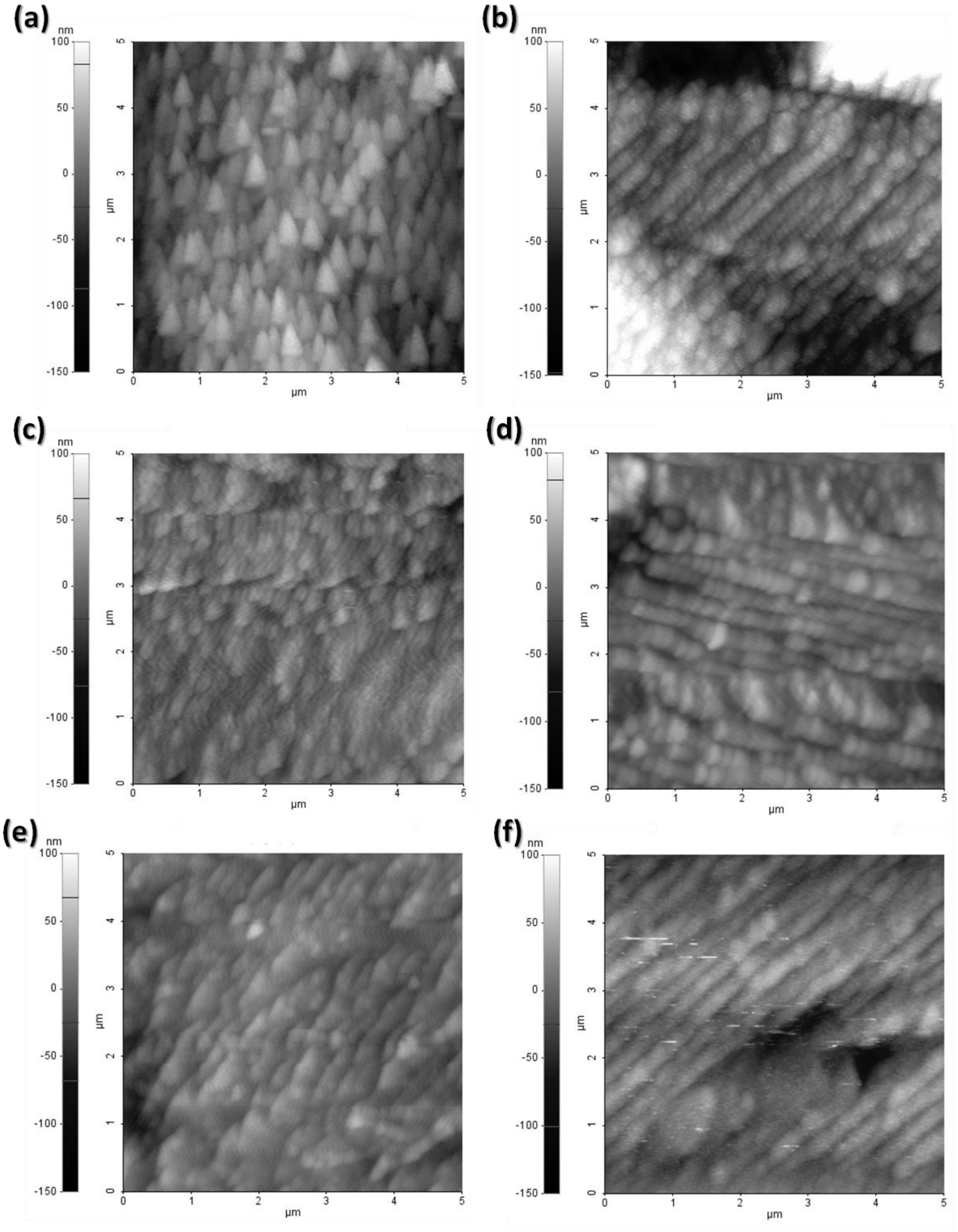

Figure 3.24. AFM images of Cu foil (a) before and after galvanic displacement with (b) 0 mM, (c) 0.1 mM, (d) 1 mM, (e) 10 mM, and (f) 100 mM of citric acid.

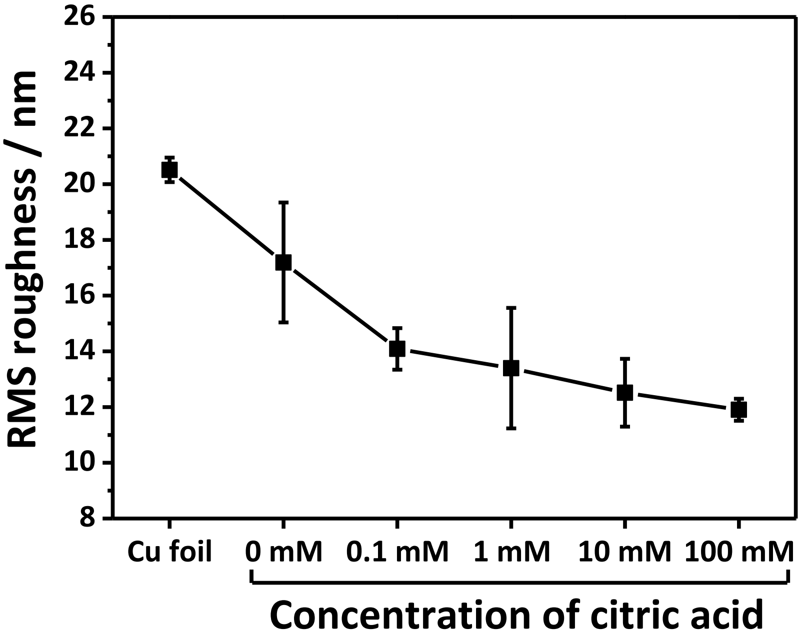

Figure 3.25. RMS roughness measured on Figure 3.24 of Pd-Cu deposits as a function of the citric acid concentration.

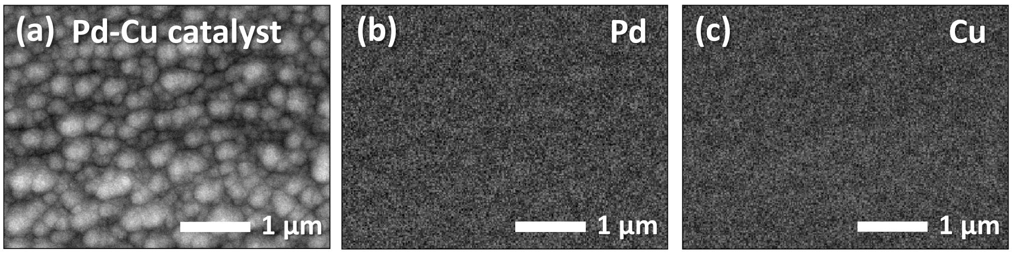

Figure 3.26. (a) FE-SEM image of Pd-Cu catalyst prepared in $PdSO_4$ solution with 1 mM citric acid and EDS mapping results for (b) Pd and (c) Cu elements.

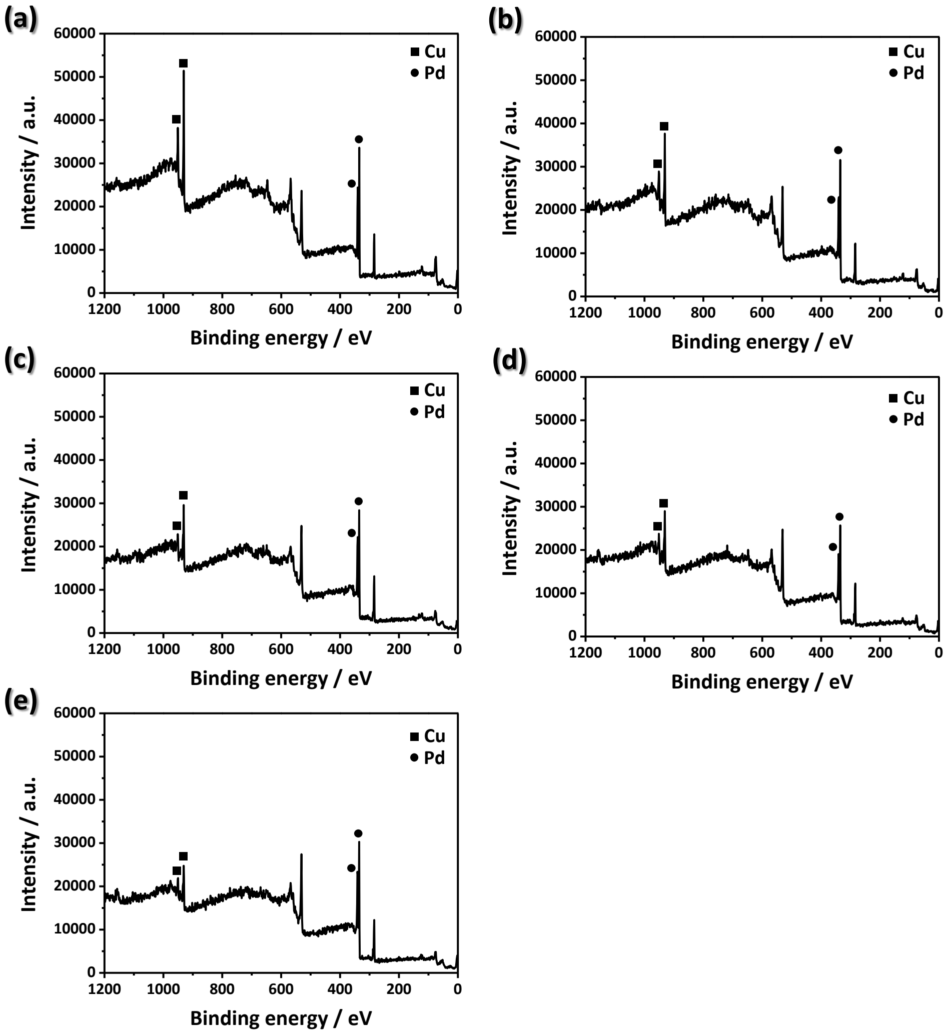

Figure 3.27. XPS spectra of Pd-Cu catalysts prepared with (a) 0 mM, (b) 0.1 mM, (c) 1 mM, (d) 10 mM, and (e) 100 mM of citric acid in $PdSO_4$ solution.

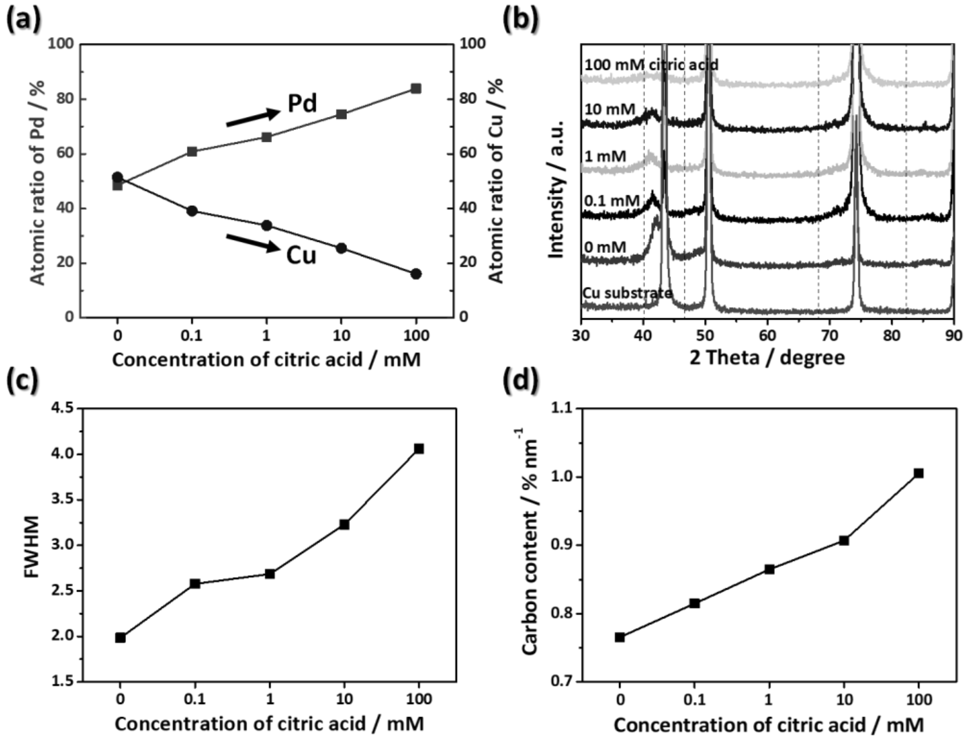

Figure 3.28. (a) Quantitative analysis of Pd and Cu elements by XPS, (b) XRD patterns, (c) FWHM of PdCu (111) peak on the XRD patterns, and (d) carbon content measured by EDS on Pd-Cu catalysts prepared with different concentrations of citric acid in $PdSO_4$ solution. The vertical dashed lines on Figure 3.28(b) are 2-theta positions of pure Pd [92].

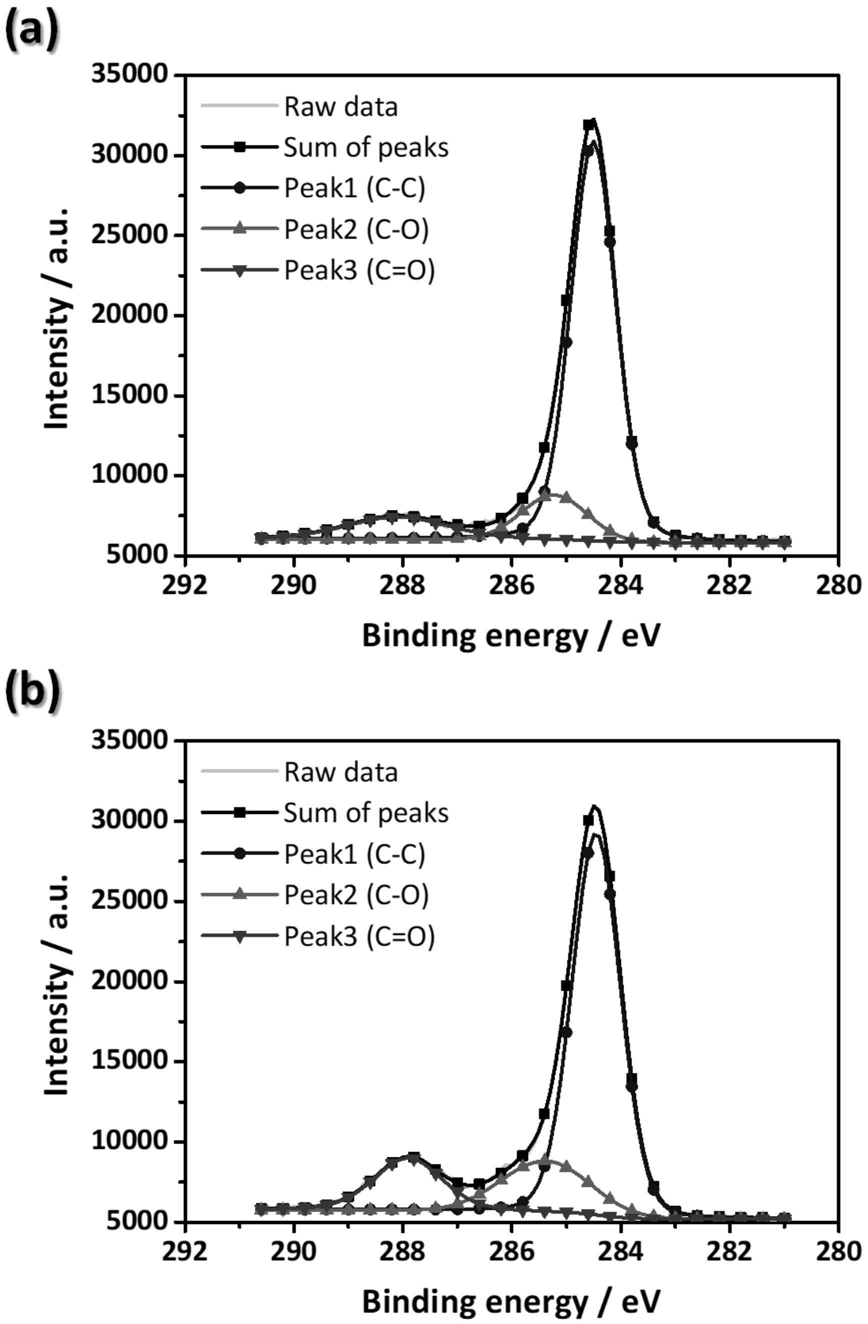

Figure 3.29. XPS C 1s spectra of Pd-Cu catalysts prepared with (a) 0 mM and (b) 1 mM of citric acid in $PdSO_4$ solution.

3.2.2. Catalytic performance toward electrochemical N_2O reduction

The effect of composition of Pd-Cu catalysts on their catalytic activity toward electrochemical N_2O reduction was examined. LSV analysis for the prepared Pd-Cu catalysts was performed to evaluate their electrochemical catalytic activities for the N_2O reduction reaction. Figure 3.30(a) represents LSV curves obtained using the $Pd_{49}Cu_{51}$, $Pd_{61}Cu_{39}$, $Pd_{66}Cu_{34}$, $Pd_{74}Cu_{26}$, and $Pd_{84}Cu_{16}$ catalysts. Tafel plots were obtained in the low overpotential region of the LSV curves to calculate Tafel slopes for N_2O reduction reaction as shown in Figure 3.30(b). Tafel slope of Pd-Cu catalysts decreased as increasing surface atomic concentration of Pd in Pd-Cu catalysts from 49 to 66%, indicating the enhanced catalytic activity for N_2O reduction. However, with further increasing Pd content in the catalysts over 66%, the Tafel slope was gradually increased. Among the investigated Pd-Cu catalysts, the $Pd_{66}Cu_{34}$ catalyst exhibited the highest catalytic activity toward electrochemical N_2O reduction reaction with the lowest Tafel slope of 0.096 V dec^{-1}. To elucidate the effect of salts such as K_2SO_4 and KOH, which were added in an electrolyte solution for efficient electrochemical analysis, on the calculation of Tafel slopes, LSV analysis was performed with or without N_2O purging in the electrolyte solution (Figure 3.31). LSV curves obtained in the N_2-purged solution showed that only the current for hydrogen evolution reaction was observed at the potential below -0.65 V and there was no electrochemical reaction occurring in the potential region more positive than -0.65 V [93]. In contrast, in the N_2O-saturated solution, N_2O reduction reaction also occurred from -0.25 V. From these results, it was found that, in the potential region more positive than -0.65 V where Tafel plots were obtained in this study, only the N_2O reduction reaction occurred. To evaluate the N_2O reduction activity of $Pd_{66}Cu_{34}$, Tafel slopes of $Pd_{66}Cu_{34}$ and pure Pd were compared as represented in Figure 3.32. $Pd_{66}Cu_{34}$ catalyst (0.096 V dec^{-1}) exhibited a lower Tafel slope for N_2O reduction than pure Pd (0.129 V dec^{-1}). Through the citric acid-assisted galvanic displacement, a Pd-Cu catalyst with higher N_2O reduction activity as compared to pure Pd was synthesized.

To gain insight into atomic-level energetic factors determining N_2O reduction activity of Pd-Cu catalyst, DFT calculations have been performed. The calculation was performed assuming that Pd atoms on Pd (111) monolayer (ML) were substituted with Cu atoms with the surface coverages of 0, 1/16, 4/16, 12/16, 15/16, and 1 ML. As shown in Figure 3.33, *d*-band center position of metal surfaces, which would be closely related to the degree of interaction between catalyst surface and reaction intermediates was explored [94-96]. Since Cu has a lower *d*-band center of -2.29 eV than Pd (-1.66 eV), adding Cu atoms into Pd catalyst resulted in the down-shift of *d*-band center, indicating the broaden *d*-band of catalyst (Figure 3.33). N_2O reduction activity, which can be represented by the reciprocal of Tafel slope, was plotted with *d*-band center position of Pd-Cu catalysts (Figure 3.34(a)). The *d*-band center values of Pd-Cu catalysts with different Pd/Cu composition were obtained by linear approximation from Figure 3.33. As shown in Figure 3.34(a), the N_2O reduction activity versus *d*-band center position of

Pd-Cu catalysts exhibited a volcano-shaped dependence. The origin of the volcano plot was illustrated in Figure 3.34(b). With increasing Cu content in Pd-Cu catalysts, the chemisorption energy to a reactant could be weaken due to the broaden *d*-band of catalysts, thus the N_2O reduction reaction could be retarded by dissociation of N_2O. Conversely, for the Pd-Cu catalysts with high Pd/Cu ratio, the reaction rate is limited by removal of products from N_2O reduction reaction due to too strong chemisorption energy. In conclusion, the highest N_2O reduction activity at the optimum composition of $Pd_{66}Cu_{34}$ resulted from moderate bonding energy between a catalyst and reaction intermediates which was induced by adding an appropriate amount of Cu in Pd catalyst.

In an economical point of view, Pd loading amount is a critical issue due to the high price of noble metals. Therefore, the lowering loading amount of Pd on catalysts significantly could reduce the cost for catalyst preparation. By using galvanic displacement reaction, Pd loading amount can be dramatically reduced by depositing thin film with a small amount of Pd on substrate surface. The mass activity, which refers to current per unit mass of noble metal loaded on each catalyst, of as-prepared $Pd_{66}Cu_{34}$ catalyst was compared with that of commercial Pd/C catalyst as shown in Figure 3.35. The Pd loading amount of each catalyst, measured by ICP-AES, was summarized in Table 3.4. LSV curves were obtained with $Pd_{66}Cu_{34}$ and Pd/C catalysts (Figure 3.35(a)) and N_2O reduction current was normalized to Pd loading amount of each catalyst (Figure 3.35(b)). At -0.65 V, the $Pd_{66}Cu_{34}$ catalyst produced the remarkably higher mass activity of -10.109 mA μg^{-1} in comparison with Pd/C (-0.060 mA μg^{-1}). The 168-folded higher efficiency with small amount of Pd loading was due to the enhanced catalytic activity by alloying effect and the formation of thin catalyst film through galvanic displacement reaction. Therefore, the catalyst with significantly high Pd-mass activity toward N_2O reduction reaction was successfully fabricated by coating the substrate with thin Pd-Cu catalyst layer which had the optimum Pd/Cu ratio for improved catalytic performance using the facile galvanic displacement method.

Table 3.4. Pd loading amount measured by ICP-AES of commercial Pd/C and the prepared $Pd_{66}Cu_{34}$ catalysts

	Pd/C	$Pd_{66}Cu_{34}$
Pd loading	71.79 ug cm^{-2}	0.44 ug cm^{-2}

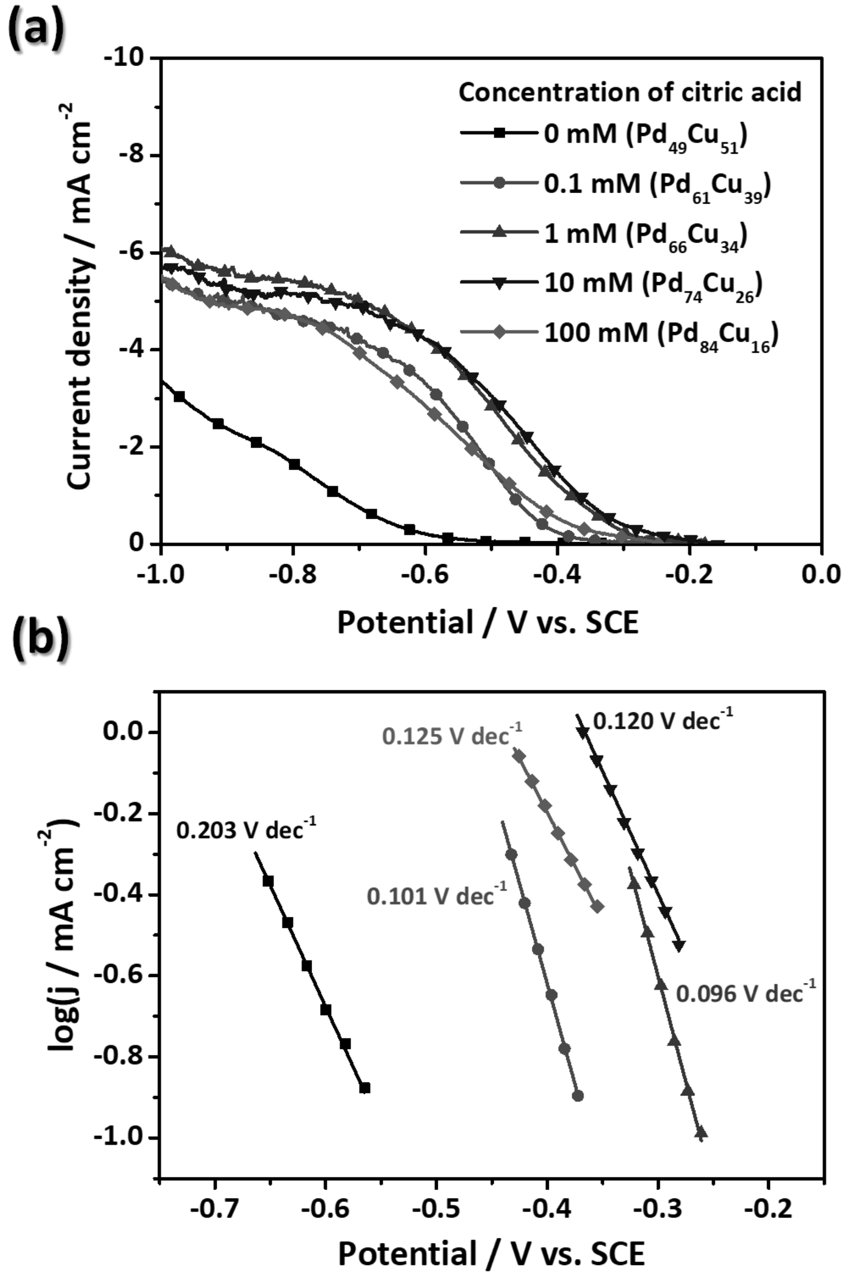

Figure 3.30. (a) LSV curves in N_2O-saturated solution and (b) Tafel plots for electrochemical N_2O reduction reaction of $Pd_{84}Cu_{16}$, $Pd_{74}Cu_{26}$, $Pd_{66}Cu_{34}$, $Pd_{61}Cu_{39}$, and $Pd_{49}Cu_{51}$ catalysts prepared by galvanic displacement in $PdSO_4$ solution with 0, 0.1, 1, 10, and 100 mM of citric acid.

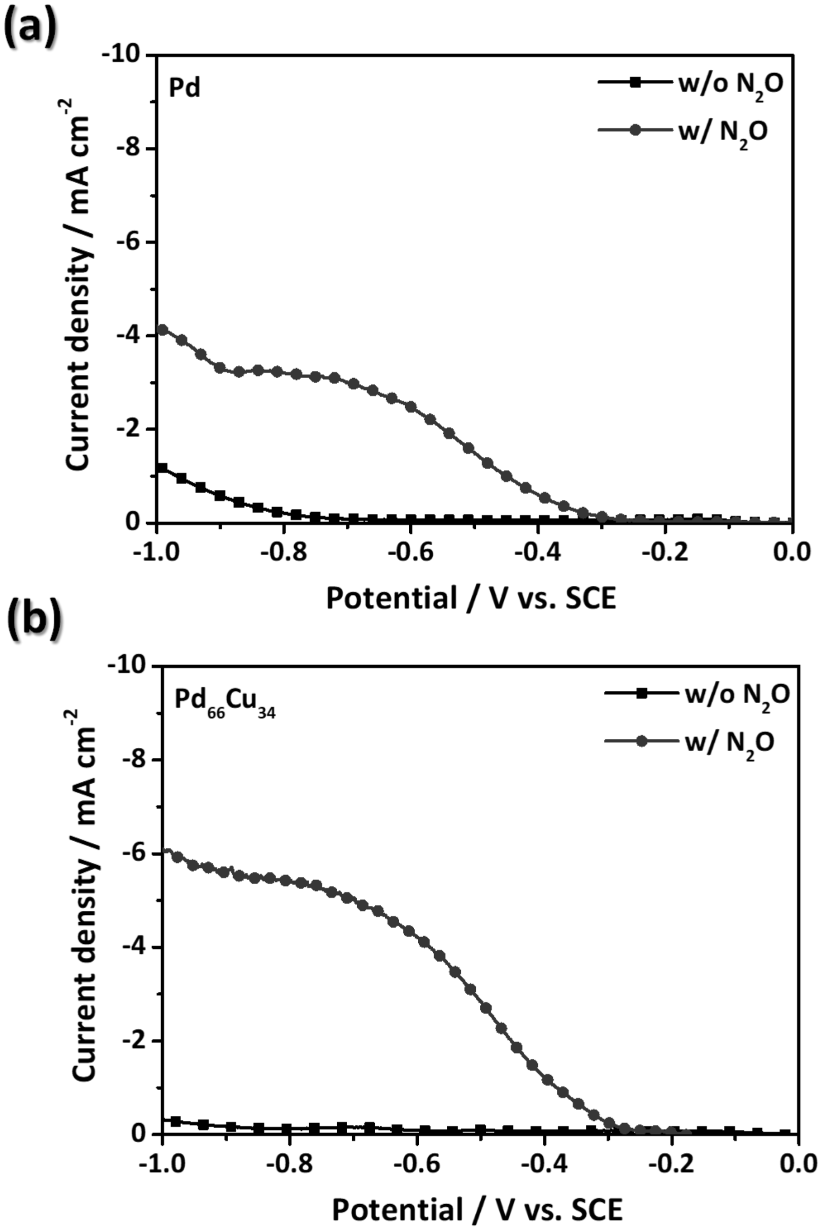

Figure 3.31. LSV curves of (a) Pd and (b) $Pd_{66}Cu_{34}$ catalysts obtained in the solution with N_2 (w/o N_2O) or N_2O (w/ N_2O) purging.

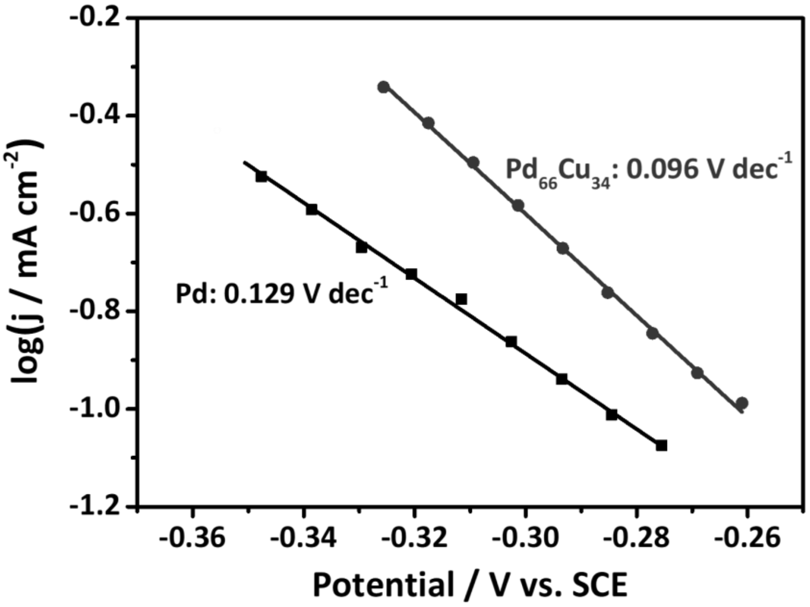

Figure 3.32. Tafel plots for electrochemical N_2O reduction reaction of Pd and $Pd_{66}Cu_{34}$ catalysts.

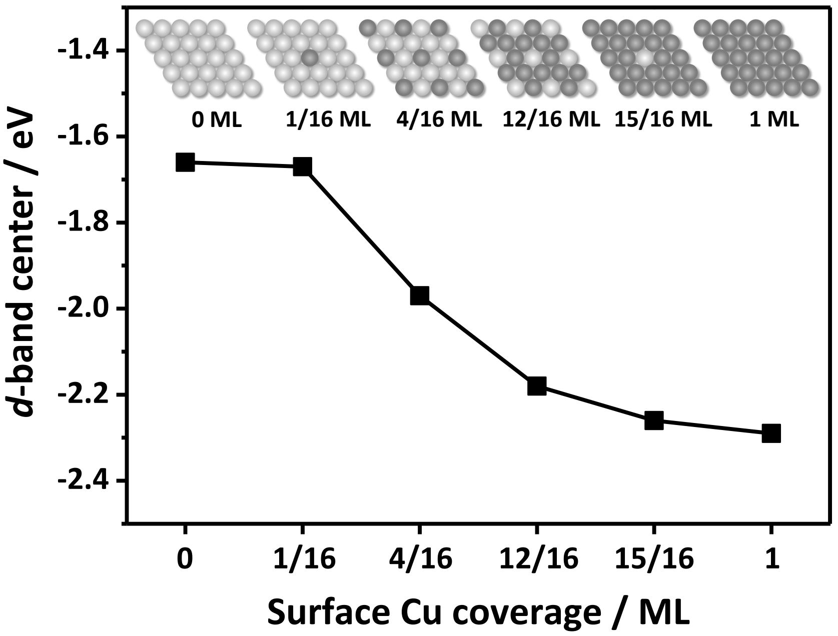

Figure 3.33. *d*-band center positions of Pd-Cu catalysts as a function of surface Cu coverage.

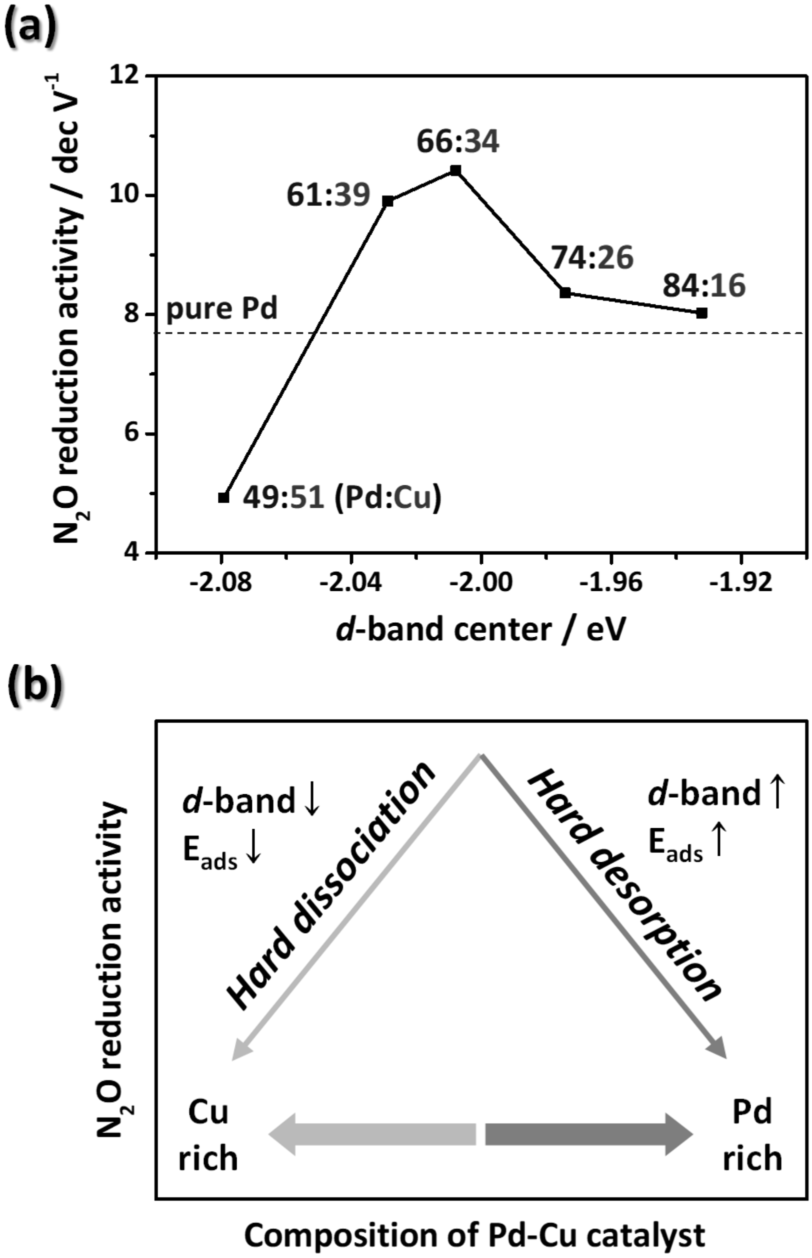

Figure 3.34. (a) Volcano plot relationship of N_2O reduction activity with *d*-band center position of Pd-Cu catalysts with different Pd/Cu composition and (b) schematic illustration of N_2O reduction activity influenced by electronic effect of Pd-Cu catalysts.

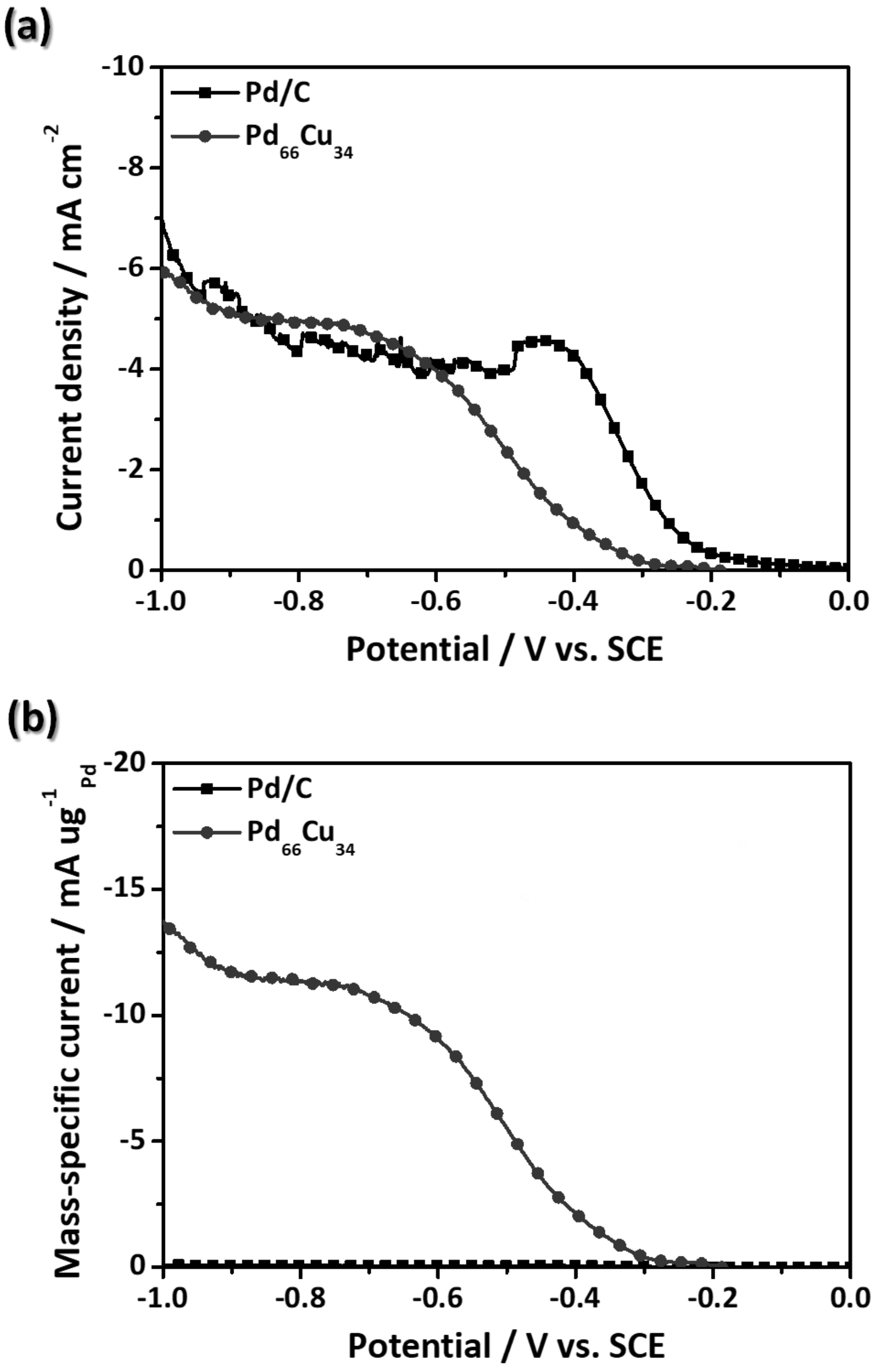

Figure 3.35. (a) LSV curves for electrochemical N_2O reduction reaction and (b) Pd-mass-normalized current of Pd/C and $Pd_{66}Cu_{34}$ catalysts.

CHAPTER IV

Conclusion

In this study, Pd-Cu catalysts were prepared via galvanic displacement deposition. The structure of Pd-Cu catalysts was adjusted to a planar or whisker shape by controlling the reaction kinetics. The type of counter ion of Pd precursor such as Cl^- and SO_4^{2-} ions can alter the rate of Cu oxidation and the mass transfer rate of metal ions in galvanic displacement reaction. The addition of Cl^- ion in galvanic displacement bath accelerates Cu oxidation reaction, which subsequently enhances Pd reduction rate, thus forming steep concentration gradient of Pd^{2+} ion near the Cu substrate. It was found that the steep concentration gradient of Pd^{2+} ion induced by Cl^- ion is essential for fabricating whisker-type metal deposits by galvanic displacement. This synthetic method for whisker catalyst can be applied to the fabrication of catalysts comprising various noble metals—including Pd-Cu, Pt-Cu, and Au-Cu —with a dramatic increase in the surface areas. It was also confirmed that the whisker-type Pd-Cu catalyst had superior electrocatalytic performance toward ethanol oxidation reaction than planar catalyst due to its large number of electrochemically active sites.

The prepared Pd-Cu whisker catalyst was also applied for N_2O reduction. To improve mass transfer of N_2O in the electrolyte solution, CTF mixer was used to induce Taylor vortices. The application of the CTF mixer resulted in the rapid dissolution and enhanced

N_2O solubility due to the intensive mixing by Taylor vortices. The saturation time was reduced by 15-fold and the saturated N_2O concentration was increased by 26.9% compared with usual mixing method using an overhead stirrer. The effectiveness of the enhanced N_2O dissolution on electrochemical N_2O reduction was tested using the CTF mixer/electrolysis reactor hybrid system. Pd-Cu whisker catalyst obtained by galvanic displacement deposition on Cu foil was attached to an outer cylinder of CTF mixer as a N_2O-reducing catalyst. Electrochemical N_2O conversions strongly depended on the existence of Taylor vortices in an electrolyte solution. When applying N_2O reduction potential of 3.5 V to the system, N_2O conversion of 99.99% was achieved by generating Taylor vortices in the solution. In contrast, N_2O conversion was about 5.39% in the absence of Taylor vortices. Therefore, it is noteworthy that N_2O electrolysis can proceed efficiently with the CTF mixer/electrolysis reactor hybrid system which can keep the N_2O concentration high and rapidly dissolve N_2O during the electrolysis.

The galvanic displacement can be also applied to synthesize catalysts with various alloy composition. Citric acid was added in galvanic displacement bath as a composition controller of Pd-Cu alloy. Citric acid was strongly adsorbed on the deposit and remained not dissociated. Thus, it was incorporated into the deposit during the galvanic displacement deposition. The incorporated citric acid restrained the Cu diffusion from Cu substrate to the deposit, resulting in the decrease in Cu content in Pd-Cu alloy. In this regard, Pd/Cu ratio in Pd-Cu catalysts was increased as increasing citric acid concentration. The catalytic activity of Pd_xCu_{100-x} catalysts (x=0, 61, 66, 74, 84, and 100) for electrochemical N_2O reduction was assessed and $Pd_{66}Cu_{34}$ catalyst exhibited the highest catalytic activity among the prepared catalysts. DFT calculations revealed that the optimum composition of $Pd_{66}Cu_{34}$ with the highest catalytic activity could result from the moderate bonding energy to reaction intermediates of N_2O reduction.

References

[1] W.B. Tolman, Binding and Activation of N_2O at Transition-Metal Centers: Recent Mechanistic Insights, Angewandte Chemie International Edition, 49 (2010) 1018-1024.

[2] A. Kudo, A. Mine, Electrocatalysis for N_2O reduction on metal electrodes, Journal of Electroanalytical Chemistry, 408 (1996) 267-269.

[3] B. Wang, X.-y. Li, Electrocatalytic properties of nitrous oxide and its voltammetric detection at palladium electrodeposited on a glassy carbon electrode, Analytical Chemistry, 70 (1998) 2181-2187.

[4] A. Kudo, A. Mine, High efficiency electrochemical reduction of N_2O on ZnO and In_2O_3 oxide semiconductor electrodes, Journal of Electroanalytical Chemistry, 426 (1997) 1-3.

[5] E. Kanazawa, G. Sakai, K. Shimanoe, Y. Kanmura, Y. Teraoka, N. Miura, N. Yamazoe, Metal oxide semiconductor N_2O sensor for medical use, Sensors and Actuators B: Chemical, 77 (2001) 72-77.

[6] R. Gómez, M.J. Weaver, Reduction of nitrous oxide on iridium single-crystal electrodes, Langmuir, 18 (2002) 4426-4432.

[7] Y. Yoshida, S. Ogata, S. Nakamatsu, H. Inoue, C. Iwakura, Catalytic reduction of nitrous oxide with atomic hydrogen permeating through palladized Pd sheet electrodes, Electrochimica acta, 44 (1999) 3585-3587.

[8] A. Dandekar, M. Vannice, Decomposition and reduction of N_2O over copper catalysts, Applied Catalysis B: Environmental, 22 (1999) 179-200.

[9] N. Konishi, K. Hara, A. Kudo, T. Sakata, Electrochemical reduction of N_2O on gas-diffusion electrodes, Bulletin of the chemical society of japan, 69 (1996) 2159-2162.

[10] M. Galle, D. Agar, O. Watzenberger, Thermal N_2O decomposition in regenerative heat exchanger reactors, Chemical Engineering Science, 56 (2001) 1587-1595.

[11] N. Velić, M. Samardžić, M. Sak-Bosnar, B. Šantek, Voltammetric determination of dissolved nitrous oxide, Int. J. Electrochem. Sci, 6 (2011) 1206-1215.

[12] Z. Liu, F. He, L. Ma, S. Peng, Recent advances in catalytic decomposition of N_2O on noble metal and metal oxide catalysts, Catalysis Surveys from Asia, 20 (2016) 121-132.

[13] K. Kanazawa, H. Yamamura, M. Nakayama, K. Ogura, Electrochemical reduction of nitrous oxide by the protons transported through polyelectrolyte-coated porous glass, Journal of Electroanalytical Chemistry, 521 (2002) 127-131.

[14] K.E. Johnson, D.T. Sawyer, The electrochemical reduction of nitrous oxide in alkaline solution, Journal of Electroanalytical Chemistry and Interfacial Electrochemistry, 49 (1974) 95-103.

[15] A. Aziznia, A. Bonakdarpour, E.L. Gyenge, C.W. Oloman, Electroreduction of nitrous oxide on platinum and palladium: Toward selective catalysts for methanol–nitrous oxide mixed-reactant fuel cells, Electrochimica Acta, 56 (2011) 5238-5244.

[16] A. Kudo, A. Mine, Electrocatalytic reduction of nitrous oxide on metal and oxide

electrodes in aqueous solution, Applied surface science, 121 (1997) 538-542.

[17] S. Isa, J. Saleh, Oxidation of metal films by nitrous oxide, The Journal of Physical Chemistry, 76 (1972) 2530-2535.

[18] K. Jiang, H.-X. Zhang, S. Zou, W.-B. Cai, Electrocatalysis of formic acid on palladium and platinum surfaces: from fundamental mechanisms to fuel cell applications, Physical Chemistry Chemical Physics, 16 (2014) 20360-20376.

[19] D. Chen, P. Sun, H. Liu, J. Yang, Bimetallic Cu–Pd alloy multipods and their highly electrocatalytic performance for formic acid oxidation and oxygen reduction, Journal of Materials Chemistry A, 5 (2017) 4421-4429.

[20] J.R. Kitchin, J.K. Nørskov, M.A. Barteau, J. Chen, Role of strain and ligand effects in the modification of the electronic and chemical properties of bimetallic surfaces, Physical review letters, 93 (2004) 156801.

[21] M. Mavrikakis, B. Hammer, J.K. Nørskov, Effect of strain on the reactivity of metal surfaces, Physical Review Letters, 81 (1998) 2819.

[22] J. Rodriguez, Physical and chemical properties of bimetallic surfaces, Surface science reports, 24 (1996) 223-287.

[23] V. Pallassana, M. Neurock, L.B. Hansen, B. Hammer, J.K. Nørskov, Theoretical analysis of hydrogen chemisorption on Pd(111), Re(0001) and Pd_{ML}/Re(0001), Re_{ML}/Pd(111) pseudomorphic overlayers, Physical Review B, 60 (1999) 6146.

[24] J. Rodriguez, Electronic and chemical properties of Pt, Pd and Ni in bimetallic surfaces, Surface science, 345 (1996) 347-362.

[25] H. Chen, J. Yue, Y. Li, C. Yi, B. Yang, S. Qi, Catalytic activity prediction of different metal surfaces for N_2O catalytic decomposition by density functional theory, Computational and Theoretical Chemistry, 1057 (2015) 1-6.

[26] S. Cherevko, N. Kulyk, C.-H. Chung, Nanoporous palladium with sub-10 nm dendrites by electrodeposition for ethanol and ethylene glycol oxidation, Nanoscale, 4 (2012) 103-105.

[27] C. Xu, H. Wang, P.K. Shen, S.P. Jiang, Highly ordered Pd nanowire arrays as effective electrocatalysts for ethanol oxidation in direct alcohol fuel cells, Advanced Materials, 19 (2007) 4256-4259.

[28] S. Shen, T. Zhao, J. Xu, Y. Li, Synthesis of PdNi catalysts for the oxidation of ethanol in alkaline direct ethanol fuel cells, Journal of Power Sources, 195 (2010) 1001-1006.

[29] Z. Liang, T. Zhao, J. Xu, L. Zhu, Mechanism study of the ethanol oxidation reaction on palladium in alkaline media, Electrochimica Acta, 54 (2009) 2203-2208.

[30] S. Hu, L. Scudiero, S. Ha, Electronic effect on oxidation of formic acid on supported Pd–Cu bimetallic surface, Electrochimica Acta, 83 (2012) 354-358.

[31] J. Noborikawa, J. Lau, J. Ta, S. Hu, L. Scudiero, S. Derakhshan, S. Ha, J.L. Haan, Palladium-copper electrocatalyst for promotion of oxidation of formate and ethanol in alkaline media, Electrochimica Acta, 137 (2014) 654-660.

[32] C. Hu, X. Zhai, Y. Zhao, K. Bian, J. Zhang, L. Qu, H. Zhang, H. Luo, Small-sized PdCu nanocapsules on 3D graphene for high-performance ethanol oxidation, Nanoscale,

6 (2014) 2768-2775.

[33] J. Liu, Z. Huang, K. Cai, H. Zhang, Z. Lu, T. Li, Y. Zuo, H. Han, Clean synthesis of an economical 3d nanochain network of pdcu alloy with enhanced electrocatalytic performance towards ethanol oxidation, Chemistry–A European Journal, 21 (2015) 17779-17785.

[34] L. Au, X. Lu, Y. Xia, A comparative study of galvanic replacement reactions involving Ag nanocubes and $AuCl_2^-$ or $AuCl_4^-$, Advanced materials, 20 (2008) 2517-2522.

[35] D.-Y. Park, H. Jung, Y. Rheem, C. Hangarter, Y.-I. Lee, J. Ko, Y.-H. Choa, N. Myung, Morphology controlled 1D Pt nanostructures synthesized by galvanic displacement of Cu nanowires in chloroplatinic acid, Electrochimica Acta, 55 (2010) 4212-4216.

[36] W. Wang, M. Dahl, Y. Yin, Hollow nanocrystals through the nanoscale Kirkendall effect, Chemistry of Materials, 25 (2012) 1179-1189.

[37] A.-A. El Mel, R. Nakamura, C. Bittencourt, The Kirkendall effect and nanoscience: hollow nanospheres and nanotubes, Beilstein journal of nanotechnology, 6 (2015) 1348-1361.

[38] O. Ghodbane, L. Roué, D. Bélanger, Study of the electroless deposition of Pd on Cu-modified graphite electrodes by metal exchange reaction, Chemistry of Materials, 20 (2008) 3495-3504.

[39] M. Mohl, D. Dobo, A. Kukovecz, Z. Konya, K. Kordas, J. Wei, R. Vajtai, P.M.

Ajayan, Formation of CuPd and CuPt bimetallic nanotubes by galvanic replacement reaction, The Journal of Physical Chemistry C, 115 (2011) 9403-9409.

[40] L. Magagnin, R. Maboudian, C. Carraro, Gold deposition by galvanic displacement on semiconductor surfaces: effect of substrate on adhesion, The Journal of Physical Chemistry B, 106 (2002) 401-407.

[41] L.A. Porter, H.C. Choi, A.E. Ribbe, J.M. Buriak, Controlled electroless deposition of noble metal nanoparticle films on germanium surfaces, Nano letters, 2 (2002) 1067-1071.

[42] M. Shao, T. Huang, P. Liu, J. Zhang, K. Sasaki, M. Vukmirovic, R. Adzic, Palladium monolayer and palladium alloy electrocatalysts for oxygen reduction, Langmuir, 22 (2006) 10409-10415.

[43] F.-R. Fan, D.-Y. Liu, Y.-F. Wu, S. Duan, Z.-X. Xie, Z.-Y. Jiang, Z.-Q. Tian, Epitaxial growth of heterogeneous metal nanocrystals: from gold nano-octahedra to palladium and silver nanocubes, Journal of the American Chemical Society, 130 (2008) 6949-6951.

[44] Y. Sun, Y. Wang, Monitoring of galvanic replacement reaction between silver nanowires and $HAuCl_4$ by in situ transmission X-ray microscopy, Nano letters, 11 (2011) 4386-4392.

[45] R.G. Milazzo, S.M. Privitera, D. D'Angelo, S. Scalese, S. Di Franco, F. Maita, S. Lombardo, Spontaneous galvanic displacement of Pt nanostructures on nickel foam: Synthesis, characterization and use for hydrogen evolution reaction, International Journal of Hydrogen Energy, 43 (2018) 7903-7910.

[46] X. Wang, N. Kariuki, J.T. Vaughey, J. Goodpaster, R. Kumar, D.J. Myers, Bimetallic Pd–Cu oxygen reduction electrocatalysts, Journal of The Electrochemical Society, 155 (2008) B602-B609.

[47] B.K. Kim, S.-K. Kim, S.K. Cho, J.J. Kim, Enhanced catalytic activity of electrodeposited Ni-Cu-P toward oxygen evolution reaction, Applied Catalysis B: Environmental, 237 (2018) 409-415.

[48] J. Suntivich, Z. Xu, C.E. Carlton, J. Kim, B. Han, S.W. Lee, N.p. Bonnet, N. Marzari, L.F. Allard, H.A. Gasteiger, Surface composition tuning of Au–Pt bimetallic nanoparticles for enhanced carbon monoxide and methanol electro-oxidation, Journal of the American Chemical Society, 135 (2013) 7985-7991.

[49] F. Fouda-Onana, S. Bah, O. Savadogo, Palladium–copper alloys as catalysts for the oxygen reduction reaction in an acidic media I: Correlation between the ORR kinetic parameters and intrinsic physical properties of the alloys, Journal of Electroanalytical Chemistry, 636 (2009) 1-9.

[50] S. Weisenberger, d.A. Schumpe, Estimation of gas solubilities in salt solutions at temperatures from 273 K to 363 K, AIChE Journal, 42 (1996) 298-300.

[51] M.C. dos Ramos, F.J. Blas, A. Galindo, Phase equilibria, excess properties, and Henry's constants of the water + carbon dioxide binary mixture, The Journal of Physical Chemistry C, 111 (2007) 15924-15934.

[52] R.F. Weiss, Carbon dioxide in water and seawater: the solubility of a non-ideal gas, Marine chemistry, 2 (1974) 203-215.

[53] R. Hubacz, S. Wroński, Horizontal Couette–Taylor flow in a two-phase gas–liquid system: flow patterns, Experimental thermal and fluid science, 28 (2004) 457-466.

[54] R.J. Campero, R.D. Vigil, Axial dispersion during low Reynolds number Taylor-Couette flow: intra-vortex mixing effects, Chemical engineering science, 52 (1997) 3303-3310.

[55] E. Dumont, F. Fayolle, V. Sobolík, J. Legrand, Wall shear rate in the Taylor–Couette–Poiseuille flow at low axial Reynolds number, International Journal of Heat and Mass Transfer, 45 (2002) 679-689.

[56] N. Ohmura, K. Kataoka, Y. Shibata, T. Makino, Effective mass diffusion over cell boundaries in a Taylor-Couette flow system, Chemical Engineering Science, 52 (1997) 1757-1765.

[57] Y. Murai, Frictional drag reduction by bubble injection, Experiments in Fluids, 55 (2014) 1773.

[58] S. Wroński, R. Hubacz, T. Ryszczuk, Interfacial area in a reactor with helicoidal flow for the two-phase gas–liquid system, Chemical Engineering Journal, 105 (2005) 71-79.

[59] S. Wroński, E. Dłuska, R. Hubacz, E. Molga, Mass transfer in gas–liquid Couette–Taylor flow in membrane reactor, Chemical engineering science, 54 (1999) 2963-2967.

[60] M. Kim, K.J. Park, K.U. Lee, M.J. Kim, W.-S. Kim, O.J. Kwon, J.J. Kim, Preparation of black pigment with the Couette–Taylor vortex for electrophoretic displays, Chemical Engineering Science, 119 (2014) 245-250.

[61] A.J. Bard, L.R. Faulkner, Fundamentals and applications, Electrochemical Methods, 2 (2001) 482.

[62] G. Kresse, J. Furthmüller, Efficient iterative schemes for ab initio total-energy calculations using a plane-wave basis set, Physical review B, 54 (1996) 11169.

[63] G. Kresse, J. Hafner, Ab initio molecular-dynamics simulation of the liquid-metal–amorphous-semiconductor transition in germanium, Physical Review B, 49 (1994) 14251.

[64] H.J. Monkhorst, J.D. Pack, Special points for Brillouin-zone integrations, Physical review B, 13 (1976) 5188.

[65] S. Grimme, S. Ehrlich, L. Goerigk, Effect of the damping function in dispersion corrected density functional theory, Journal of computational chemistry, 32 (2011) 1456-1465.

[66] H. Chen, Q. Lu, C. Yi, B. Yang, S. Qi, Bimetallic Rh–Fe catalysts for N_2O decomposition: effects of surface structures on catalytic activity, Physical Chemistry Chemical Physics, 20 (2018) 5103-5111.

[67] B. Kim, T. Ritzdorf, Electrodeposition of near-eutectic SnAg solders for wafer-level packaging, Journal of the electrochemical Society, 150 (2003) C577-C584.

[68] K. Zhuo, M.-G. Jeong, C.-H. Chung, Dendritic nanoporous nickel oxides for a supercapacitor prepared by a galvanic displacement reaction with chlorine ions as an accelerator, RSC Advances, 3 (2013) 12611-12615.

[69] Y. Wang, B. Liu, S. Xiao, H. Li, L. Wang, D. Cai, D. Wang, Y. Liu, Q. Li, T. Wang,

High performance and negative temperature coefficient of low temperature hydrogen gas sensors using palladium decorated tungsten oxide, Journal of Materials Chemistry A, 3 (2015) 1317-1324.

[70] T. Gao, G. Meng, J. Zhang, Y. Wang, C. Liang, J. Fan, L. Zhang, Template synthesis of single-crystal Cu nanowire arrays by electrodeposition, Applied Physics A, 73 (2001) 251-254.

[71] S. Milić, M. Antonijević, Some aspects of copper corrosion in presence of benzotriazole and chloride ions, Corrosion Science, 51 (2009) 28-34.

[72] C. Bonfiglio, H. Albaya, O. Cobo, The kinetics of the anodic dissolution of copper in acid chloride solutions, Corrosion Science, 13 (1973) 717-724.

[73] M. Jayakumar, K. Venkatesan, T. Srinivasan, Electrochemical behavior of fission palladium in 1-butyl-3-methylimidazolium chloride, Electrochimica Acta, 52 (2007) 7121-7127.

[74] L. Espinosa-Alonso, K. De Jong, B. Weckhuysen, A UV-Vis micro-spectroscopic study to rationalize the influence of Cl^{-}(aq) on the formation of different Pd macro-distributions on γ-Al_2O_3 catalyst bodies, Physical Chemistry Chemical Physics, 12 (2010) 97-107.

[75] S. Kaja, S.P. Mukherjee, E.J. O'sullivan, M. Paunovic, Palladium sulfate solution for the selective seeding of the metal interconnections on polyimide dielectrics for electroless metal deposition, Google Patents, 1995.

[76] A. Correia, L. Mascaro, S. Machado, L. Avaca, Active surface area determination

of Pd-Si alloys by H-adsorption, Electrochimica acta, 42 (1997) 493-495.

[77] Z.-Y. Shih, C.-W. Wang, G. Xu, H.-T. Chang, Porous palladium copper nanoparticles for the electrocatalytic oxidation of methanol in direct methanol fuel cells, Journal of Materials Chemistry A, 1 (2013) 4773-4778.

[78] R. Kádár, C. Balan, Transient dynamics of the wavy regime in Taylor–Couette geometry, European Journal of Mechanics-B/Fluids, 31 (2012) 158-167.

[79] R. Weiss, B. Price, Nitrous oxide solubility in water and seawater, Marine chemistry, 8 (1980) 347-359.

[80] K. Andersen, T. Kjær, N.P. Revsbech, An oxygen insensitive microsensor for nitrous oxide, Sensors and Actuators B: Chemical, 81 (2001) 42-48.

[81] P.R. Childs, Rotating cylinders, annuli, and spheres, Rotating Flow, (2011) 177-247.

[82] M. Nemri, S. Charton, É. Climent, Mixing and axial dispersion in Taylor–Couette flows: the effect of the flow regime, Chemical Engineering Science, 139 (2016) 109-124.

[83] W.M. Jung, S.H. Kang, W.-S. Kim, C.K. Choi, Particle morphology of calcium carbonate precipitated by gas–liquid reaction in a Couette–Taylor reactor, Chemical engineering science, 55 (2000) 733-747.

[84] S. Poncet, R. Da Soghe, C. Bianchini, S. Viazzo, A. Aubert, Turbulent Couette–Taylor flows with endwall effects: a numerical benchmark, International Journal of Heat and Fluid Flow, 44 (2013) 229-238.

[85] E. Dłuska, S. Wroński, T. Ryszczuk, Interfacial area in gas–liquid Couette–Taylor flow reactor, Experimental thermal and fluid science, 28 (2004) 467-472.

[86] Y. Jin, D. Sun, J. Yu, C. Dong, D. Yang, Effects of complexing agent on the morphology and porosity of electroless nickel deposits, Transactions of the IMF, 77 (1999) 181-184.

[87] P. Muhammed Shafi, A. Chandra Bose, Impact of crystalline defects and size on X-ray line broadening: A phenomenological approach for tetragonal SnO_2 nanocrystals, AIP Advances, 5 (2015) 057137.

[88] H. Zhang, Z. Yang, Y. Ju, X. Chu, Y. Ding, X. Huang, K. Zhu, T. Tang, X. Su, Y. Hou, Galvanic Displacement Synthesis of Monodisperse Janus-and Satellite-Like Plasmonic–Magnetic Ag–Fe@ Fe_3O_4 Heterostructures with Reduced Cytotoxicity, Advanced Science, 5 (2018) 1800271.

[89] Z. Wang, X. Xiao, T. Zou, Y. Yang, X. Xing, R. Zhao, Z. Wang, Y. Wang, Citric acid capped CdS quantum dots for fluorescence detection of copper ions (II) in aqueous solution, Nanomaterials, 9 (2019) 32.

[90] S. Zhu, J. Yue, X. Qin, Z. Wei, Z. Liang, R.R. Adzic, S.R. Brankovic, Z. Du, M. Shao, The role of citric acid in perfecting platinum monolayer on palladium nanoparticles during the surface limited redox replacement reaction, Journal of The Electrochemical Society, 163 (2016) D3040-D3046.

[91] M.J. Kim, S. Choe, H.C. Kim, S.K. Cho, S.-K. Kim, J.J. Kim, Electrochemical behavior of citric acid and its influence on Cu electrodeposition for damascene metallization, Journal of The Electrochemical Society, 162 (2015) D354-D359.

[92] M.-L. Chen, C.-Y. Park, J.-G. Choi, W.-C. Oh, Synthesis and characterization of

metal (Pt, Pd and Fe)-graphene composites, Journal of the Korean Ceramic Society, 48 (2011) 147-151.

[93] M.C. Jeong, C.H. Pyun, I.H. Yeo, Voltammetric studies on the palladium oxides in alkaline media, Journal of The Electrochemical Society, 140 (1993) 1986-1989.

[94] Y. Mun, K. Kim, S. Kim, S. Lee, S. Lee, S. Kim, W. Choi, S.-k. Kim, J.W. Han, J. Lee, A novel strategy to develop non-noble metal catalyst for CO_2 electroreduction: Hybridization of metal-organic polymer, Applied Catalysis B: Environmental, 236 (2018) 154-161.

[95] J. Ko, H. Kwon, H. Kang, B.-K. Kim, J.W. Han, Universality in surface mixing rule of adsorption strength for small adsorbates on binary transition metal alloys, Physical Chemistry Chemical Physics, 17 (2015) 3123-3130.

[96] V. Stamenkovic, B.S. Mun, K.J. Mayrhofer, P.N. Ross, N.M. Markovic, J. Rossmeisl, J. Greeley, J.K. Nørskov, Changing the activity of electrocatalysts for oxygen reduction by tuning the surface electronic structure, Angewandte Chemie International Edition, 45 (2006) 2897-2901.

국문 초록

촉매의 전자구조와 전기화학적 활성 표면적은 전기화학 반응에 대한 촉매의 활성을 결정하는 중요한 요소이다. 갈바닉 치환 반응을 이용한 촉매 합성법을 통해 합금을 형성하거나 촉매의 구조를 변화시킴으로써 고활성 전기화학 촉매를 제조할 수 있다. 구리 기판을 팔라듐 양이온이 포함되어 있는 용액에 담그면 팔라듐과 구리의 표준 환원 전위 차이로 인하여 갈바닉 치환 반응이 자발적으로 일어나 팔라듐이 전착된다. 팔라듐-구리 갈바닉 치환 반응이 일어나는 동안, Kirkendall 효과에 의해 구리 원자가 구리 기판에서 팔라듐 전착물로 확산하며 이로 인해 팔라듐-구리 합금이 형성된다. 이때, 갈바닉 치환 반응의 속도를 조절하면 팔라듐-구리 합금 촉매의 구조를 평면 형태 또는 휘스커 형태로 변화시킬 수 있다. 갈바닉 치환 반응 용액에 염화 이온을 첨가하면 반응 속도가 빨라지고 이로 인해 구리 기판 표면에 존재하는 팔라듐 양이온의 농도 구배가 커진다. 따라서 팔라듐-구리 전착물이 수직방향으로 성장하여 휘스커 형태의 구조를 갖게 된다. 합성한 팔라듐-구리 휘스커 촉매의 전기화학적 에탄올 산화 반응에 대한 활성을 조사한 결과, 휘스커 구조에 의한 넓은 반응 면적과 팔라듐과 구리의 상호작용에 의한 촉매의 전자구조 변화로 인해 평면 형태의 팔라듐 촉매보다 약 21배 더 높은 촉매 활성을 나타냈다.

합성한 휘스커 형태의 팔라듐-구리 촉매를 아산화질소의 전기화학적 환원 반응에도 적용하여 보았다. 구조적 단차가 큰 촉매에서 촉매 내부로의

N_2O 접근성을 향상시키고 더불어 N_2O의 용해를 촉진하기 위하여 쿠에트-테일러 흐름 혼합기와 전기화학 반응기가 융합된 시스템을 도입하였다. 쿠에트-테일러 흐름 혼합기의 내부 실린더 회전 속도를 증가시켜 테일러 수가 임계 값에 도달하게 되면, 반응기 내 용액에 테일러 와류가 형성되어 아산화질소의 용해가 촉진되고 용해도 또한 증가한다. 아산화질소의 용해 특성 향상이 아산화질소의 환원 반응에 미치는 영향을 조사하기 위해, 팔라듐-구리 휘스커 촉매를 아산화질소의 환원 반응 시 음극으로 이용되는 쿠에트-테일러 흐름 혼합기의 외부실린더에 부착하여 전압을 인가했다. 쿠에트-테일러 흐름 혼합기에 전압을 가하여 아산화질소 환원을 진행할 때, 용액 내 테일러 와류를 형성할 경우 99.99% 이상의 아산화질소 전환율을 얻을 수 있었다. 따라서, 본 연구에서는 갈바닉 치환 반응을 이용하여 촉매의 활성 표면적 및 전자구조를 조절하여 촉매 활성을 높이고, 쿠에트-테일러 흐름 혼합기가 융합된 전기화학 시스템을 도입하여 반응물의 용해 특성을 향상시킴으로써 전기화학 반응의 효율을 극대화 하였다.

팔라듐-구리 촉매의 전자구조는 갈바닉 치환 반응 용액에 구연산을 첨가하여 조절할 수 있다. 갈바닉 치환 반응 용액에 첨가하는 구연산 농도를 조절하면 팔라듐-구리 촉매 내 팔라듐과 구리의 원자 비율이 달라지며 이를 통해 촉매의 전자구조를 변화시킬 수 있다. 구연산은 갈바닉 치환 반응이 일어나는 동안 전착물 내 혼입되어 구리 원자가 기판으로부터 확산되는 것을 억제하기 때문에 전착된 팔라듐-구리 촉매 내 구리 원자의 비율을 감소시킨다. 팔라듐-구리 촉매의 아산화질소 환원 반응에 대한

활성은 촉매 내 팔라듐과 구리의 원자 비율에 크게 의존하는 특성을 보였다. 다양한 조성을 갖는 팔라듐-구리 촉매의 활성을 조사한 결과 팔라듐과 구리의 원자 비율이 66:34인 촉매가 아산화질소 환원 반응에 가장 우수한 활성을 나타내었으며, 상용 탄소 담지 팔라듐 촉매와 비교하여 월등히 높은 팔라듐 질량당 활성을 보였다. 밀도범함수이론 계산 결과 팔라듐과 구리의 원자 비율이 66:34인 촉매는 팔라듐과 구리의 원자간 전하 전달에 의해 촉매와 반응 중간체의 흡착에너지가 최적화 되어 아산화질소의 환원에 우수한 촉매 활성을 보이는 것으로 밝혀졌다.

주요어: 팔라듐-구리 촉매, 갈바닉 치환 반응, 휘스커 촉매, 에탄올의 전기화학적 산화, 아산화질소의 전기화학적 환원, 쿠에트-테일러 흐름 혼합기

학 번: 2014-21528